A CRYOGENIC TEST FACILITY

IAN VEENENDAAL
Bachelor of Science, University of Lethbridge, 2013

A Thesis
Submitted to the School of Graduate Studies
of the University of Lethbridge
in Partial Fulfillment of the
Requirements for the Degree

MASTER OF SCIENCE

Department of Physics and Astronomy
University of Lethbridge
LETHBRIDGE, ALBERTA, CANADA

A CRYOGENIC TEST FACILITY

IAN VEENENDAAL

Date of Defense: January 14, 2016

Dr. David Naylor Supervisor	Professor	Ph.D.
Dr. Locke Spencer Committee Member	Assistant Professor	Ph.D.
Dr. Adriana Predoi-Cross Committee Member	Professor	Ph.D.
Dr. René Boeré Chair, Thesis Examination Committee	Professor	Ph.D.

Dedication

This thesis is dedicated to my beautiful, caring, and supportive wife, Alexis.

Abstract

The next generation, space-borne instruments for far infrared spectroscopy will utilize large diameter, cryogenically cooled telescopes in order to achieve unprecedented sensitivities. Low background, ground-based cryogenic facilities are required for the cryogenic testing of materials, components and subsystems. The Test Facility Cryostat (TFC) at the University of Lethbridge is a large volume, closed cycle, 4 K cryogenic facility, developed for this purpose. This thesis discusses the design and performance of the facility and associated external instrumentation. An apparatus for measuring the thermal properties of materials is presented, and measurements of the thermal expansion and conductivity of carbon fibre reinforced polymers (CFRPs) at cryogenic temperatures are reported. Finally, I discuss the progress towards the design and fabrication of a demonstrator cryogenic, far infrared Fourier transform spectrometer.

Acknowledgments

First and foremost, I would like to thank my supervisor, Professor David Naylor, for taking me on as a summer research assistant in the second year of my undergraduate degree (even after I missed the application deadline), and continuing to support and encourage me through the completion of my undergraduate degree, and now, my Master's degree. I thank you for your continued support as I now pursue a PhD.

I would also like to thank the members of the Astronomical Instrumentation Group who played crucial roles in the completion of this thesis. To Brad Gom, thank you for imparting to me your vast knowledge of cryogenic systems, and for demonstrating a patient and meticulous attitude, which is crucial when working in a research lab with these delicate systems. To Gregory Tompkins, thank you for designing and building any and all electronics systems I needed for cryogenic measurements. Also, thank you Vince Weiler for your assistance in the building and testing of a circuit board, control software, and user interface for the differential interferometer. I would like to thank Abenezer Teklemariam, who assisted me with the heat load calculations for the Test Facility Cryostat (TFC), and Jacob Groeneveld for your help with the operation of the TFC. Also, a huge thank you to Dr. Sudhakar Gunuganti for always being able to provide a hand around the lab when it was needed, for providing critical feedback on many of my ideas, and for keeping the TFC operational while I was locked away, writing this thesis.

I would also like to thank Dr. Giorgio Savini and the EU FP7-FISICA programme for the funding and support I received from FISICA during my Master's degree. I would like to thank Professor David Walker and Martyn Jones of Glyndwr University for sending us carbon fibre reinforced polymer (CFRP) samples which were used in this thesis, and for encouraging further collaboration involving the fabrication and testing of CFRP samples at cryogenic temperatures. Also, I would like to thank Professor Peter Ade for his work on manufacturing a far infrared beamsplitter, which is a key component of the cryogenic spectrometer which I will be constructing for my PhD.

I would like to thank everyone else that shared an office with me throughout my Master's degree, including Dr. Matthijs van der Wiel, Dr. Gibion Makiwa, Tanner Heggie, and Sherif Abdelazim. You have all made my job more interesting, and have encouraged and pushed me to work hard on the task at hand.

I would like to thank my thesis committee, Professor Locke Spencer and Professor Adriana Predoi-Cross, for providing helpful feedback throughout every step of the way.

Lastly, thank you to my wife, Alexis, and my parents, Adrian and Ellis, for keeping me motivated during those long days and nights of writing.

Contents

List of Tables

List of Figures

Chapter 1

Far Infrared Astronomy

This chapter provides a brief introduction to the field of far infrared (FIR) astronomy. The science goals which make this waveband appealing are presented. In particular, the benefits of spectroscopy over conventional photometry are discussed. The challenges which are associated with observing in the FIR are also discussed. Strategies and new technologies which are used to overcome these challenges are presented. Finally, I present a brief overview of the use of cryogenics in FIR astronomy.

1.1 The Far-Infrared Wavelengths

The FIR wavelength band corresponds to the range of electromagnetic radiation from 30 to 300 μm [1]. This band lies between microwave wavelengths (1 to 1000 mm) and near and mid infrared wavebands (1 to 30 μm). Many disciplines may include submillimetre (SMM) wavelengths (300 to 1000 μm) in this band, and sometimes refer to it as the terahertz band ($\sim$300 GHz to 30 THz) depending on the dominant unit convention in the field. In astronomy, the FIR and SMM wavelengths are often observed simultaneously, with the same scientific objectives in mind, and will therefore be treated as synonymous in the following chapters. In infrared astronomy, there are two common unit conventions: the wavelength (measured in micrometres or microns) and the wavenumber (measured in inverse centimetres, cm^{-1}).

The FIR waveband, sandwiched between the widely used near-infrared and microwave bands, remains a relatively unexplored region. Far from being due to a lack of interest in the field, the lack of technology in FIR imaging is largely due to the low atmospheric propagation distance of FIR electromagnetic radiation (Figure 1.1), eliminating the drive to develop terrestrial technologies which use this band [2]. Additionally, many sources whose wavelength of peak emission lies in the far infrared are difficult to detect, owing to the low energy of individual photons emitted as compared to those at optical wavelengths. This is due to the inverse proportionality of wavelength to photon energy, E,

$$E = hc/\lambda \qquad \text{(eV)} \tag{1.1}$$

where h is Planck's constant, c is the speed of light in a vacuum, and λ is the photon wavelength. Far infrared photons have an energy of $<4 \times 10^{-2}$ eV. Astronomical observations in the far infrared provide a unique window through which to study a range of astronomical objects, from star forming regions to high redshifted galaxies (Section 1.2). As a result, astronomy has been the dominant driver for the advancement of technologies in this waveband.

While astronomy is the main driver for the development of FIR imaging technology, there are applications in other areas. Applications are limited in radar and telecommunications to short range systems. However, the spectroscopic identification of lightweight molecules makes FIR spectrometers useful for remote sensing. Additionally, tissue samples have peak absorption coefficients in the FIR waveband. Cancerous tissue has been found to have a higher absorption coefficent as compared with healthy tissue samples, owing in part to different concentrations of water within the sample [4]. Therefore, the detection of cancer through FIR imaging is seen as another potential market for terahertz technologies.

1.2 Observing in the FIR

It is estimated that over half of the radiant energy of the universe is emitted in the FIR [5, 6]. There are two key reasons for this: the absorption of high energy radiation by cold interstellar dust, and subsequent reemission in the FIR; and the shifting of peak

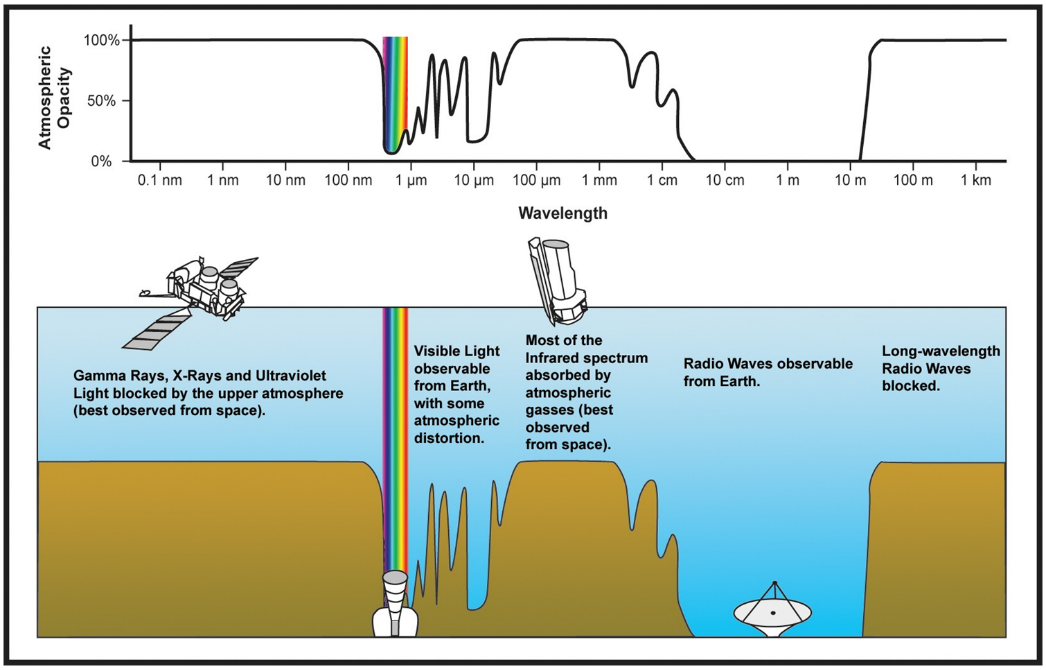

Figure 1.1: The transmission of earth's atmosphere over the UV to radio wavelength ranges. This diagram shows a high atmospheric opacity for most of the FIR and SMM wavebands, between 10 μm and 1 mm [3].

wavelengths of emission into the FIR for distant, redshifted galaxies.

FIR observations of the near universe are mainly concerned with studies of the interstellar medium. The interstellar medium which is made up of dust and gas, contains information on the composition and physical conditions necessary for star formation. Typically, interstellar dust is responsible for continuum emission, in the form of thermal radiation, which follows Planck's Law,

$$B_\lambda(\lambda, T) = \frac{2hc^2}{\lambda^5} \frac{1}{e^{\frac{hc}{\lambda k T}} - 1} \qquad (\mathrm{W\ sr^{-1}\ m^{-2}\ \mu m^{-1}}) \quad (1.2)$$

where k is the Boltzmann constant and T is blackbody temperature of the system. Continuum emission, with a temperature range on the order of 10 K to 100 K, has peak emission in the FIR, as determined by Wien's Law,

$$\lambda_{peak} = \frac{2900}{T}. \qquad (\mu\mathrm{m}) \quad (1.3)$$

While dust clouds block visible and ultraviolet radiation, they show a higher transmission to far infrared radiation. The FIR waveband can then be used to probe to constituents of the cloud, where shorter wavelength imaging would be unable to do so. Interstellar clouds consist of ionic, atomic, or molecular species, each of which emit unique spectral signatures in the FIR. Ionic spectral features are characteristic of high energy, ultraviolet radiation, typically from main sequence stars which are undergoing nuclear fusion. Since UV radiation does not penetrate interstellar clouds, ionic and atomic spectral signatures are manifested in a FIR spectrum as fine structure spectral lines, representing low energy transitions between split energy levels from spin orbit coupling. The intensities of these fine structure lines can be used to quantify the abundance of ionized species (NII, OIII) or atomic isotopes (^{13}C) with respect to neutral atoms (CI, NI, OI). The fact that low energy spectral lines can be used to observe high energy, ionizing processes, which would otherwise be obscured in the visible and UV, makes FIR spectroscopy a critical window in which to study these phenomena. Also, lightweight molecules, such as CO and HCN, have rotational transitions in the FIR. The illumination of these molecules leads to the excitation of these modes, leading to narrow wavelength absorption lines in the FIR, and subsequent emission lines as the molecules return to the ground state. Thus, the interstellar medium, as measured by a spectroscopic instrument, is characterized by continuum emission with narrow absorption and emission lines.

I will present three examples of different types of astrophysics that can be uniquely observed in the FIR. First, dense star-forming regions, which are obscured by residual dust clouds. Secondly, ultra-luminous infrared galaxies (ULIRGs), which are galaxies with a high rate of star formation, are discussed. Finally, highly redshifted galaxies allow us to observe the evolution of galaxies over cosmic time.

1.2.1 Star Forming Regions

Infrared astronomy offers a unique view of the interstellar medium, which is composed mainly of cold clouds of dust and gas. The gas consists mostly of hydrogen ($\sim 70\%$) and helium ($\sim 28\%$), but also heavier elements and compounds ($\sim 2\%$), and can exist in ionic, atomic, or molecular form depending on where it is found [7]. The dust, on the other hand, is composed mainly of silicates, carbon dust species, and organic compounds, such as polycyclic aromatic hydrocarbons (PAHs). Since these clouds obscured short wavelength radiation, FIR observations provide a unique view of the early stages of star formation.

As a particularly dense pocket of the interstellar medium begins to collapse under the force of its own gravity to form a star, gravitational potential energy is converted to kinetic energy, leading to an increase in temperature and pressure. The condition for the commencement of gravitational collapse is that the cloud must exceed a critical mass, known as the Jean's mass [8], leading to an instability where gravitational forces exceed the thermal pressure forces from the interior of the cloud. The Jean's mass can be expressed as,

$$M_J = \left(\frac{5kT}{G\mu}\right)^{3/2}\left(\frac{3}{4\pi\rho}\right)^{1/2} \quad \text{(kg)} \qquad (1.4)$$

where k is the Boltzmann constant, G is the gravitational constant, μ is the mass per particle, ρ is the mass density of the cloud. Note that M_J is proportional to $T^{3/2}$ and $\rho^{-1/2}$, meaning that cold, dense clouds have a lower critical mass, and are more likely to exceed the Jean's mass condition.

Heat generated from within the collapsing cloud is radiated away from the pre-stellar core in the form of thermal emission as the cloud continues to collapse. With low temperatures, and therefore, peak emission in the FIR, early stage pre-stellar cores show up as bright sources in far infrared surveys. By observing protostars in different environments, thereby capturing different stages of stellar evolution, we can understand the process of star formation. Since stars are the optical building blocks of galaxies, a complete grasp of star formation in all stages is critical to the understanding of galactic evolution [9].

1.2.2 Ultra-Luminous Infrared Galaxies

ULIRGS are galaxies which are unusually luminous in the FIR. These are galaxies which contain a large amount of interstellar matter, which is responsible for high thermal emission in the FIR. The luminous clouds are indicative of high energy thermodynamic processes obscured by the clouds. It is for this reason that ULIRGs are considered to be in a stage where they have a higher than normal star formation rate. Typically, a ULIRG will have a star formation rate (SFR) of at least 10 times the SFR in our own galaxy. Rapid star formation is thought to be due to the onset of large mechanical forces which trigger gravitational collapse in many areas of the interstellar medium simultaneously. These large forces are typically linked to galactic mergers [10]. ULIRGs typically exist in the redshift range $1 < z < 2$, meaning that they are younger galaxies than our own, in the intermediate stage between formation and settling into elliptical or spiral galaxies [10]. Many of these galaxies contain active galactic nuclei (AGN) which are obscured at shorter wavelengths, but are apparent because of the presence of fine structure lines in the FIR from highly ionized species. The correlation between the development of AGN and the onset of rapid star formation is a question that future study of these sources will address [9].

1.2.3 High-Z Galaxies

In the FIR wavebands, very highly redshifted galaxies are relatively easy to detect due to the negative K-correction factor. Negative K-correction is a result of the relative independence of brightness of a galaxy on redshift. Redshift is measured as a dimensionless quantity, z, which is related to a source wavelength, λ_{src} and the actual observed wavelength, λ_{obs} by the expression,

$$z = \frac{\lambda_{obs} - \lambda_{src}}{\lambda_{src}} \tag{1.5}$$

The redshift of a galaxy is indicative of the speed at which it is moving away from the observer. Due to the rate of expansion of the universe, redshift gives information on the distance, or look back time, between the galaxy and the observer, commonly expressed as Hubble's Law. With an increase in look back time, we expect a decrease in irradiance proportional to $(1+z)^{-2}$ due to the decrease in the solid angle subtended by the source. However, for a galaxy which emits peak thermal emission from main sequence stars in the optical and near infrared, the peak emission is shifted towards the FIR at increasing distance, leading to a relative independence of brightness of the source on distance (Figure 1.2). Utilizing this relatively easy detection rate of highly redshifted sources, along with sharp spectral features, redshifted into the far-infrared, the distance of the sources, and therefore look back time, can be measured. Observing the concentrations of molecular and atomic species at different eras in cosmological time is one of the chief goals of FIR astronomy.

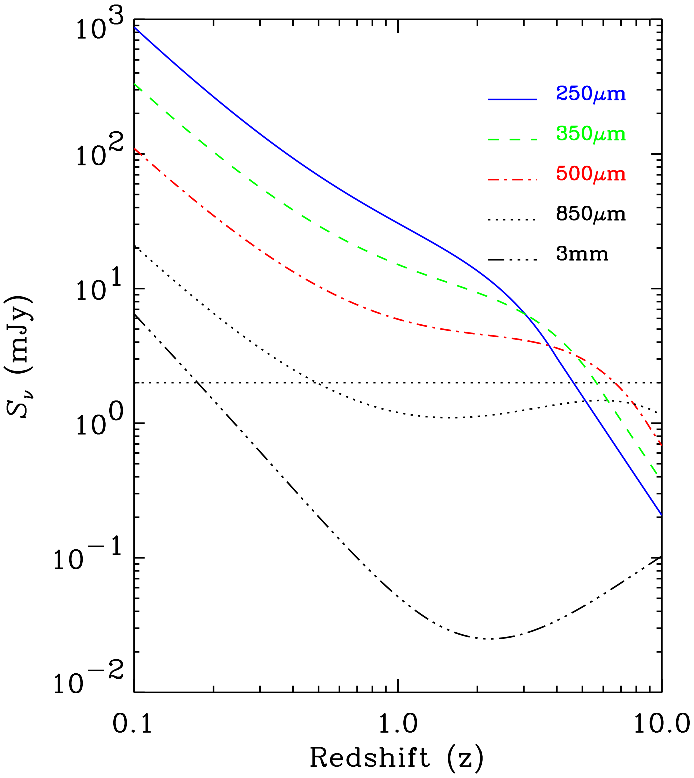

Figure 1.2: The negative K-correction compensates for the perceived dimming of objects as distance increases. For objects in the FIR/SMM, the peak of the blackbody emission spectrum is shifted into the observed waveband, leading to a weaker dependence of flux density on redshift. [9].

1.3 FIR Spectroscopy

Photometric observations can be obtained more quickly than spectroscopic observations, and are useful to determine the variation in emission over a wide area of sky. Photometric observations integrate flux over a broad spectral band determined by the instrument's spectral response profile, which is defined by its subcomponents (filters, etc.) and detector response. While this is sufficient to measure thermal emission, it will not reveal spectral features. High resolution spectroscopy is required to measure the intensities and widths of spectral lines, such as OI, CII, and the CO ladder.

Furthermore, imaging spectroscopy provides a solution for mapping large spatial regions with high resolution spectroscopy, providing information in two domains: the spatial and the spectral. Spatial sampling is achieved by detector arrays on the image plane, and further by moving the telescope to mosaic the sky. Spectral sampling is achieved with instruments which either separate photons by their wavelengths directly (eg. grating, prism) or by splitting the beam into multiple paths and interfering them with a known path difference (eg. Michelson, Mach-Zehnder, Martin-Puplett, Fabry-Perot) [11]. Most FIR observatories consist of both photometric and imaging spectroscopic instruments, providing access to sensitive intensity mapping of extended sources as well as detailed spectral information of point sources (eg. ISO [12], Spitzer [13], Akari [14], Herschel [15]).

1.4 Observing Challenges

As discussed previously, from an astronomical perspective, the FIR regime has remained largely unexplored, primarily due to the absorbing nature of the atmosphere. The chief atmospheric absorber of FIR radiation is water vapour. Since the atmosphere is absorbing in the FIR, the atmosphere also emits in the FIR. The emission of the atmosphere is a dominant source of noise for many ground-based FIR observatories. The low transmission of the atmosphere can be overcome by constructing high-altitude observing platforms, such as the James Clerk Maxwell Telescope (JCMT) on Mauna Kea, Hawaii [16]. These platforms are built in high and dry places where the column density of water vapour in the atmosphere is much diminished as compared to sea level. To achieve even lower levels of atmospheric emission, observatories are built at even higher altitudes. SOFIA is a high-altitude aircraft based observing platform which can get above the troposphere all together for even more precise measurements [17]. Ultimately, the best FIR observatories are located outside the atmosphere. Space-based observing platforms have been in place for over three decades and are continuing to provide increasingly superior results in the mid and far infrared bands.

The second challenge when observing in the FIR is that the photon energy is so low, that it is difficult to fabricate detectors with sufficient sensitivity. For a long period of time, detector technology was inadequate to provide the necessary sensitivity. There exists two principle types of detectors. These are classified into photon and thermal detectors. Photon detectors, as the name suggests, respond to the incident photons by exciting free charge carriers. The wavelength response is determined by the bandgap energy of the semiconducting detector material. Unfortunately, the low energy of FIR photons preclude the use of photon detectors. The required band gap is so small that thermal agitation will cause electrons to cross the bandgap, contributing to the detector noise. To detect FIR photons, a thermal detector must be used. The second type of detector is the thermal detector (eg. bolometer). Here, radiation is absorbed by the detector and the resulting temperature change is measured by a sensitive thermometer. These detectors have a broader spectral coverage because they are not limited by electronic bandgaps. Since the sensitivity of bolometer detectors is due to the ability to detect a small change in temperature, cryogenic detectors offer the best advantage, because of their superior sensitivity to incident power (expressed as noise equivalent power) [9]. With the application of cryogenics in detector technology, one can also utilize superconducting materials which have a very sharp resistive transition at cryogenic temperatures, making them extremely sensitive to small temperature changes. Only recently have we have achieved detector sensitivities on order of $10^{-19}\ \mathrm{W}/\sqrt{\mathrm{Hz}}$ [18].

Detectors with such a high sensitivity necessitate instruments which are also cryogenically cooled, typically to liquid helium temperatures, so as not to be a dominant source of thermal emission themselves. The combination of low temperature instrumentation and sensitive detectors, which will be used in future missions such as SPICA [19], have sufficient sensitivity that detection is not limited by the detector sensitivity, but by the background zodiacal and galactic cirrus emission [18] (Figure 1.3).

1.5 Cryogenics in Space

From the above discussion, it should be clear that the ultimate sensitivity of observations in the FIR can only be achieved by placing large telescopes in space, operating at cryogenic temperatures, with extremely sensitive detectors. Drawing upon the success of past FIR missions such as IRAS [20], ISO [12], AKARI [14], Spitzer [13], and Herschel [15], there are now two missions under development that will employ active cooling of the telescope optics and instrumentation to $<6\,\mathrm{K}$ to achieve background radiation levels on the same order of magnitude as the cosmic microwave background (CMB). SPICA is a joint venture led by JAXA and ESA [19], and CALISTO is a cryogenic FIR observatory led by NASA [21].

With a sufficiently cold telescope, background limited performance of a FIR instrument may be achieved. A decrease in intensity of telescope emission of 10^6 as compared to Herschel, as shown in Figure 1.3, will manifest itself as an increase in signal-to-noise ratio (SNR) of 10^3 with sufficiently sensitive detectors.

The utilization of low temperature instrumentation in a space environment, where servicing and repair is impossible, requires extensive laboratory testing of the instrument so that its performance is thoroughly understood. Testing facilities which are capable of achieving cryogenic temperatures are necessary for this task. I have been involved in the design, construction, and certification of a cryogenic facility at the University of Lethbridge for the testing of instrument components in future FIR missions. This thesis presents the design, construction, and performance validation of a cryogenic test facility that has been developed for this specific purpose.

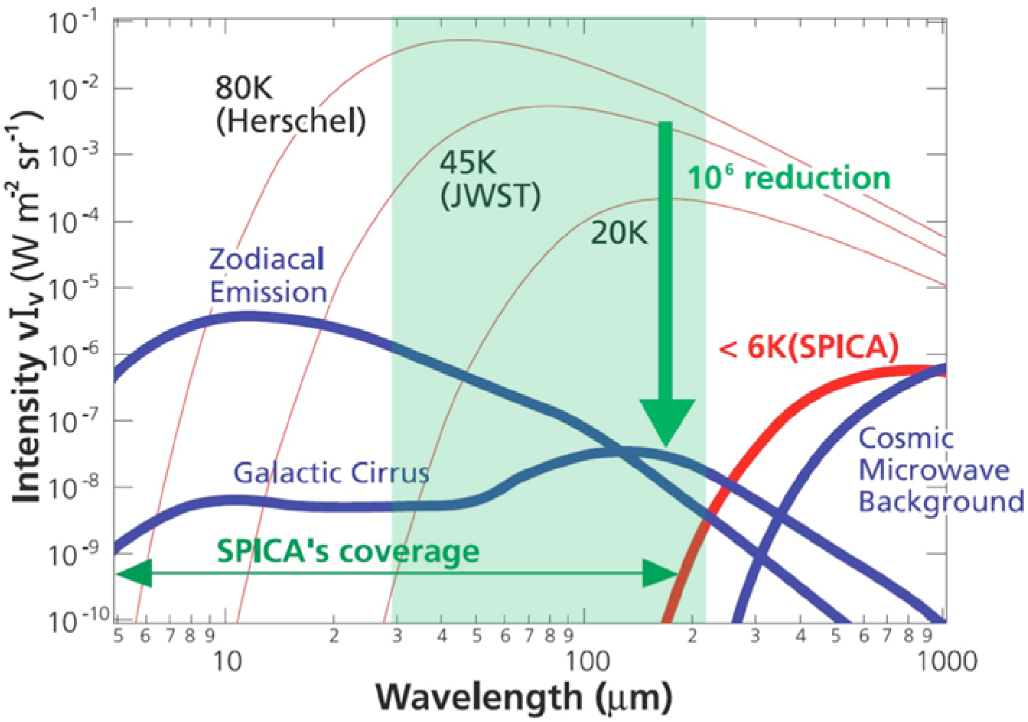

Figure 1.3: Thermal emission estimates for the <6 K SPICA telescope are shown in relation to the thermal emission of Herschel and the developing JWST, as well as common galactic regions. The 10^{-6} reduction in intensity of thermal emission for SPICA as compared to Herschel puts the thermal emission of SPICA below the background emission levels along the plane of the Solar System and the Milky Way [22].

Table 1.1: Overview of FIR space observatories.

Mission	Agency	Launch Date	Diameter [m]	Waveband [μm]	Operational Temp. [K]	Location	Instruments	Source
IRAS	NIVR NASA SERC	January 26, 1983	0.57	7.5 - 100	$<$10	low earth orbit (900 km)	LRS, CPC	[20]
ISO	ESA	November 17, 1996	0.60	2.5 - 240	3	elliptical earth orbit (70 600 km max)	ISOCAM, ISOPHOT, LWS, SWS	[12]
Spitzer	NASA	August 25, 2003	0.85	3.6 - 160	5.5	solar orbit	IRAC, IRS, MIPS	[13]
AKARI	JAXA	February 21, 2006	0.71	2 - 180	5.8	low earth orbit (700 km)	FIS, IRC	[14]
Herschel	ESA	May 14, 2009	3.5	55 - 671	85	L2	HIFI, PACS, SPIRE	[15]
JWST	NASA	2018	6.6	0.6 - 29	$<$50	L2	NIRCam, NIRSpec, TFI, MIRI	[23]
SPICA	ESA/JAXA	2022	3.2	5 - 210	$<$6	L2	MCS, SAFARI, FPC, SCI	[18]
CALISTO	NASA	–	5	35 - 650	4	L2	–	[21]

Chapter 2

Material Properties at Low Temperatures

As discussed in Chapter 1, to exploit the sensitivity of modern detectors at FIR wavelengths, instrumentation must be cooled to around 4 K so that self emission is not a dominant source of photon noise. Large volume, cryogenic facilities are required for testing both components and integrated systems at low temperatures.

At room temperature, we have a thorough understanding of material properties; it is even the case that for most materials, their properties can be predicted and are modelled with high accuracy. Theoretical models rely on assumptions which may not hold at cryogenic temperatures, resulting in increased uncertainties. Therefore, the only way to understand the properties of materials at low temperatures is to measure them.

The parameters we are interested in are specific heat, thermal expansion, electrical/thermal conductivity, and a variety of mechanical properties. An undergraduate may wrongly infer that these properties are constant for any material, that is to say, independent of temperature; this is not the case. One of the first things that is realized in the field of cryogenics, is that predicting material properties at low temperatures from their room temperature values results in inaccurate values. In fact, properties of materials generally have a very strong temperature dependence which is not readily apparent in a room temperature setting. For example, epoxy is generally used to adhere pieces together and is considered to be a substance with a fairly high ductility, which is not the case at cryogenic temperatures. Below room temperature, many forms of epoxy undergo a ductile-to-glass transition which causes

Table 2.1: Heat capacity terminology, definitions, and units. Note that since many terms are represented by the same symbol, the term used must be emphasized.

Term	Definition	Units	Symbol
Heat Capacity	heat capacity of a system/object	$\mathrm{J\,K^{-1}}$	C
Specific Heat Capacity	heat capacity per unit mass	$\mathrm{J\,m^{-1}\,K^{-1}}$	c
Molar Heat Capacity	heat capacity per mole	$\mathrm{J\,mol^{-1}\,K^{-1}}$	c
Volumetric Heat Capacity	heat capacity per unit volume	$\mathrm{J\,m^{-3}K^{-1}}$	c

them to become brittle and thus prone to cracking when under stresses, which are commonly caused by thermal gradients in the system [24]. Special care must be taken to select epoxies that retain their ductility over the cryogenic temperature range. In general, the selection of materials for cryogenic use is limited to a small pool of materials for which there exists well-tabulated measurements of their properties. Appendix A lists properties of many common materials which are used at cryogenic temperatures.

2.1 Specific Heat

Specific heat is the measure of the energy per unit mass required to change the temperature of the material by one degree. A number of other similar terms may be used to describe similar phenomena, which are summarized in Table 2.1. In this section, we will discuss derivations in terms of heat capacity. The transcription to specific heat can be made by dividing by mass. Knowledge of heat capacity can be used, for example, to estimate the time it would take for an integrated system to cool to 4 K. In general, cryogenic instruments are made with materials having a low specific heat in order to minimize cooling time. Materials with a high specific heat may be used in special cases, but their geometry is configured so that the overall heat capacity of the component remains low.

Heat capacity is defined in two different ways depending on which constraint, either pressure or volume, is kept constant as heat is added to the material. Heat capacity at constant volume is usually described as “energy capacity [25],”

$$C_V = \left(\frac{\partial E}{\partial T}\right)_V = T\left(\frac{\partial S}{\partial T}\right)_V, \qquad (\mathrm{J\ kg^{-1}\ K^{-1}}) \quad (2.1)$$

representing all the heat being stored as internal energy. Heat capacity at constant volume is usually the parameter that is determined by theory as it ignores the volume change of a material by thermal expansion. In practice, the heat capacity of a solid must be measured at constant pressure, since thermal expansion of a material must be taken into account. Heat capacity at constant pressure is expressed as [25],

$$C_P = \left(\frac{\partial H}{\partial T}\right)_P = \left(\frac{\partial E}{\partial T}\right)_P + P\left(\frac{\partial V}{\partial T}\right)_P, \qquad (\mathrm{J\ kg^{-1}\ K^{-1}}) \quad (2.2)$$

where H is the enthalpy. This is often referred to as “enthalpy capacity,” and it can easily be seen in the above equation that this accounts for the energy required to move the surroundings away from the material as it thermally expands, in addition to the change in internal energy. As we will see in the following section, the thermal expansion of a material is small at cryogenic temperatures, therefore, the difference between C_P and C_V is often negligible.

There are various elements of a material that can contribute to the specific heat, with two contributions being significant. The most significant contribution to specific heat at room temperature is vibrations of the solid lattice, or phonons. However, the contributions from electronic specific heat cannot be ignored, especially at low temperatures. In fact, electronic specific heat becomes the dominant contribution below around 4 K, for highly conductive materials such as copper [26]. Other contributors to specific heat are nuclear specific heat and Schottky specific heat, which are only significant for magnetic materials at ultra-low temperatures (ie. less than 1 K) and will not be discussed further [26]. To first approximation, the contributions to total specific heat by each element can be expressed as a sum, and any interaction between them is ignored [26].

2.1.1 Lattice Specific Heat

At high temperatures, the specific heat of a material always approaches a constant value. In fact, the molar specific heat is approximately the same for any metallic material (ie. a material with a regular crystal lattice). This is known as the Dulong and Petit limit [26]. The derivation of this limit can be seen from simple kinetic theory. For a 3-D solid lattice, there are six vibrational degrees of freedom, three kinetic and three potential, which means that change in internal energy is realized by the equipartition theorem as [26],

$$\Delta U = \frac{1}{2} f N k \Delta T = 3 N k \Delta T. \qquad \text{(J)} \quad (2.3)$$

where f is the number of degrees of freedom of each molecule/atom, N is the number of molecules/atoms in the material, k is the Boltzmann constant in J K^{-1}, and ΔT is the change in system temperature. Using Equation 2.3 to determine heat capacity [26],

$$C_V = \frac{\Delta U}{\Delta T} = 3Nk = 3nR \qquad (\text{J K}^{-1}) \quad (2.4)$$

where n is the number of moles of molecules/atoms, and R is the universal gas constant in J K^{-1} mol^{-1}. Therefore the molar specific heat is a constant value [26],

$$c_V = 3R. \qquad (\text{J mol}^{-1}\text{K}^{-1}) \quad (2.5)$$

At low temperatures, however, the relatively simple model of Dulong and Petit breaks down and specific heat becomes temperature dependent and varies widely among materials. Below around 100 K, specific heat falls off as $\sim T^3$, approaching zero as T goes to 0 K, following the third law of thermodynamics [25]. The reason for the decrease in specific heat originates from the Einstein solid theory, which treats a solid as an arrangement of quantum harmonic oscillators. Due to the Heisenberg uncertainty principle, the lowest energy an oscillator at frequency ν can have is $E = \frac{1}{2}h\nu$ [27]. This ground state energy equates to a characteristic temperature, $T_c = E/k$, below which the oscillator cannot reduce

Table 2.2: Debye Temperatures of common pure elements used in cryogenics [28].

Element	Debye Temperature θ_D (low temperature limit)
Aluminum	428 K
Copper	343 K
Gold	170 K
Iron	470 K
Nickel	450 K
Platinum	240 K
Sapphire	1047 K
Silver	215 K
Titanium	420 K

energy any further and therefore does not contribute to specific heat. According to the third law of thermodynamics, once all quantum oscillators are in the ground state, the specific heat effectively becomes zero [25].

The Debye theory estimates the phonon contribution to heat capacity of a material as [26],

$$C_V = 9Nk\left(\frac{T}{\theta_D}\right)^3 \int_0^{\theta_D/T} x^4 e^x (e^x - 1)^{-2} dx, \qquad (\mathrm{J\ K^{-1}}) \quad (2.6)$$

where x is the unitless quantity,

$$x = h\nu/kT. \quad (2.7)$$

The derivation of Equation 2.6 is based on the elastic-continuum model of a solid, in which energy is considered as being stored in the vibrational modes of the crystal lattice, and the lattice elements are treated as interacting quantum oscillators [24]. In the Debye theory, θ_D represents the *Debye temperature*, a material specific constant which quantifies the temperature at which all quantum oscillators are above the ground state [26]. The Debye temperatures of some common elements used in cryogenics are listed in Table 2.2.

For cryogenic temperatures, where $T << \theta_D$, the upper boundary on the integral goes to ∞ and the integral in Equation 2.6 has a solution, $4\pi^4/15$. In these low temperature conditions, molar heat capacity has a cubic dependence on temperature, given by [24],

$$C_V(T) = \frac{3\pi^4 Nk}{5}(T/\theta_D)^3. \qquad (\mathrm{J\ mol^{-1}\ K^{-1}}) \quad (2.8)$$

For conductive materials, this cubic equation matches experimental data with $1-2\%$ error up till about $\theta_D/10$, where the contribution due to electrons becomes significant [26].

2.1.2 Electronic Specific Heat

As the vibrational modes of a crystal lattice approach the ground state, the specific heat of a material should level out as T^3. Experimental data shows that the dependence evolves to introduce a linear T term. This is characteristic of the specific heat of the electrons in the material. The linear dependence is derived from Fermi-Dirac statistics which means that only electrons with energies that lie within kT of ε_0, which represents the Fermi energy of the electrons, will receive sufficient energy to change levels [26]. The number of electrons which will change energy is defined as [26],

$$n = kTF(\varepsilon_0), \qquad (2.9)$$

where $F(\varepsilon_0)$ is the energy density of states. Each electron will receive energy $\frac{3}{2}kT$ and differentiating that energy with respect to temperature gives the heat capacity per electron [26],

$$c_e = 3k^2TF(\varepsilon_0). \qquad (\mathrm{J\ K^{-1}}) \quad (2.10)$$

The molar specific heat at low temperatures is generally fit to the polynomial,

$$c(T) = \gamma T + \frac{1944}{\theta_D^3}T^3. \qquad () \quad (2.11)$$

To account for the combination of the cubic and linear terms, specific heat at low temperatures is often expressed in graphical form as c/T vs T^2 and fit with a linear regression in order to measure γ and θ_D [29].

2.2 Thermal Expansion

Thermal expansion of materials is a critical parameter in the design of cryogenic instrumentation. Large temperature changes and thermal gradients can lead to dimensional changes which impose high stresses on components. One of the main strategies used in instrument design is the matching of thermal expansion between materials which are joined together. Near room temperature, the rate of linear thermal expansion is a constant [24],

$$\alpha = \frac{1}{L}\frac{\Delta L}{\Delta T}, \qquad (\mathrm{K}^{-1}) \quad (2.12)$$

where L is the length of the object, ΔL is the change in length associated with a change in temperature, ΔT. Matching thermal expansion then becomes a trivial task of selecting materials with a similar coefficient of thermal expansion (CTE), α. However, at cryogenic temperatures, thermal expansion is temperature dependent in much the same way as lattice specific heat.

The CTE of a solid is proportional to the specific heat of the material in most cases, especially in crystalline solids where the dominant source of heat capacity for $T \geq \theta_D/10$ is lattice vibrations [24]. The primary reason for the connection between the two properties is the anharmonicity of the lattice vibrations as higher vibrational modes are excited, leading to an increasing mean separation of the lattice constituents as temperature is increased [26]. The constant of proportionality between the specific heat and the CTE of a material is defined as the Grüneisen parameter, γ, [30]:

$$\gamma = \frac{3B\alpha}{c_V} \quad (2.13)$$

where B is the bulk modulus which does not change much with temperature [26]. Since the CTE is proportional to the specific heat, at low temperatures, well below θ_D, it follows

T^3 for insulators and T for conductors. At high temperatures, CTE approaches a constant value. With a variable rate of thermal expansion, it becomes useful to measure the total thermal linear expansion from room temperature to T rather than the CTE [24],

$$\frac{\Delta L}{L} \equiv (L_T - L_{293})/L_{293}. \tag{2.14}$$

Note that the derivative of the above equation with respect to temperature is the temperature dependent CTE, given in Equation 2.12.

Considering thermal expansion from room temperature to cryogenic temperatures, materials are classified into four groups based on their thermal expansion ranges. Organic materials consisting of long chain polymers routinely have the highest thermal expansion at around $1-2\%$ linear contraction from room temperature to 4 K. Next, pure metals exhibit a total contraction of around $0.2-0.4\%$. The materials with the lowest thermal contraction glasses and low thermal expansion alloys with a $< 0.1\%$ dimensional change. The thermal expansion of these three categories is shown in Figure 2.1. The final category belongs to a recently developed group of materials known as composites. These materials may be created by combining two materials to exploit the favourable properties of both. Since these materials are manufactured, their thermal expansion may be designed based on the volume density and orientation of constituent materials. Composite materials have been developed to have extremely small and even negative thermal expansion [24, 31].

2.3 Electrical Conductivity

The following two sections are dedicated to transport of energy in materials in the form of electrical current and heat flow. The mechanisms behind both types of transport properties are intertwined, which is evident in the fact that a potential difference or a thermal gradient across a conductive material induces both a current and a heat flow [30]. In this case, the similarities arise from electrons being the energy carrier for both processes. Electrons are the primary charge carrier for electrical current, and together with phonons, are

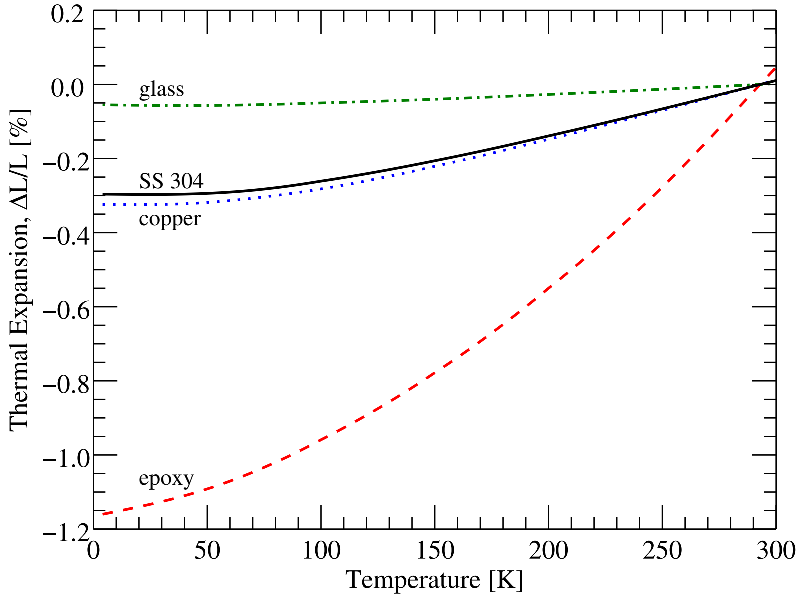

Figure 2.1: Thermal expansion of selected cryogenic materials showing the three ranges of thermal expansion values (not including composite materials). Thermal Expansion values were taken from [32].

the major energy carriers for heat transport.

Electrical conductivity, σ, is a measure of the current induced in a material in the presence on an electric field, $\mathbf{E}$. It is defined as the reciprocal of the resistivity of the material, ρ [30],

$$\mathbf{E} = \rho\mathbf{j} = \frac{\mathbf{j}}{\sigma}. \qquad (\mathrm{N\,C^{-1}}) \qquad (2.15)$$

where the current density, $\mathbf{j}$, is defined as [30],

$$\mathbf{j} = -ne\mathbf{v}, \qquad (\mathrm{C\,s^{-1}\,m^{-2}}) \qquad (2.16)$$

where n is the number of charge carriers, e is the electric charge per carrier, and $\mathbf{v}$ is the average charge carrier velocity, or *drift velocity*. Also, under the assumption that an electron scatters from the lattice elements, and that the velocity after a collision is in a random direction, the electron velocity is dependent on the force of the electric field on the electron, $F = -e\mathbf{E}$, the average time between collisions, τ, and the mass of the electron, m_e [30],

$$\mathbf{v} = -\frac{e\mathbf{E}\tau}{m_e}. \qquad (\mathrm{m\ s^{-1}}) \qquad (2.17)$$

Combining Equations 2.15, 2.16, and 2.17, the electrical conductivity is derived as [30],

$$\sigma = \frac{ne^2\tau}{m_e} = \frac{ne^2\lambda}{m_e v}, \qquad (\mathrm{S\ m^{-1}}) \qquad (2.18)$$

where λ is the average distance between collisions, or *mean free path*, and v is the magnitude of the electron velocity.

There are two scattering mechanisms that play a role in determining the mean free path of the electron. The first is electron scattering resulting from interactions with phonons. Since phonon energies are extremely temperature dependent (see Section 2.1.1), this form of scattering is also temperature dependent and dominates in the high temperature domain. This represents the electrical resistivity, $\rho_{ph}(T)$, of a material if no lattice defects are present [24]. The second type of scattering is electron scattering from lattice imperfections. This determines the electronic mean free path within a material that would be present as T approaches 0 K when phonon scattering is ”frozen out”, or becomes negligible. This type of scattering leads to a residual resistivity, ρ_{res} [24].

To a good approximation, both scattering mechanisms can be summed together, ignoring any interaction between them. This is known as Matthiessen’s rule [24], expressed as,

$$\rho(T) = \rho_{res} + \rho_i(T) \qquad (\Omega\ \mathrm{m}) \qquad (2.19)$$

The purity of a metal is usually expressed in the form of the residual resistivity ratio (RRR), defined as,

$$\mathrm{RRR} = \rho_{293\,\mathrm{K}}/\rho_{4\,\mathrm{K}}. \tag{2.20}$$

where $\rho_{293\,\mathrm{K}}$ is the resistivity of the material at room temperature and $\rho_{4\,\mathrm{K}}$ is the resistivity at 4 K, analogous to ρ_{res}.

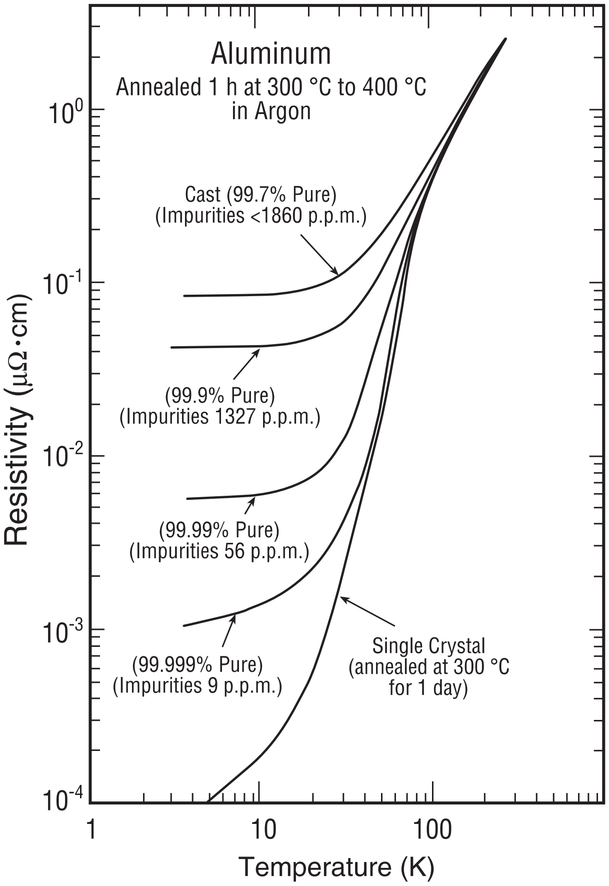

Figure 2.2: The electrical resistivity of aluminum with different purities as a function of temperature. Each resistivity curve approaches a constant, ρ_{res} as temperature approaches zero [24].

In general, pure metals have high electrical conductivity since the defects present in the material are minimal and therefore the mean free path of the electron is large. In addition, the purer the metal, the higher the electric conductivity at cryogenic temperatures, represented by a higher RRR. Figure 2.2 shows the difference in electrical resistivity at cryogenic temperatures for aluminum of different purities. A metal alloy, which will have other elements dispersed within the crystal lattice, will by nature have a lower electrical conductivity.

Insulating materials, on the other hand, have very low electrical conductivity, and generally a low thermal conductivity, because of the lack of free electrons. However, there is a class of insulating materials with high thermal conductivity, from enhanced phonon transport. These properties are observed only in insulators with a regular crystal lattice, such as diamond or sapphire.

2.4 Thermal Conductivity

The thermal conductivity of a material is a measure of the rate of heat transport through the material when exposed to a temperature differential. When faced with designing a cryogenic system which subtends a 300 K differential over a relatively short distance, this is arguably the most important property to consider when selecting materials. In the most basic sense, heat flow can be expressed by Fourier's Law in its 1-D form [24]:

$$\frac{\partial Q}{\partial t} = -\lambda A \frac{\partial T}{\partial x} \qquad \text{(W)} \qquad (2.21)$$

From the above equation, the rate of heat flow through the material is a product of the thermal conductivity, λ, the cross-sectional area, A, and the spatial derivative of temperature, $\frac{\partial T}{\partial x}$. Also, heat flows antiparallel to the temperature gradient, as represented by the negative sign. The thermal conductivity of a material is temperature-dependent and can vary by many orders of magnitude between 4 K and room temperature. In this case, the rate of heat flow through a macroscopic material in 1-D can be expressed by integrating the above equation between the upper and lower temperature boundaries [24],

$$\frac{\partial Q}{\partial t} = -\frac{A}{L}\int_{T_1}^{T_2} \lambda(T)dT. \qquad \text{(W)} \qquad (2.22)$$

This integral form of Fourier's Law is useful in calculating thermal transport over the cryogenic temperature range. Values for the thermal conductivity integral have been tabulated for many materials and temperature ranges, and are available in most cryogenic reference books [24]. The thermal conductivities of common materials, which I have used in this thesis, are included in Appendix A.

The electrons which are responsible for transporting charge within the material also play a role in the transport of heat. In addition, a second mechanism for the transport of heat is provided by phonons. Electronic heat transport dominates for pure metals and phonon heat transport dominates for insulators with alloys and semiconductors relying on a combination of electron and photon transport for heat conduction. As with electrical conductivity, the different scattering processes are assumed to act independently of each other, meaning the total thermal conductivity is the linear sum of the contributions by each carrier.

For pure metals, almost all the heat is conducted through the material by free electrons. Therefore, a very good approximation of the thermal conductivity can be made by applying a proportionality constant to the electrical conductivity since each electron will transport both charge and heat. The proportionality constant is the Lorenz number, L_N, from the Wiedemann-Franz-Lorenz law [24],

$$\frac{\lambda_e}{\sigma_e T} = L_N \approx 2.44 \times 10^{-8} \qquad (\mathrm{V}^2/\mathrm{K}^2) \qquad (2.23)$$

The Lorenz number holds to within a few percent at room temperature, where the dominant electron scattering process is by phonons, and at 4 K, where lattice imperfection scattering dominates, but does not hold at intermediate temperatures. This is because low energy phonon-electron interactions are much better at limiting heat flow than electrical charge, resulting in an estimate for thermal conductivity that is too high [24].

Thermal conductivity for insulators and transition metals at low temperatures is primarily dependent on phonon transport. Thermal conductivity of these materials is limited by the scattering of phonons in phonon-phonon interactions at higher temperatures and phonon scattering off lattice irregularities at low temperatures [24]. In practice, phonon heat transport is difficult to predict, but is more efficient in materials with an ordered crys-

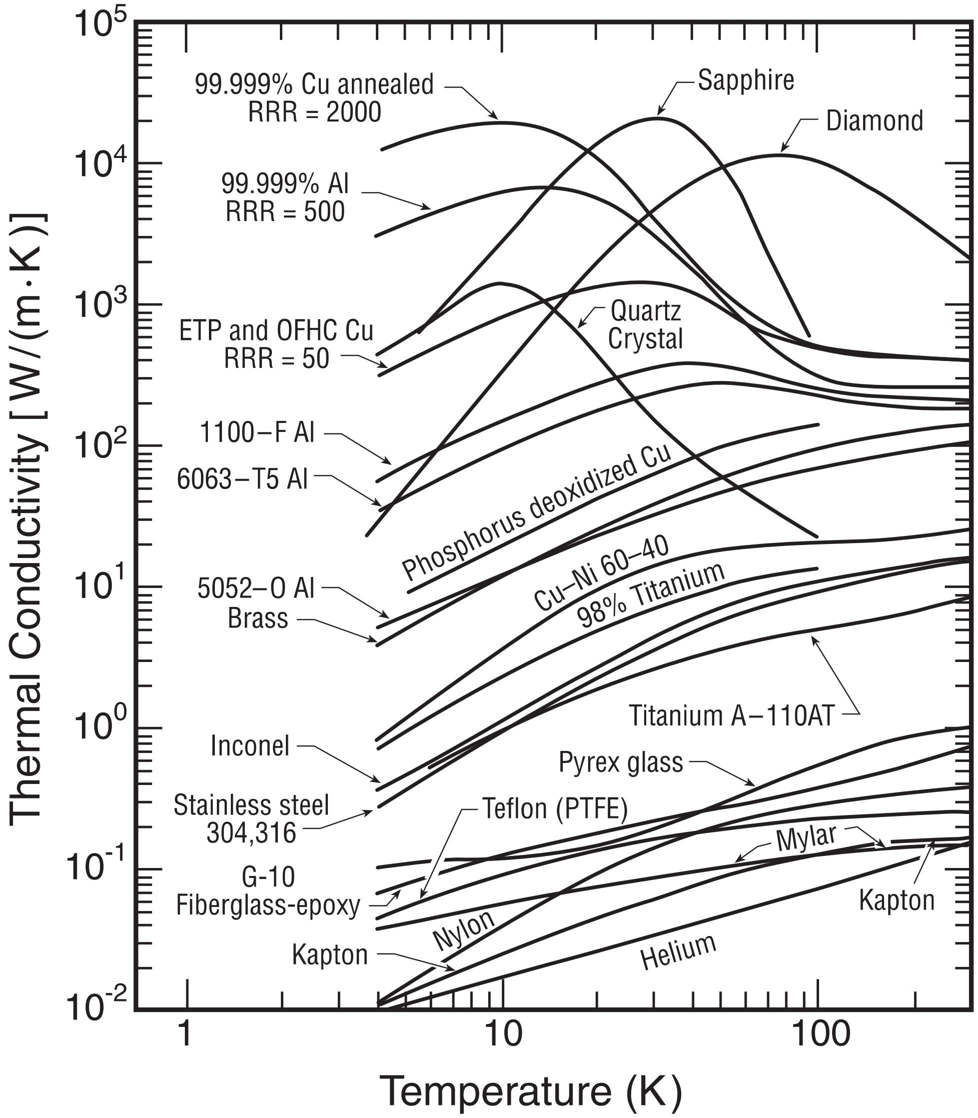

Figure 2.3: Temperature-dependent thermal conductivity for a variety of materials which are commonly used in cryogenics [24]

tal structure. This means insulating crystals, such as diamond and sapphire, have a very high thermal conductivity, while exhibiting a low electrical conductivity, making these materials very useful as sample holders for materials that must be in good thermal contact but must be electrically isolated. Other insulating materials with a disordered structure, such as glass and plastics, have a very low thermal conductivity [24]. The thermal conductivities of a variety of common cryogenic materials is shown in Figure 2.3.

2.5 Mechanical Properties

Mechanical properties are important in cryogenic instrumentation design because an inappropriate selection of materials may result in a system that deforms, or in the worst case, fractures, leading to potentially catastrophic failures. The mechanical properties of interest for cryogenic design are fracture toughness, elastic modulus, fatigue, and creep.

2.5.1 Fracture Toughness

When considering mechanical properties of materials, there is a very clear distinction which needs to be made between strength and toughness. Strength is maximum stress (force per unit area) that can be applied to a material before it deforms permanently (plastically) or fractures. For example, the yield strength of a material is the stress beyond which the material deforms plastically, and the ultimate strength is the pressure beyond which the material fractures, both of which are displayed in Figure 2.4. On the other hand, toughness describes the ability of a material to absorb energy from a pressure load without fracturing. Toughness is a measure of both the elasticity and ductility of a material, and expressed as the area under the curve in Figure 2.4. In order for a material to be considered tough, it must have a high strength and high ductility.

Fracture toughness represents the amount of energy per unit volume a material with a preexisting fracture can absorb before the fracture propagates. It is the most important property to consider when selecting materials because the presence of cracks in a material cannot be predicted theoretically, and therefore provide a risk for catastrophic failure which cannot be accurately predicted by stress-strain models. In cryogenics, materials are chosen that have a high fracture toughness at low temperatures. Metals which exhibit a face centred cubic (f.c.c.) crystal structure, such as aluminum, copper, and austenitic stainless

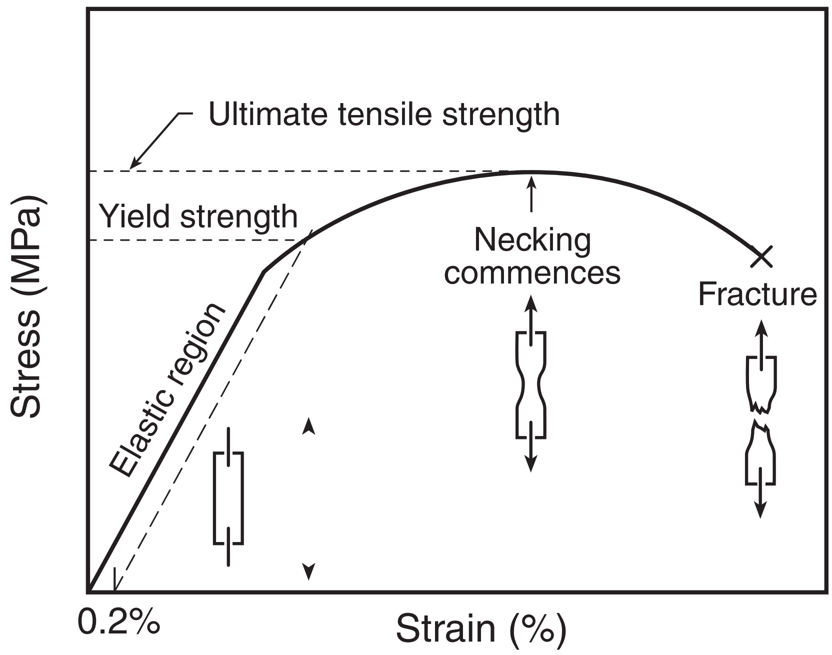

Figure 2.4: A stress-strain curve which is characteristic of ductile materials [24].

steels, show exceptional resistance to fracturing at low temperatures while other materials, with a body centred cubic (b.c.c.), such as iron and ferritic stainless steels, for example (Figure 2.5), show a large drop in fracture toughness below around 100 K [24]. This limits the choice of materials for cryogenic structures to materials like aluminum and copper. The mechanical properties of these common materials is shown in Appendix A.

Composite materials, which are discussed in Chapter 4, are generally constructed from materials which are brittle at low temperatures, such as epoxy and graphite. However, since the epoxy is reinforced with many small diameter fibres, the strength of the material remains unchanged when a few individual fibres fracture. Therefore, the overall fracture toughness of the material is much greater than that of its constituents.

2.5.2 Elastic Modulus

When subject to an external force, in the absence of cracks, a material will deform following a predictable stress-strain curve. Figure 2.4 shows the stress-strain curve for a ductile material. The deformation regions of the curve are split into two sections: the elas-

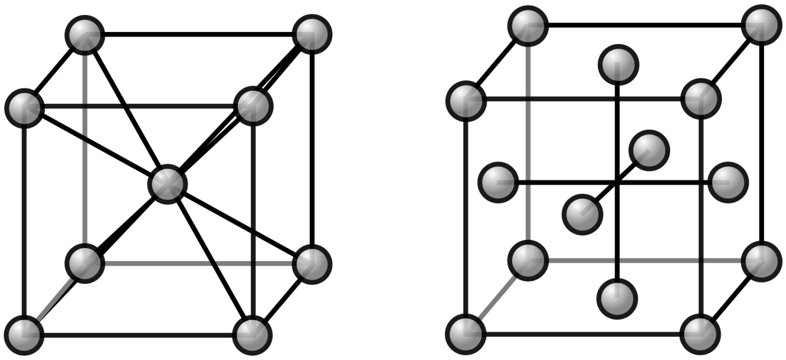

Figure 2.5: A schematic showing a body centered cubic strucutre (left) and a face centered cubic structure (right) [33].

tic deformation region and the plastic deformation region. In the elastic deformation, the stress is directly proportional to the percentage deformation, or strain. The proportionality constant is the elastic modulus, given by,

$$E = \frac{\text{stress}}{\text{strain}} \qquad \text{(GPa)} \tag{2.24}$$

When in the elastic deformation region, the object will return to its original shape when the stress is removed. If the stress on the object exceeds the yield strength of the material, the material will undergo a plastic deformation. The strain at which the yield strength is reached is known as the *elastic strain limit*. If the stress is still increased on the object, eventually the object will break upon reaching the ultimate strength, or the fracture point. If the fracture point is close to the yield point, the object is brittle [24]. For example, glass is a brittle material which does not experience much plastic deformation before fracturing. If the object has a large plastic deformation region, the object is ductile [24]. Examples of ductile materials used in cryogenics include copper, aluminum, and steel.

There are a number of different elastic moduli, which may have vastly different values, which must be considered. When the stress is normal to the cross-sectional area of the material, the modulus is the *tensile modulus* or *compressive modulus* depending on the direction of the stress. When considering the application of stress from all sides of the material equally, the *bulk modulus* is used. Finally, when considering a stress that is parallel to the cross-sectional area, the *shear modulus* is used. For the vast majority of situations, we consider the strain on a support structure that is under a tensile or compressive load.

Although differing, the tensile and compressive moduli of a material are assumed to be constant. However, experimental tests have shown that in metals, there is a weak temperature dependence, resulting in a change in the elastic modulus by a few percent when cooled to cryogenic temperatures [26]. This temperature dependence tends to disappear as temperature decreases, following the third law of thermodynamics. In general, tensile and compressive strength and modulus of materials both increase by a few percent as the material is cooled. In practice, mechanical properties of systems determined from room temperature measurements are assumed to hold to within a few percent at cryogenic temperatures [24].

2.5.3 Fatigue

Fatigue is the measure of the number of times an object can be stressed before it fractures, expressed as fatigue life. Fatigue life depends on a number of different variables including the stress magnitude, the fracture toughness, and the ductility of the object. In practice, the fatigue life of a sample is also dependent on the composition of the material and on the type of heat treatment or cold work applied to the material. As such, fatigue life is difficult to predict analytically and is therefore measured experimentally. Fortunately, like the elastic properties of a material, the fatigue life tends to improve with lower temperatures. The exception to this case is materials that undergo a ductile-to-brittle transition as temperature decreases. This transition is common in materials which a b.c.c. crystal structure, such as iron. Although a strong structural material at ambient temperatures, iron becomes brittle at low temperatures. For materials that don't experience a ductile-to-brittle transition, of which f.c.c. materials such as aluminum and copper are the prime example, the fatigue curves for a material can then be measured at room temperature for cryogenic instrumentation and these values can be used as an estimate for the cryogenic performance [24].

2.5.4 Creep

The creep of a material is a measure of the plastic flow of the material when under a constant stress for a period of time. Creep can occur even if the applied stress is well below the yield strength of the material. Generally, creep is not a significant factor for metallic structural materials in cryogenics. However, certain polymeric materials, such as the resin used in fibre-reinforced composites (FRPs), may experience significant creep. This must be accounted for when selecting the polymer to use for fabricating FRPs. The topic of selecting appropriate polymers is discussed further in Chapter 4.

2.6 Conclusion

In practice, the temperature-dependence of material properties is a subject that relies heavily on a strong background knowledge in solid state theory. Even so, successful theoretical models are often simplifications and can only hold for materials with a well known, continuous lattice structure. This limits our theoretical understanding of materials to mainly the pure metals. As we have seen, materials which are required for low electrical/thermal conductivity or low thermal expansion will not be pure metals and therefore, their properties cannot be predicted accurately. Therefore, handbooks exist which list experimentally determined properties of materials over wide temperature ranges. In the following chapters, the selection of materials for cryogenic instrumentation will be based on handbook values, which are reported in Appendix A, rather than theoretical values.

Chapter 3

The Test Facility Cryostat

In June 2014, the Astronomical Instrumentation Group (AIG) secured funding from the Canadian Foundation for Innovation (CFI) for the construction of a large cryogenic test facility. The goal of the so-called Test Facility Cryostat (TFC) was to provide the capacity to cool large volumes, up to 70 L, to 4 K, and perform measurements and metrology from various angles. The goal was to not only measure optical, mechanical, thermal properties of components but also integrated systems, such as the SPICA/SAFARI instrument. In this chapter, I will outline my involvement in the design of the TFC including mechanical and heat analysis, layout requirements, final assembly, and verification of system performance.

3.1 TFC Design

The design of cryogenic facilities generally revolve around the management of the three modes of heat transport: conduction, convection, and radiation. Since in the vast majority of cryogenic systems operate under vacuum, convection can be disregarded. Each relevant cooling mechanism introduces specific design issues for the TFC. The vacuum chamber must subtend a 1 atm pressure differential, which drives the mechanical design of the outer vacuum chamber (OVC). Cryostats are outfitted with concentric layers of radiation shields, the purpose being to limit the heat transfer through thermal radiation to the interior of the cryostat. These shields are highly reflective, typically polished aluminum, or copper, often gold plated, and thermally anchored at different temperature stages, so they may be cooled by conduction. Lastly, conductive heat loading is managed by an appropriate choice of materials. Support structures, which must necessarily be anchored to the room temperature OVC, are made with low thermally conductive materials, such as stainless steel or reinforced resin composites. Cold components and samples are connected to cooling surfaces using highly conductive materials with low heat capacities, mainly pure metallic components such as high purity aluminum or oxygen free high conductivity (OFHC) copper. Through proper management of parasitic conductive and radiative heating, low temperatures are achieved.

As funding was secured for the TFC, discussions began between the AIG and Quantum Technology Corp. (QT) in Squamish, BC on the design and construction of the TFC. The initial design of the TFC was refined following discussions with QT. The design was driven largely by the unique, cryogenic volume requirements. To fulfil its ultimate purpose, the 4 K working volume of the TFC had to exceed the proposed volume of the SAFARI instrument, which was 420 mm × 220 mm × 125 mm [34]. The TFC was designed not only to house an instrument of this size, but also accommodate input and output optics to allow testing of the system. Part of this volume was also allocated to a 300 mK adsorption refrigerator from Chase Research Cryogenics [35], to provide cooling for sensitive composite bolometer detectors which operate at this temperature [36]. The final dimensions of the cryogenic working volume were 580 mm × 480 mm × 250 mm, offering roughly 3 times the usable working volume of other cryostats available to the AIG.

Several designs for the large test facility cryostat were considered, beginning with the original design proposed for testing of the SAFARI optical delay line (Figure 3.1). The original design is discussed further in a paper presented at the SPIE Astronomical Telescopes and Instrumentation conference in Montreal, which can be found in Appendix D. The original design included a horizontal, cylindrical vacuum vessel that would provide maximal access to the 4 K work surface [37], but unfortunately, FEA simulations showed that this would be insufficiently stiff to provide the required low-vibration platform for interferometer testing (Figure 3.2).

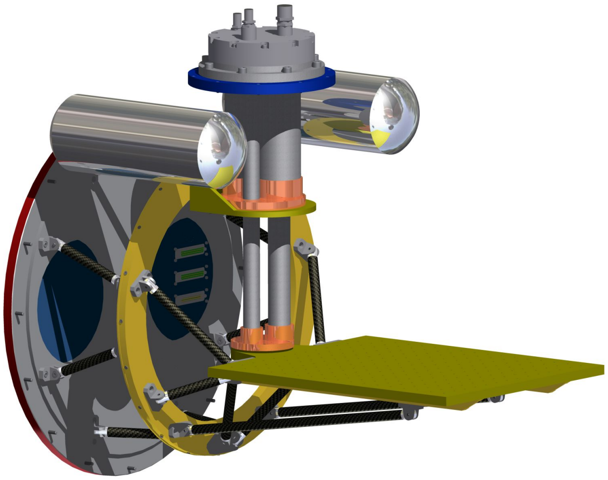

Figure 3.1: The initial design of the cryogenic test facility. This horizontal, cylindrical design featured a split OVC and radiation shields, allowing for maximal access to the 4 K working volume without disturbing the internal wiring of the cryostat [37].

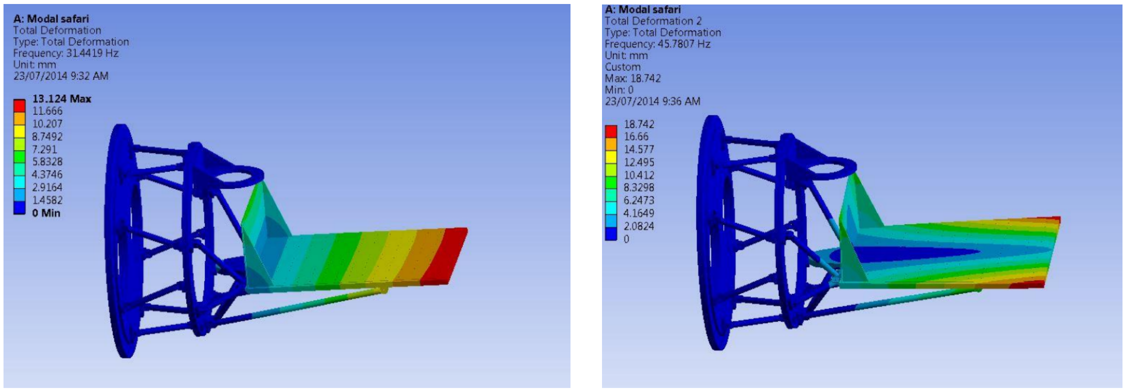

Figure 3.2: The 1st and 2nd vibrational modes for the cylindrical design of the TFC. Not surprisingly, the figures show that the 4 K plate is a cantilever, with the highest amplitude vibrations at the end of the plate. Also, the vibrational modes were low order, 31 Hz and 46 Hz for the modes pictured.

After several iterations with QT, a square, vertical design for the cryostat was selected. In this novel design, carbon fibre reinforced polymer (CFRP) plates connected to the room temperature, 45 K, and 4 K stages provide enhanced mechanical stiffness.

The rectangular design was chosen, not only for its enhanced mechanical rigidity, but also for the benefits it provided in terms of access to the usable space, allowing for multiple exterior ports. A rectangular design allowed for closer positioning of interior components to viewports, and viewport locations that were not confined to have an optical axis passing through the center of the vessel. However, the challenge of constructing a rectangular vessel lies in the mechanical strength and stiffness of the chamber. In general, cylindrical chambers are selected because of their intrinsically higher mechanical strength. Rectangular vessels rely on welded joints, which require special welding techniques in order to prevent trapped air pockets.

3.1.1 Vacuum Chamber

The vacuum vessel went through several design iterations, with stainless steel and aluminum being considered for the chamber material. Stainless steel is easier to weld but more difficult to machine, while aluminum is lighter, and easier to machine, but more difficult to weld. We chose a hybrid solution, with a stainless steel chamber because of the higher Young's modulus and yield strength offered by stainless steel, allowing for thinner OVC walls. Aluminum was chosen for the top plate because the top plate was necessarily thicker than the walls to allow room for internal threaded blind holes for mounting the internal supports. The final design incorporated 9.5 mm ($3/8''$) thick stainless steel 304 walls and a 20 mm thick Al 6061 top plate. Figure 3.3 shows the equivalent von-Mises stress (a scalar value for stress computed from the Cauchy stress tensor [38]) on the vacuum chamber as a result of a 1 atm pressure differential. The maximum stress is 90 MPa which does not exceed the 0.2% yield strength of stainless steel 304, which is around 240 MPa [39]. The maximum deformation of the chamber occurs on the underside and is about 800 μm in the center (Figure 3.4).

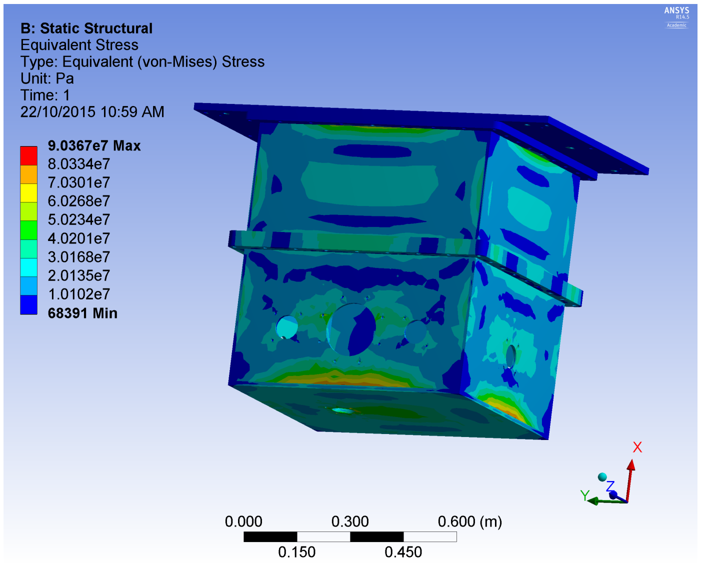

Figure 3.3: The equivalent von-Mises stress on the walls of the stainless steel 304 vacuum chamber resulting from a 1 atm pressure differential.The location of 5 viewports can be seen in this figure, and should not be confused with irregularities in the calculated stress.

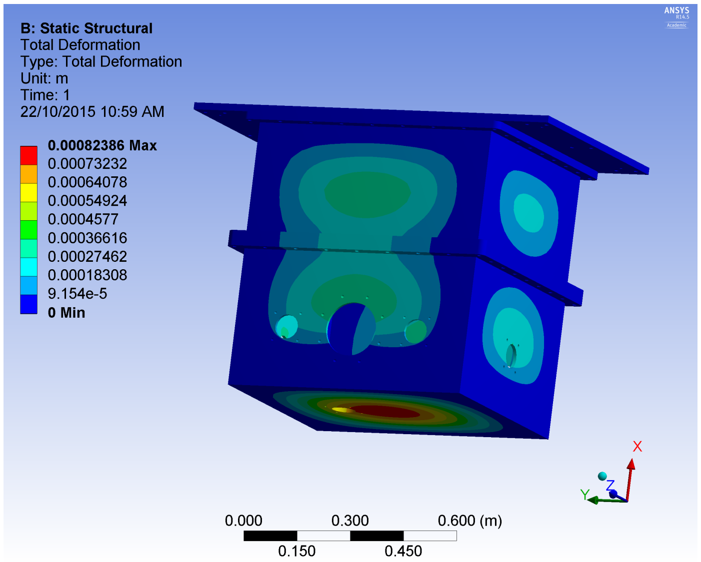

Figure 3.4: The deformation of the walls of the TFC vacuum chamber from a 1 atm pressure differential. The location of 5 viewports can be seen in this figure, and should not be confused with irregularities in the structural deformation.

3.1.2 Cooling Mechanism

TFC was designed to accommodate two identical Cryomech PT415 pulse tube coolers (PTCs) [40], but in such a way that only a single PTC would be required to reach the absolute temperature. The second unit would provide additional cooling power, and a lower cooling time. Mechanical cryocoolers were chosen because of the increasing cost of liquid helium. Only a single cryocooler was purchased due to budget limitations. Each pulse tube cooler provides a 1.5 W cooling power at 4.2 K and has an intermediate stage which provides 40 W of cooling power at 45 K [40]. The main disadvantage of using pulse tubes as cryocoolers is that they induce external vibrations. To minimize the impact of vibrations, the pulse tube cold heads were attached to the 4 K plate using flexible oxygen-free, high-conductivity (OFHC) copper braids as heat links to offer a good thermal conductive path while decoupling mechanical vibrations (Figure 3.5).

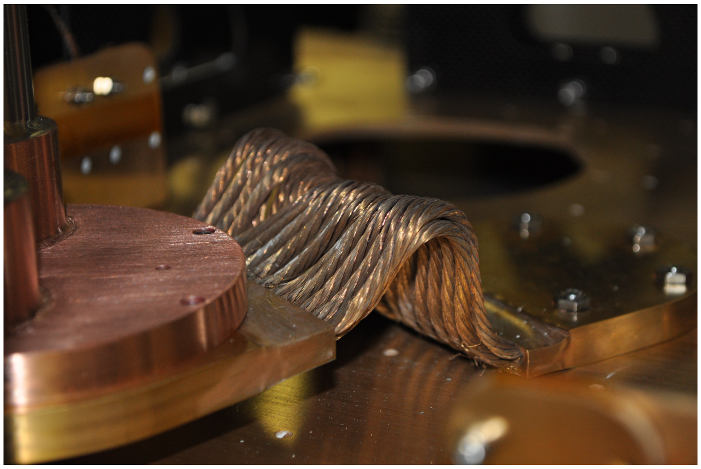

Figure 3.5: An image of the OFHC copper braid, with a 5 μm gold coating, connecting the 4 K pulse tube cold head and the 4 K plate. The flexible copper braids decouple the system from mechanical vibrations generated by the pulse tube, while conducting heat between the components.

3.1.3 Apertures

The TFC was designed to be a general purpose facility for thermal, mechanical, and optical testing at 4 K, requiring numerous input and output apertures to couple the facility with room temperature measuring equipment. Three flanges of standard sizes were placed on the front and back faces of the OVC, consisting of one ISO160 flange (160 mm inner diameter) and two ISO63 flanges (63 mm inner diameter). Two ISO63 flanges on each short face and one on the underside of the chamber were added for a total of 9 available ports (Figure 3.6). The array of apertures ensured easy access to samples or systems, in multiple configurations, on the cold plate of the TFC.

Also a crucial part of the design related to ease of access was splitting the vacuum chamber in the center as seen in Figure 3.6. With this configuration, the 4 K volume was easily accessible without having to expose the upper support structures, internal electrical wiring, and intermediate stages. To assist with the ease of access to the 4 K plate, the radiation shields were created in panelled sections so that a single panel for each shield had to be removed to access the 4 K volume (Figure 3.7). A hydraulic scissor jack was also included in the frame of the TFC, allowing for easy raising and lowering of the lower chambers.

3.1.4 Radiation Shields

The management of radiant heating through the application of radiation shields was a critical parameter in the design of the TFC. The number of shields and material selected for the shields were chosen so that they: had high thermal conductance to avoid hot spots in the shield, were highly reflective in order to minimize radiative transfer, and were thermally anchored to the PTC to allow for fast cooling of the shields. The design of radiation shields can be difficult to model because radiative heat transfer between surfaces can be difficult to predict for even the simplest of cases, and becomes almost impossible when calculating heat transfer for components that are not concentric cylinders/spheres or parallel plates. Therefore, radiative heat transfer was estimated using the parallel plate method. In this case, the amount of heating power transferred between the plates can be estimated by [24],

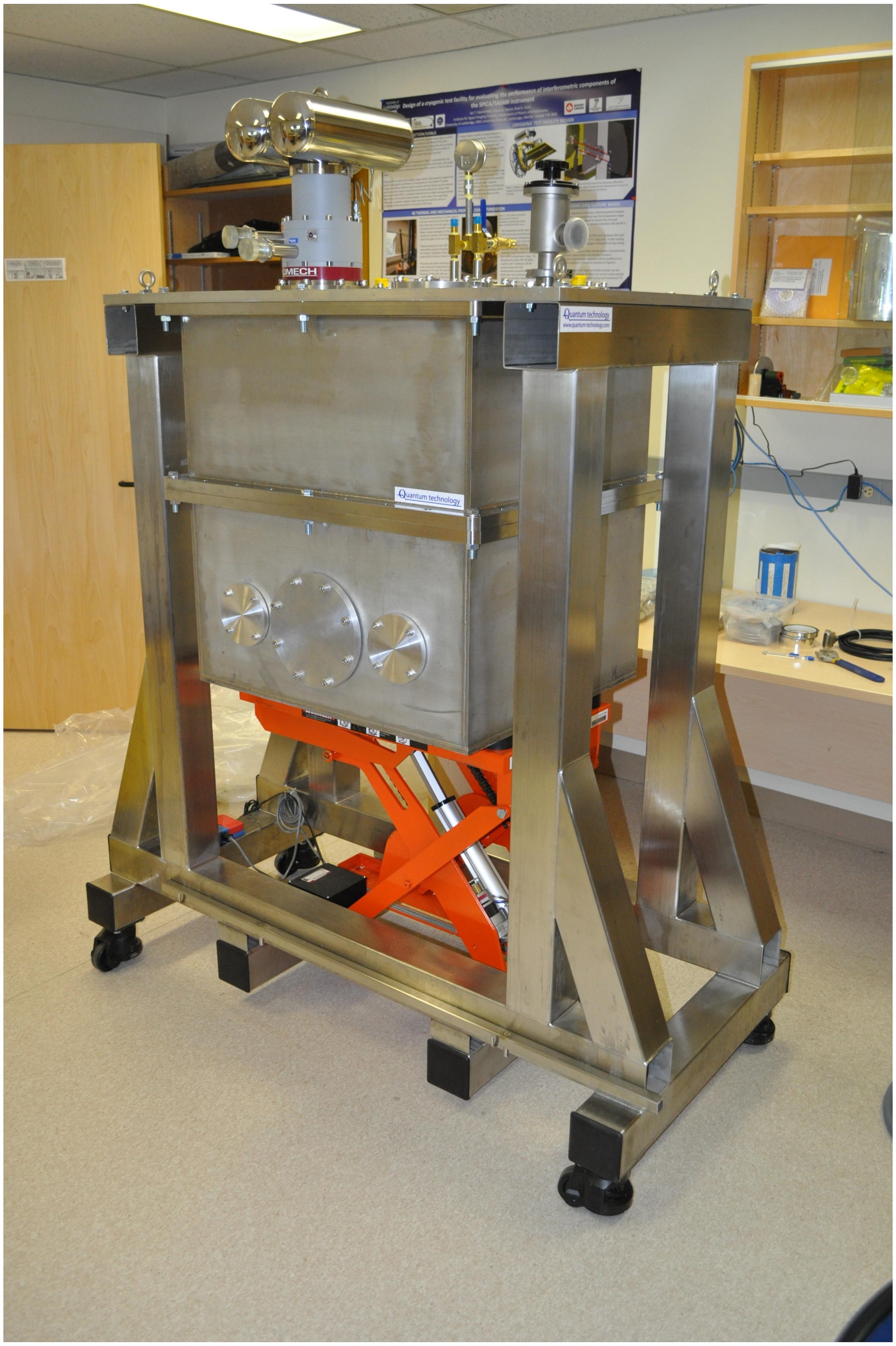

Figure 3.6: The Test Facility Cryostat after delivery to the University of Lethbridge. A single PTC, vacuum port, and liquid nitrogen inlet/outlet can be seen mounted to the upper plate. The horizontal split in the vacuum chamber allows for the bottom half of the chamber to be lowered by the scissor jack. Three blank flanges for the side apertures are also shown.

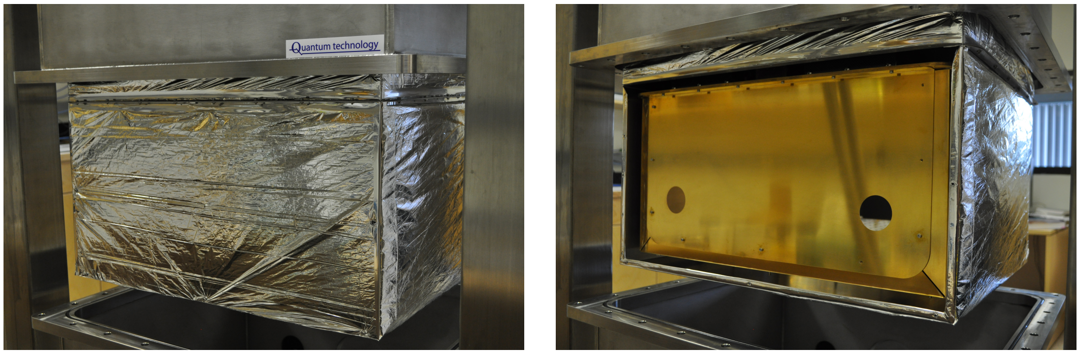

Figure 3.7: Removable radiation shield panels for accessing the 4 K volume.

$$\dot{q}_{rad} = AE\sigma(T_2^4 - T_1^4) \qquad \text{(W)} \tag{3.1}$$

where A is the area of the smaller plate, E is a factor that depends on the emissivity of both surfaces, ε_1 and ε_2, T_1 and T_2 are the temperatures of the inner and outer surface respectively and σ is the Stefan-Boltzmann constant. E can be expressed by the equation [24],

$$E = \frac{\varepsilon_1 \varepsilon_2}{\varepsilon_1 + \varepsilon_2 - \varepsilon_1 \varepsilon_2}. \tag{3.2}$$

There were two layers of radiation shielding which minimized the radiant loading on the 4 K working volume. An aluminum shield was designed to be thermally sunk to the 45 K plate as an intermediate shield. The aluminum shield was surrounded with layers of aluminized mylar sheets, commonly referred to as multi-layer insulation (MLI). The purpose of the MLI was to decrease the radiant loading onto the aluminum shields themselves so as not to overload the 40 W cooling capacity of the 45 K cold head. Theoretical models predict that with N identical, low-emissivity shields, the radiative heat transfer is decreased by a factor of $1/(N+1)$ [24, 41]. However in reality, the actual insulating advantage per layer is much lower since the application of MLI is never an exact method and is subject to such factors as the amount of contact between the shields and how densely packed the layers are. Therefore, the number of layers required was determined empirically and minimized for ease of installation. The MLI application is discussed further in Section 3.2.2. A second layer of shielding was added at the 4 K level. These shields were constructed from OFHC copper and gold plated to a thickness of 1 μm. The gold plating conferred two advantages. The first was on the connecting flange, Au-Au contacts are shown to have the smallest thermal resistance which means the shields will get colder with gold coating than with any other material [42]. The second reason was gold, polished to a specular finish, has one of the lowest emissivities of all materials in the infrared [24]. This means that heat transport from the outer layer of shielding to the inner level was minimized.

3.1.5 Precooling System

The goal for the cool down time of the TFC was that the facility cooled down to 4 K with no assistance within 24 hours, operated by a single PTC. To provide a faster cool down time however, a liquid nitrogen (LN2) precooling system was incorporated. The LN2 system includes stainless steel flexible bellows from the upper room temperature plate to two reservoirs on the 45 K and 4 K stages in series (Figure 3.8). The reservoirs on the plates were fabricated from OFHC copper with a stack of OFHC copper leaves inside each reservoir in order to increase surface area and therefore increase heat transfer from the LN2. The reservoirs are bolted to the 45 K and 4 K plates with a thin layer of apiezon N grease [43].

3.2 Assembling the TFC

I travelled to Quantum Technology Corporation's facilities in Vancouver to assist with the assembly of the TFC, and to gain practical experience in the industrial setting. My contributions to the assembly of the TFC are in two specific areas: the gold plating of the TFC components, and the electrical wiring to the 4 K working volume.

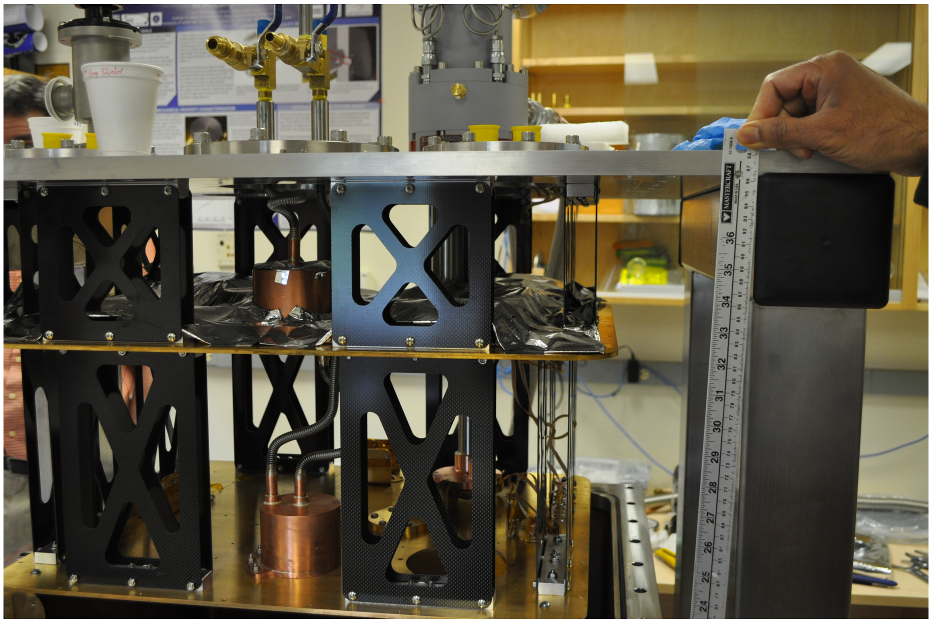

Figure 3.8: The upper sections of the TFC showing the CFRP support plates as well as the precooling system.

3.2.1 Gold Plating

As mentioned in the previous section, gold coating of low temperature components increases the thermal conductance across joints, and also decreases the emissivity of the components. All components at 4 K were coated in gold to ensure maximum efficiency of the thermal connections. Moreover, gold coating was applied in order to minimize the effects of corrosion. The 4 K shield panels, 4 K plate, 45 K plate, wiring heat sinks, electrical connector plates, and flexible copper braids were all gold plated. We adopted an electroplating method for the gold coating process. The component to be plated was suspended in a 24 K pure gold solution from Gold Plating Services [44]. The anode consisted of 2 platinum clad niobium sheets (6” x 34”). The optimum plating current density for the plating solution is typically 2 to 5 mA cm^{-2} [45]. Therefore, a 3 mA cm^{-2} current density was selected and the current was supplied by two 6 A Agilent power supplies configured in parallel. The required plating time was estimated as [46],

$$T = \frac{\rho_{\text{Au}} t n F}{J m(\text{Au})}, \qquad \text{(s)} \qquad (3.3)$$

where T is the total plating time, ρ_{Au} is the density of gold, t is the plating thickness, n is the ionic charge of the gold ion in the plating solution ($+1$ in this case), F is Faraday's constant, J is the current density, and $m(\mathrm{Au})$ is the atomic mass of gold. The above equation assumes 100% plating efficiency. Two gallons of gold plating solution were used, costing approximately US$1200 each.

Gold coatings for contact surfaces (ie. the 45 K and 4 K plates) were plated to at least 2 μm thick to provide a sufficient contact area for the thermal conductance. Surfaces that were gold plated in order to decrease emissivity (ie. 4 K shields) were coated to a thickness of 1 μm, many times thicker than the skin depth of gold at infrared wavelengths, which ranges from 3.8 to 120 nm from 1 to 1000 μm.

3.2.2 MLI installation

Fabricating the 45 K shields in panels was inconvenient for the application of MLI. Additionally, efficiency of the MLI was decreased, owing to the increased contact between layers at the panel edges. However, the benefits associated with ease of access to the 4 K volume outweighed the inconvenience. Although MLI can be purchased in bulk with a specified number of layers, we decided to construct our own from a roll of aluminized Mylar. Mylar sheets were cut to size for the shield panels at the University of Lethbridge and were then taken to QT during assembly of the TFC.

For the first application of MLI, four layers of $\sim$20 μm thick MLI, aluminized on both sides, were applied to each shield panel, not including the top of the 45 K plate, and held in place with aluminized mylar tape. Small, $<$1 mm holes were melted into the MLI panels, with a fine-tipped soldering iron, in a 150 mm $\times$ 150 mm grid to allow for outgassing between layers. Bolt holes in the panels were also melted out of the MLI with a broader tipped soldering pencil. After the first cool down, more layers of MLI were added to reduce the radiant loading seen by the 45 K shield. Twelve layers of MLI in total were added to the upper 45 K shields, and fixed lower panels, which are seldom removed. Eight layers were added to the upper half of the 45 K plate, and on the lower removable panels which are removed to access the 4 K volume. The shield base temperatures are reported in Section 3.3.1. Due to time constraints and since the performance of the TFC was deemed adequate, the number of layers of MLI was considered sufficient. More layers can be added in the future to further improve the performance. However, diminishing returns will be seen as the density of MLI increases, owing to the increased surface contact between layers [47].

3.2.3 Cryostat Wiring

The goal of the TFC is to test cryogenic instruments, which commonly have mechanisms which require electrical connections for motion, metrology, and thermometry. Since electrical wiring provides a conduction path from room temperature to the cryogenic components, wire material and diameter was selected in order to minimize the heat flow while also meeting the appropriate current requirements. Cryostat wiring is selected by minimizing the summation of the heat load due to conduction as well as the heat load due to Joule heating. Thermal conduction is calculated using Fourier's Law, shown in Equation 2.21, while Joule heating is predicted using the relation $P = I^2R$ where I is the current flowing through the wire, and R is the wire resistance. The design of the TFC included wiring for two main applications: low current thermometry wiring, and high current power wiring. To date, I have installed 70 wires in the TFC. The thermometry wiring consists of 60 39 AWG wires, allowing for fifteen thermometers in 4-wire configurations. Six 39 AWG wires for small, low current heaters were also added, as well as four 32 AWG high current leads. Since the current requirements for the thermometry wiring were low ($<10\,\mu$A), the wiring was purchased in the form of dual-twist looms with 12 pairs of 39 AWG OFHC copper conductors each [48]. While using a material with a higher resistivity would have decreased the heat conduction along the wire, OFHC copper wire was selected in order to allow for slightly higher current applications (10 to 100 mA), such as for small heaters, without introducing excessive Joule heating or melting the wire insulation.

Four 23-pin Amphenol electrical connectors were located on the top mounting flange, shown in Figure 3.9. The OFHC copper looms were used with two of the connectors, with a 1 m loom length from room temperature to 60 K, and 1 m from 60 K to 4 K. Each loom allowed for 5 thermometers (ie. 20 wires in a standard 4-wire configuration [49]) and 1 small heater circuit (2 wires). Five thermometers were wired permanently into the upper structures of the TFC, on each of the pulse tube cold heads, each of the LN2 reservoirs, and on the 45 K plate. Since these thermometers were placed at different levels, one continuous loom to the 4 K plate could not be used. Therefore, quad-twist phosphor bronze wire was used for each thermometer so that they could be placed in any location inside the TFC [50]. A full block diagram of the TFC thermometry wiring can be found in Appendix B.

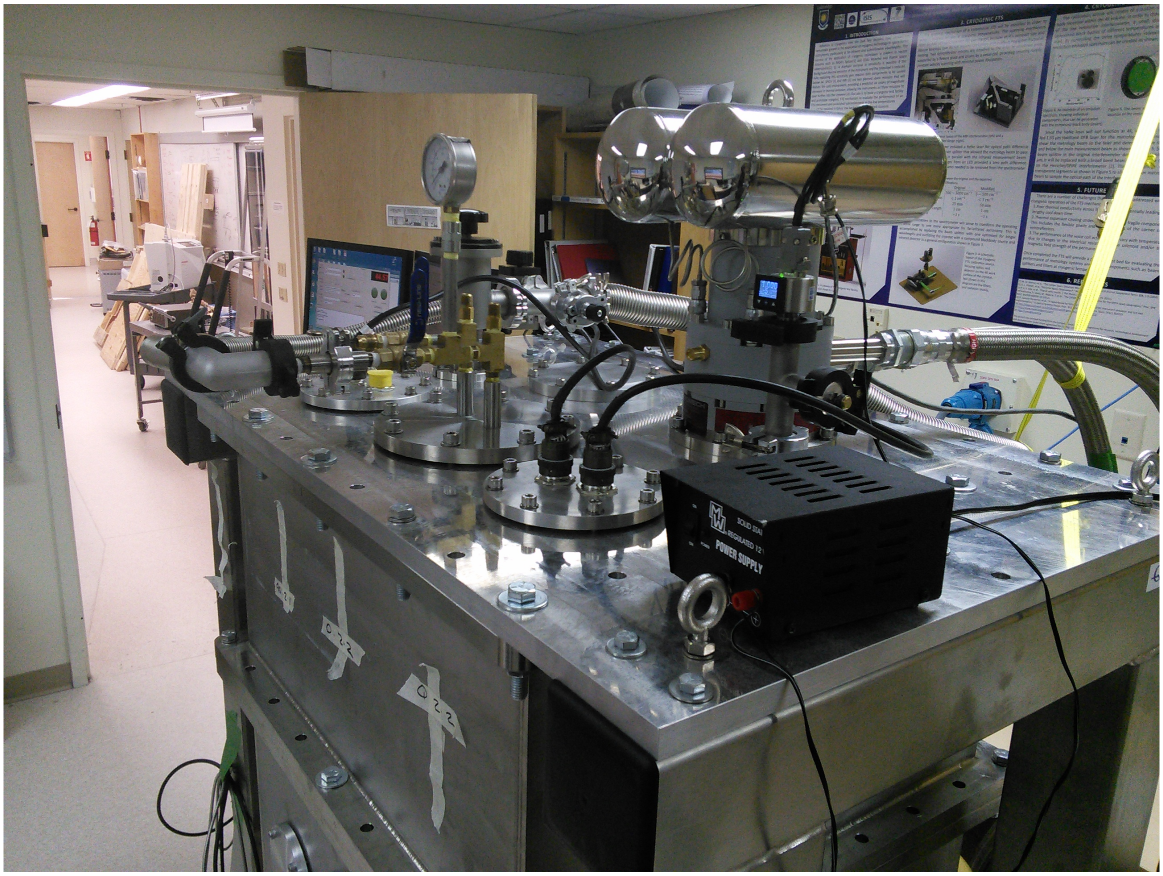

Figure 3.9: The top plate of the TFC, showing the Amphenol electrical connectors, vacuum flanges and bellows, pop-off valve to relieve overpressure, and pressure gauge with power supply.

For the initial testing, the five permanent thermometers were available. To provide a broader overview of the system temperature range for the initial cooling verification tests, the LN2 reservoir thermometers were removed and placed on the 4 K plate and warm end of the 45 K aluminum shields.

3.3 TFC Verification

Once the TFC had been assembled, two cool downs cycles were performed at QT's facilities as part of acceptance tests before the system was delivered. The key specification was the lower temperature limit of the facility with a single pulse tube. Also of importance was the cooling times, and the base temperature of the 45 K shields. The cooling power of the TFC was measured in subsequent weeks following the delivery of the TFC. The results of the TFC acceptance tests are presented in the following section.

3.3.1 Base Temperatures

During the first cool down of the TFC, four layers of MLI were installed, and as a result the system failed to reach the target temperatures. Figure 3.10 shows the cool down curves resulting from the first cool down. It was determined that the 45 K shield was still too hot, overloading the 4 K volume with parasitic radiant heating. Therefore, the system was opened up again and more MLI was added.

As discussed in Section 3.2.2, more layers of MLI were added to the 45 K shield panels in the second cool down. Additionally, two strips of 8 layer MLI were wrapped around the upper and lower seams in the 45 K shields. The 45 K shields reached sub-100 K and the 4 K plate reached 3.8 K so this level of MLI was deemed sufficient (Figure 3.11). Further layers of MLI will be applied in the future to further improve the cooling time, and the base temperatures of the shields.

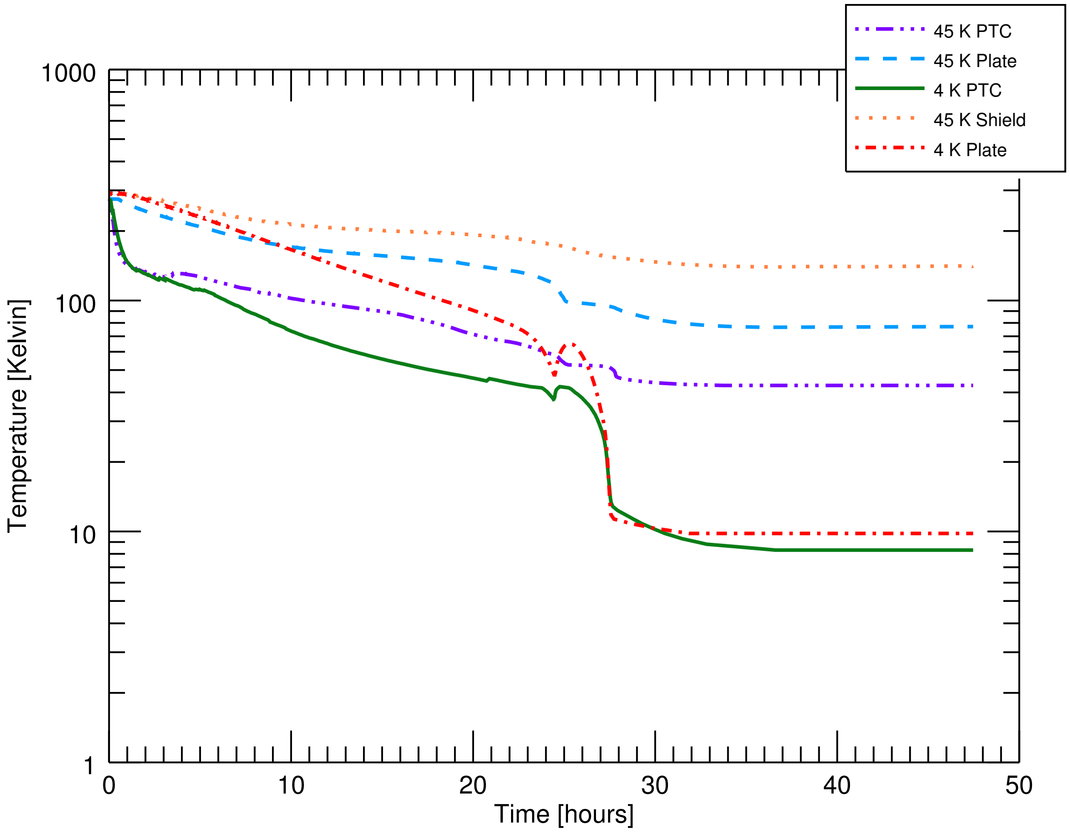

Figure 3.10: Plot of the temperatures for the first cool down of the TFC. The system did not reach the desired base temperature of 4 K, and took nearly 40 hours to reach thermal equilibrium. The sharp drop in the temperature of the base plate at 27 hours is due to the liquefaction of helium in the 4 K pulse tube cold finger. All temperature readings have an approximately 2% uncertainty.

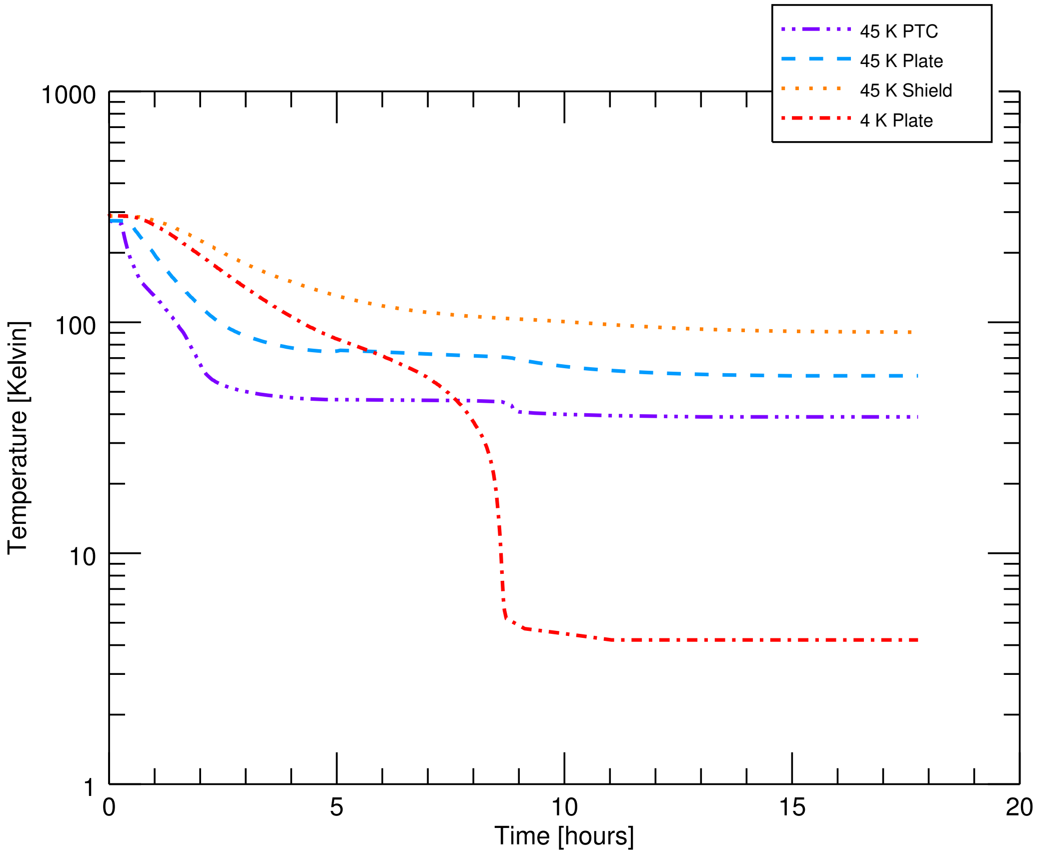

Figure 3.11: Plot of the temperatures for the second cool down of the TFC. Note in this cool down, liquid nitrogen was used in the first 5 hours to supplement the cooling power of the pulse tube. Also, the 4 K PTC thermometer is not shown because the thermometer lost contact with the cold head. All temperature readings have an approximately 2% uncertainty.

3.3.2 Copper Braid

A study of the thermal gradient across the copper braids provided insight into the heating of the cryostat due to thermal radiation and conduction along the CFRP supports. The copper braid in Figure 3.5 consisted of 26 braids, each with a 3 mm diameter, and connects the 45 K PTC cold head to the 45 K stage. A 20 K thermal gradient was present across the braids, shown in Figure 3.11, corresponding to a 17 W heat flow through the braid from the integral form of Fourier's Law (Equation 2.21), assuming negligible thermal contact resistance for the bolted connections on either end of the braid. Since the system was in thermal equilibrium at this time, the equivalent cooling power of the 45 K cold plate was 17 W rather than the quoted 40 W. An increase in the heat flow through the braid, by adding more copper strands for example, would increase the cooling power of the system.

3.3.3 Cooling Power

Though the PTC has a quoted 1.5 W cooling power at 4.2 K [40], much of this cooling power was utilized for mitigating the effects of parasitic heat loading, such as radiation from higher temperatures and conduction through the internal wiring. Therefore, the residual cooling power was measured directly, as well as calculated through thermal modelling. To measure the residual cooling power, a large 5 W heater was placed on the edge of the 4 K plate. Two thermometers were placed on the plate in different locations. One thermometer sat near the heater and the other sat on the opposite edge of the plate. The heater was wired to a PID control system internal to the Lakeshore 340 temperature controller [51]. As the temperature was adjusted to different setpoints, the current through the heater was adjusted and the voltage drop across the heater was measured using a 4-wire method. The heater power ($P = VI$), was taken to be the available cooling power at the temperature corresponding to the thermometer on the far side of the plate.

From the data in Table 3.1, we can conclude that of the total available 1.5 W cooling power at 4.2 K, 1.25 W was used to mitigate the parasitic heating effects of radiation from

Table 3.1: Cooling power results for the TFC.

Current [mA]	Voltage [V]	Cold Plate Temperature [K]	Heater Temperature [K]	Heater Power [W]
16.8	9.606	4.004	4.19	0.161
19.4	12.82	4.249	4.44	0.249
21.3	15.34	4.500	4.68	0.327
23.0	17.88	4.750	4.93	0.411
24.3	20.02	5.002	5.19	0.487
26.7	24.03	5.499	5.68	0.642
28.7	28.15	6.005	6.19	0.808
32.4	34.91	7.001	7.19	1.131
35.6	41.62	8.000	8.20	1.482
38.4	48.24	9.001	9.21	1.852
40.5	53.22	10.00	10.2	2.155

the shields and heat transport through the wires.

3.3.4 Shield Temperatures

Thermometers were placed over various parts of the shields to produce a thermal map of the shields during the cooling process. One of the reasons for this measurement was to verify that the temperature disparity that originated from having a split in the middle of the shield was not too great. A bolted connection in a cryogenic system is bound to introduce some degree of thermal resistance into the conduction path. This contact resistance can be due to: pressure of the joint, deformations in the contact surface, surface roughness, and particles trapped between the joint. Because of this, contact resistance can be difficult to predict and must therefore be measured directly. Furthermore, degradation of the contact surface is avoided by keeping the surface clean. Thermal contact resistance is often defined as,

$$\rho_c = \frac{1}{\alpha_c} = \frac{\dot{q}}{\Delta T} \qquad \text{(W/K)} \qquad (3.4)$$

Where ρ_c and α_c are thermal contact resistance and conductance. $\dot{q}$ is the heat flux and ΔT is the temperature difference across the joint.

The thermal map in Figure 3.12 shows that even though the base temperature of the 4 K plate is achieved after 23 hours, the 45 K shields still continue to cool for another ~10 hours.

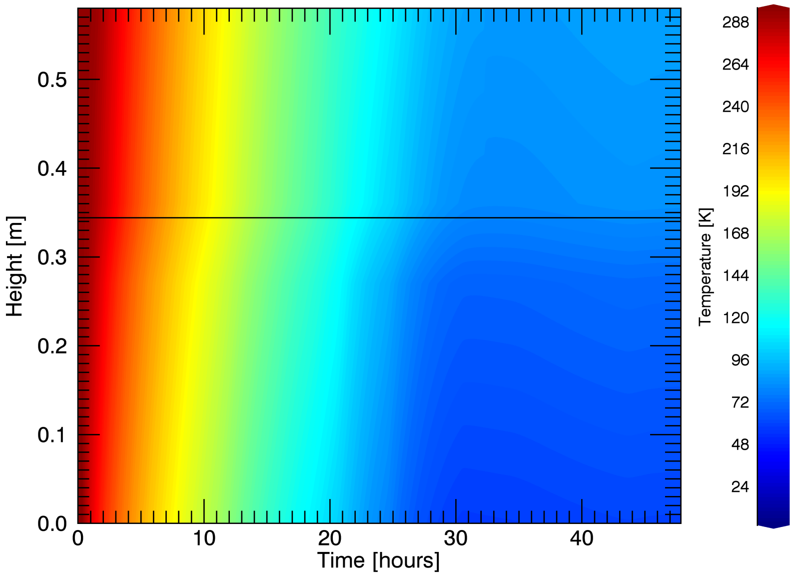

Figure 3.12: Temperatures of the 45 K shield during a typical cool down. The horizontal line at 0.35 m is the location of the split in the 45 K shield.

3.4 External Instrumentation

Despite the impressive capacity of the TFC to cool large masses and volumes to 4 K, the inclusion of only thermometer and small heater wiring on construction limits the capabilities of the system to a degree. The TFC was designed to be a multi-purpose facility for testing the cryogenic performance of new spectroscopic instrumentation for space telescopes as well as for measuring material properties of composite materials at low temperatures. High precision instrumentation and metrology systems are therefore required to perform these measurements. For this reason, two externally mounted metrology systems were incorporated into the system design.

3.4.1 Cryogenic Iris

Much of the external instrumentation requires a window in the TFC. Under the current circumstances, a single pulse tube is not sufficient to cool the system with a window open to the laboratory environment. The total radiant power through a window (40 mm diameter in this case), calculated by the Stefan-Boltzmann Law amounts to:

$$P_{rad} = A\sigma T^4 \approx 0.5\,\mathrm{W} \tag{3.5}$$

Where A is the diameter of the window, T is 293 K, and σ is the Stefan-Boltzmann constant. From Table 3.1, this heat input is double the residual cooling power of the TFC at 4.2 K, increasing the base temperature of the TFC to 5 K. Therefore, a cryogenic, motorized, zero-aperture iris, consisting of twin sets of blades, has been designed. When closed, the iris prevents a direct line of sight to the laboratory, so that the system may reach base temperatures with the iris closed (Figure 3.13).

3.4.2 Renishaw Differential Interferometer

When measuring performance of an instrument or material properties, accurate position measuring is generally required. The system which AIG have acquired for the task is an RLU10 laser unit and RLD10 differential interferometer from Renishaw [52]. This system uses a stabilized HeNe laser, a double-pass interferometer, and quadrature detection to measure the relative displacement between two parallel flat mirrors. A relative measurement technique was chosen because this makes the measurement insensitive to common-mode vibrations of the TFC along the measurement axis. This system has a resolution of 38.6 pm and has been used to measure thermal expansion of composite materials, as discussed in Chapter 4. In the future, this system will be useful for high-resolution metrology.

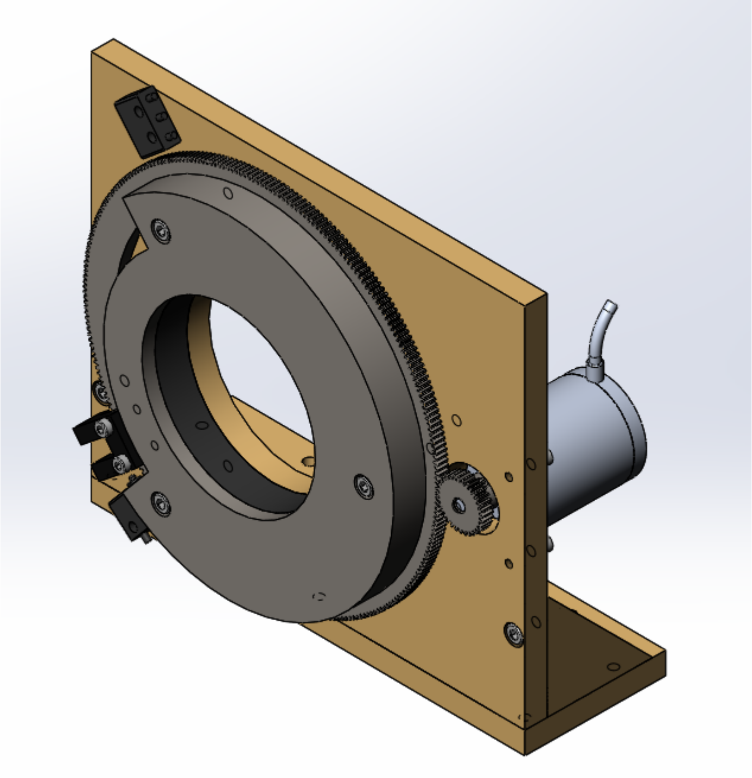

Figure 3.13: A cryogenic iris for the TFC to block room temperature thermal radiation from reaching the 4 K environment during cooling. The iris is powered by a cryogenic, high vacuum compatible stepper motor, and a gear train with a mechanical advantage of 8. Once base temperatures are reached, the iris will be opened to allow for optical measurements.

3.4.3 Electronic Autocollimator

The electronic autocollimator (PLX ACT-25) allows the AIG to measure the tilt of optical components [53], as opposed to displacement which is measured by the differential interferometer. The autocollimator has an 84 x 84 arcminute field of view with an accuracy of 2.5 arcseconds, allowing for measurement of the tilt of a plane mirror up to 42 arcminutes. The autocollimator has been mounted onto one of the large viewport flanges on the TFC and has been used to measure the twisting of the 4 K plate during cooling. Also, this system has proved useful in measuring the accuracy of corner cube retroreflectors and rooftop mirrors and their performance and deformations during cooling from room temperature to 4 K. In the future, this system will also be used to measure flexure modulus of materials at cryogenic temperatures.

Figure 3.14: An image of the Renishaw RLD10 differential interferometer, mounted to the TFC with a custom-made set of aluminum plates. The plates allow for slight positional corrections to be made outside the cryostat, as well as easy detachment and re-attachment of the interferometer without realignment.

3.4.4 Mechanical Feedthroughs

Mechanical feedthroughs have not been incorporated at this point due to the addition of parasitic conduction heat loads associated with them. In the future, these may be added to the TFC to enable application of external loads in order to measure mechanical properties at low temperatures.

3.5 Conclusion

The TFC has been designed, fabricated and delivered to the AIG laboratories. Operating conditions have been tested and the TFC is operating as expected. The operating specifications are listed in Table 3.2. In the coming months, the performance of the TFC is expected to improve as additional sheets of MLI are added and the copper braid is redesigned. External instrumentation has been successfully integrated with the TFC and used to measure properties of composite materials, as discussed in the following chapter.

Figure 3.15: An image of the PLX electronic autocollimator mounted on one of the large viewports in the TFC. A shelf was constructed to hang from the viewport so that the autocollimator could be mechanically coupled to the TFC to reduced vibrational errors in the measurements. The viewport flange, shelf, and autocollimator can be removed from the TFC as a single unit.

Table 3.2: Performance specifications of the TFC.

Parameter	Predicted	Actual
Size	1.5 m × 0.75 m × 2 m	1.5 m × 0.75 m × 2 m
4 K Volume	580 mm × 480 mm × 250 mm	580 mm × 480 mm × 250 mm
MLI	30 layers	12 layers
Pump Out Time	<8 hours	3.5 hours
Cool Down Time	<24 hours	23 hours
Warm Up Time	24 hours	40 hours
Cooling Capacity	1.5 W with 2 PTCs	250 mW with 1 PTC
Thermometry Channels	up to 16	15
Viewports	2 x 150 mm dia., 7 x 50 mm	2 x 150 mm dia., 7 x 50 mm dia.

Chapter 4

Composites for Cryogenic Instrumentation

The development of composite materials is an emerging field, driven primarily by the need for materials with specific mechanical and thermal properties for aerospace applications, but also has applications in other fields, one of which is astrophysics. The process of developing composite materials involves combining multiple materials to exploit their favourable properties. Typical composites are composed of two materials: a matrix material and a reinforcement material. While there are many common materials which could be considered composite materials, including concrete and plywood, the emphasis of this chapter is on strong, lightweight, fibre-epoxy composites. The reinforcement material consists of thin fibres that are responsible for the bulk of the material's strength. Common fibre materials include glass, Kevlar® [54], and graphite. The matrix material is generally a cured polymeric resin. The matrix plays the role of protecting the fibres from adverse environmental conditions, and also propagating mechanical loads between fibres and across the composite. With the matrix, the material can be constructed on a larger scale, and at a lower density, than the reinforcement material alone would allow. Additionally, the matrix increases the fracture toughness of the composite, allowing for a number of individual reinforcement fibres to fracture under stress without compromising the whole material. This chapter discusses the benefits of fibre-epoxy composites, which use carbon fibres in a resin matrix, for cryogenic, space-based instrumentation.

4.1 Carbon Fibre Reinforced Polymers

As the name suggests, carbon fibre reinforced polymers (CFRPs) are a class of composite material consisting of two components: a polymer resin matrix and carbon fibre reinforcements. CFRPs are of great interest in today's field of composite materials because they exhibit favourable properties, such as high stiffness, high tensile strength, low weight, high chemical resistance, high temperature tolerance, and low thermal expansion. The properties of CFRP make it useful especially for mechanical supports under tensile loads. Their high strength-to-mass ratio and heat resistance have made them the material of choice for high-performance applications such as aircraft wings, satellite supports, and luxury vehicles. Figure 4.1 shows two CFRP samples that were used for testing of their cryogenic properties.

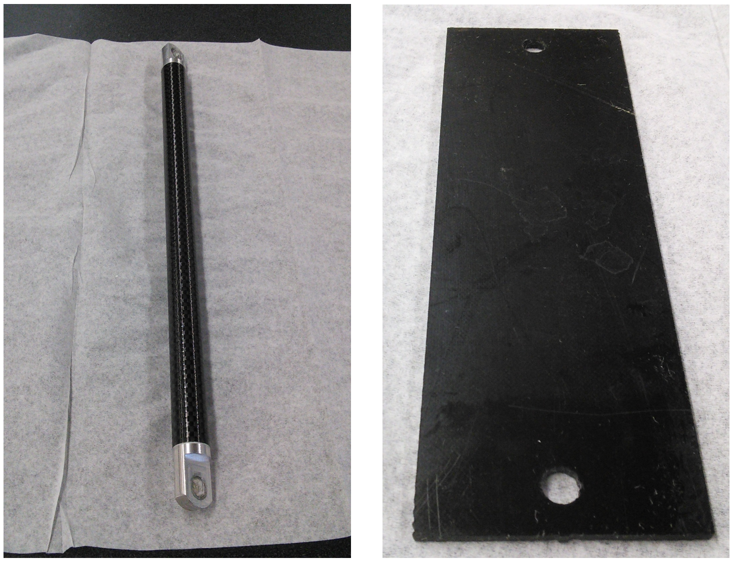

Figure 4.1: Samples of CFRP plates and rods which were used for the measurement of their thermal properties. The rod was a high-strength lightweight carbon fibre tube purchased from McMaster-Carr (Part # 5287T32) [55], and the plate was fabricated by Martyn Jones of Glyndwr University, Wales.

The matrix material is typically an epoxy resin, consisting of organic polymers. The types of epoxies used can be classified into two categories: thermoplastics and thermosets. A thermoplastic material is a polymeric material which solidifies when cooled and can return to an uncured state when reheated. These materials can be remolded at elevated temperatures and recured multiple times. However, this form of resin exhibits a significant amount of creep (defined in Section 2.5.4), even when well below the melting point of the resin. On the other hand, thermosets are polymeric materials which have been cured at an elevated temperature, and cannot be melted or reshaped post-cure. Thermosets are typically used when constructing rigid components from CFRP because they are generally stronger, yet more brittle. Thermoplastics are used when ductility is an important factor for the produced component. Most matrix materials such as epoxies, polyesters, and polyimides fall into the thermoset category [56].

The carbon fibres are typically thin, approximately 5 μm diameter [56], and are commonly used because of their high stiffness. As compared to other reinforcing fibres, carbon fibres exhibit the highest elastic modulus (Section 2.5.2). Also, cryogenic tests have indicated that carbon fibres exhibit a smaller temperature dependence of the Young's moduli as compared with other common reinforcement materials, such as alumina or glass fibres [57]. A commercially available carbon fibre will have tensile modulus between 207 to 1035 GPa [56], which serves to illustrate the range of possible properties available when fabricating CFRP. Hartwig and Knaak report a matrix laced with carbon fibres showing a Young's modulus approximately 4 to 6 times greater glass fibre reinforced composites (GFRP) with the same volume fraction of fibres, and 1.5 to 2.5 times greater than a Kevlar® fibre composite [58]. The variability of the Young's modulus for different carbon fibres is based on the molecular structure of the carbon fibres, resulting from the fabrication process. Carbon fibres can be manufactured from two precursors, namely, polyacrylonitrile (PAN) or pitch [56]. Typically, PAN carbon fibres are wet spun from a PAN solution at elevated temperatures (100 to 200 °C) to align the polymer chains in the fibre direction, and then carbonized at high temperatures (1000 to 2000 °C). Subsequent heat treatment (above 2000 °C) causes the carbon structures to become more ordered and graphitic. Strength of the fibres can be improved by stretching during the graphitization. Pitch fibres are produced from heat treatment (300 to 500 °C) of isotropic pitch, until the pitch polymerizes to form molecular sheets. This state of the pitch is known as ”mesophase.” Fibres are produced by melt spinning mesophase pitch through a spinneret. The fibres are then stabilized (at 200 to 300 °C) to avoid fusing them together. Subsequent heat treatment to carbonize and graphitize the fibres are similar to the PAN fibre production [56]. Carbon fibres produced from pitch are more brittle, having a lower tensile strength and tensile strain-to-failure, but they have a higher tensile modulus than PAN carbon fibres. This is a characteristic of the higher percentage of graphitic carbon in pitch fibres. The tensile strength of both PAN and pitch fibres is highly dependent on the defects and flaws in graphitic carbon form [56]. Generally, PAN produced fibres are classified as turbostratic and pitch produced fibres are graphitic. Turbostratic (PAN) fibres also have a higher fracture toughness because carbon atoms are folded rather than flattened, limiting the propagation of cracks [59].

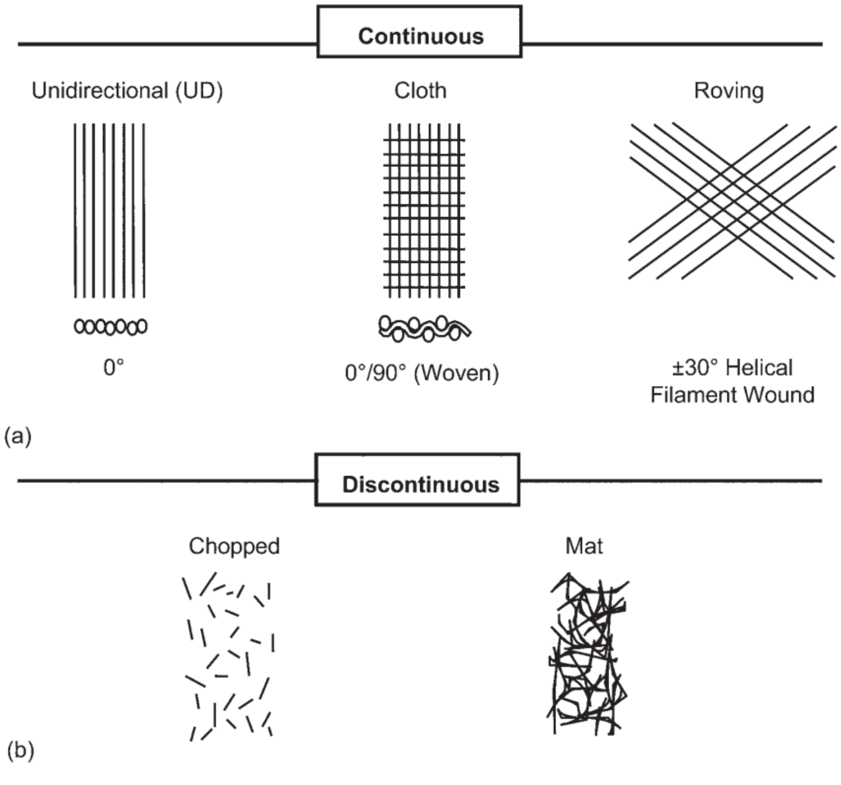

Figure 4.2: Typical fibre reinforcement types and configurations. [60]

Carbon fibre composites may be constructed with either continuous (long) or discontinuous (short) fibres, shown in Figure 4.2. The classification of the fibres is determined by the fibre length in relation to a critical fibre length. The critical fibre length is quantitatively defined as,

$$l_c = \frac{\sigma_f d}{2\tau_m}, \qquad \text{(m)} \quad (4.1)$$

where σ_f is the ultimate tensile strength, d is the fibre diameter, and τ_m is the shear strength of the fibre-matrix interface. A composite with fibre lengths shorter than the critical length will not efficiently transfer mechanical loads from the matrix to the fibre. That is to say, the shear strength of the fibre-matrix interface is less than the tensile strength of the fibre, causing the fibre-matrix boundary to detach before the fibre fractures [61–64]. Therefore, short fibre composites have a lower strength and elastic moduli as compared to long fibres. However, when incorporated into a thin layer of matrix material, often referred to as a ply or lamina, short fibres may be oriented in random directions to obtain equal thermal and mechanical properties in all directions parallel to the plane of the ply. The uniform properties along the plane means this material is referred to as quasi-isotropic. Plys of continuous fibre composites may have their fibres oriented in a single direction (unidirectional) or in two directions as a weave or other fabric form (bidirectional) as shown in Figure 4.2. A unidirectional ply will have high strength and modulus along the direction of the fibres but weak mechanical properties in the transverse directions. Continuous fibre composites are more costly to manufacture, but utilize the full potential of the reinforcement strands.

Long strand carbon fibres may be purchased as dry bundles which must be coated with resin to form a lamina. More commonly, the continuous fibres are purchased pre-impregnated into a thin sheet of resin, known as *prepreg*. The thickness of *prepreg* sheets usually varies between 0.13 to 0.25 mm [56]. Layers of *prepreg* are then cut to size and the laminae are stacked until the desired thickness is reached, forming a composite laminate. Layers may be stacked in any orientation desired depending on the directional strength required. If high strength is needed in only a single direction, the laminae are stacked parallel, forming a unidirectional, anisotropic material (Figure 4.3a). If strength and stiffness are required in multiple directions, these layers can be stacked in alternating orthogonal layers, making a quasi-isotropic material (Figure 4.3b). In both cases, the material will have weak properties along the normal direction to the laminate layers, due to the weak bonds between the laminae and the lack of reinforcement fibres in this direction.

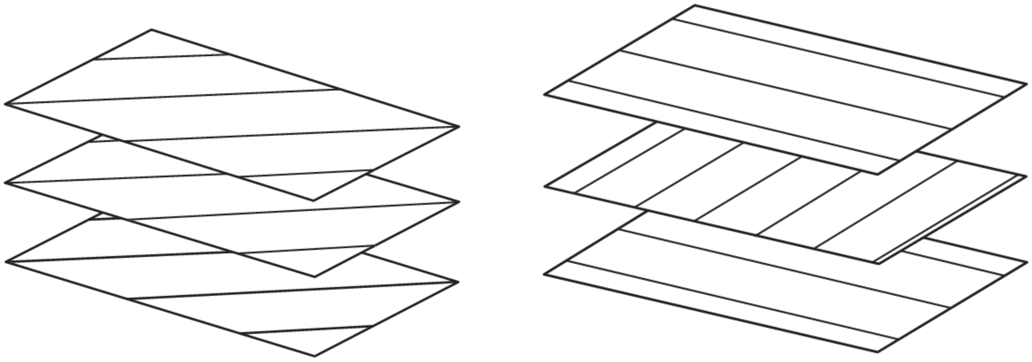

Figure 4.3: (Left) Unidirectional stacking of unidirectional, continuous fibre laminae, forming a unidirectional laminate. (Right) Orthogonal layers of unidirectional, continuous fibre laminae, forming a quasi-isotropic laminate [56].

4.2 Space Applications

CFRPs have long been used in space applications because of their well suited properties for extreme applications. The main use of composite materials is for construction of components with high strength-to-mass ratio.These are commonly the support structures for space vehicles and instrumentation. Using composite materials offers the benefits of reduced mass, and lower moment of inertia, both of which decrease fuel requirements. CFRPs are the material of choice because their strength-to-mass and tensile modulus-to-mass ratios are among the highest for any material. The ability to orient the fibres unidirectionally allows the composite to have high stiffness along a single axis, making continuous fibre CFRP composites useful for support straps and struts. CFRP supports are used for a variety of components such as solar arrays, antennas, and optical platforms [65].

In addition to strength of materials, another important driver when designing cryogenic systems is the thermal properties of the material. CFRP is often chosen instead of other strong fibre composites because it can be designed to have a very small coefficient of thermal expansion (CTE). CTEs can be manufactured to be comparable to that of Invar, with an additional advantage being due to the lower density and higher strength of CFRP. CFRPs are therefore used as supports for objects which must be dimensionally stable over a large temperature range. These objects include telescope mirrors and lenses as well as optical platforms.

Additionally, while CFRP has a relatively high thermal conductivity near room temperature, the thermal conductivity quickly decreases with decreasing temperature, giving CFRP a lower conductivity per volume fraction of fibres than the more common glass fibre insulating supports [65]. As a result, CFRP struts are also commonly used to support cryogen tanks on spacecraft. CFRP supports have been used successfully as low conductivity, low expansion supports for the support between the optical bench, liquid helium tank, and general framework of the Herschel Space Observatory [66].

A new method of using CFRPs in space applications is emerging in the form of novel mirror structures. Telescope reflectors must be constructed with materials with a high dimensional stability. Common materials used are metals with a well known CTE, such as aluminum and beryllium, or glass materials with a very low CTE, such as Zerodur or fused silica. CFRPs are promising because they can be manufactured to have a low CTE in addition to a lower density than zero expansion glass. Future space missions such as SPICA and FIRI are considering CFRP for this purpose [67].

There are, however, concerns over using CFRP for dimensionally stable reflecting components. These are associated with the variability and anisotropicity of the material properties when using different sub-materials and fabrication methods, the degradation of the materials over multiple thermal cycles and exposure to harsh environments, and the outgassing of polymer matrix materials in a vacuum [68, 69]. In fact, CFRP mirrors were considered for the Herschel Space Observatory, but were not selected because of degradation of the composite from water absorption, causing cracking of the composite on freezing of the water [68]. The thermal and mechanical properties of CFRP composites are highly dependent on the fibre volume fraction, orientation, and the type of materials used and the manufacturing methods for both the fibres and the composites. Therefore, every form of CFRP material will have slightly different properties. In order to understand the dimensional stability qualities of the composite, measurements of the thermal properties of CFRPs must be made each time a new sub-material or manufacturing technique is used.

4.3 Measuring Thermal Properties

The most important properties to measure when considering a CFRP laminate for cryogenic use are the thermal conductivity, and thermal expansion. Additionally, if the intended use of the material involves supporting other components, the tensile/compressive modulus and ultimate strength of the material must be understood. Thermal properties of materials may change drastically with temperature, requiring the characterization of materials over the entire 4 to 300 K range. Moreover, the effects of repeated thermal cycling must be studied to understand potential failure modes due to material fatigue. In this section, the design, fabrication, and operation of an apparatus I have designed and used for measuring material properties of CFRP composites is discussed. The potential for measuring the Young's modulus of materials at low temperatures is also considered. However, since the temperature dependence of Young's modulus is weak [24], and room temperature measurements are relatively simple, cryogenic measurements of mechanical properties were postponed for future work. Determination of the ultimate strength of composites is also not considered, because of the large mechanical forces involved which would be difficult to incorporate into a cryogenic system. The measurement of CFRP properties at cryogenic temperatures is a collaborative project with Glyndwr University, Wales as part of the EU FP7-FISICA programme [70].

4.3.1 Thermal Expansion

The measurement of the thermal expansion of materials relies on precise methods of determining both temperature and displacement. Accurate thermometers, in the form of resistors or diodes, calibrated for an array of temperature ranges, are commercially available. For accurate temperature measurement from 1 to 400 K, both Cernox™ resistance temperature detectors (RTDs) and silicon diodes are commonly used [49]. All thermometers used for measurements in this chapter are Cernox™ and have been calibrated against a Cernox™ factory calibrated sensor with a typical sensor accuracy of 5 mK at 4.2 K up to 40 mK at 300 K [49].

A variety of displacement measuring techniques are available, involving mechanical, electrical (capacitive or inductive), or optical dilatometers. Push-rod dilatometers are the oldest and most frequently used for high temperature applications. In a push-rod system, a sample is placed in a temperature controlled environment with one end of a rod in contact with each end surface, much like in Figure 4.4. The rods extend out of the controlled environment to ambient temperature. With two rods in contact with opposite faces of the sample, the differential displacement in the ends of the two rods, measured with a linear variable differential transformer (LVDT) [71], will determine the thermal expansion of the material. This design confers the advantage that the encoder used to measure displacement does not experience the temperature fluctuations of the sample, and is therefore not prone to thermally induced errors or limited by the operating temperature limits. Uncertainties in the measurement of thermal expansion can arise due to thermal expansion of the rod itself, meaning the apparatus must be calibrated with a material of known thermal expansion, typically a pure metal. Additionally, a mechanical contact with a temperature controlled sample will lead to parasitic heat transport through the rod. At elevated temperatures, this may be an acceptable heat loss but at cryogenic temperatures, cooling powers are limited and heating due to parasitic conduction from a rod at ambient temperature can quickly overload the cooling power of the system.

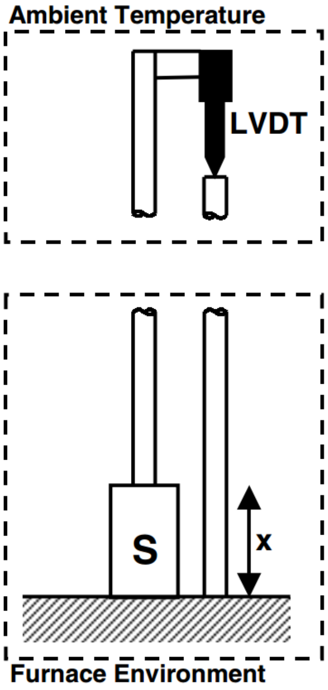

Figure 4.4: An example of a mechanical dilatometer for the measurement of thermal expansion of a sample, S in the figure [72].

Capacitive methods may also be used to measure thermal expansion. The capacitance of a parallel plate capacitor depends on the separation of the parallel plates, d, according to the relation [27],

$$C = \varepsilon \frac{A}{d}, \qquad \text{(F)} \quad (4.2)$$

where ε is the permittivity of the dielectric between the capacitor plates, and A is the area of the smaller plate.

A system in which the expansion of a material changes the distance between two charged, parallel plates could be used to measure thermal expansion. This method is useful over any temperature range but is especially useful at low temperatures, where thermally induced vibrations are diminished, allowing for a more precise capacitance measurement. While this method has proven to work in laboratory tests of solids and as a high precision metrology device for space instrumentation [73], this method was not adopted for our purposes. Capacitance measurements are susceptible to noise induced by external vibrations. The pulse tube cooling system operates on the principle of rapid, adiabatic expansion and compression of helium gas, which induces vibrations by nature of its operation. Despite attempts to mitigate the transfer of vibrations from the pulse tube to the sensitive measurement area, we could not quantify the level of vibrational damping during the design process, and therefore decided on an alternate measurement method.

The method selected for thermal expansion measurements was the interferometric technique. We chose a differential interferometer to reduce measurement errors due to vibration. Additionally, the ease of operation of the stabilized laser source and detector, positioned at room temperature, were factors in the selection of this technique. The instrument selected for the task was a Renishaw RLU10 laser unit with an RLD10 differential laser interferometer and detector head [52].

The Renishaw differential interferometer (DI) measures the relative displacement between two plane mirror targets using a fibre-fed HeNe laser. The differential nature of the measurement eliminates common mode errors along the measurement axis. The DI is mounted on the outside of the vacuum chamber, emitting laser beams into the cryostat through a viewport. The interferometeric components and detector are all located inside the DI head. The interferometer is laid out in a double pass configuration, as shown in Figure 4.5, increasing the sensitivity of the instrument.

Due to the long cool down times involved, and the relative nature of the measurement, the interferometer output had to be recorded continuously for durations of over 24 hours. Unfortunately, the software provided with the product only allowed a 20 s maximum recording time. To provide sufficiently long time series measurements, we designed a custom electronic interface based on microcontrollers that would allow us to use our own software to log data at high resolution for arbitrary time scales. USB-based microcontrollers (Teensy++2.0 [74]) were employed to interface with a Renishaw RPI20 module with a PC. The module accepts analogue 1 V_{pp} sine/cosine signals, converting them into a 36-bit word,

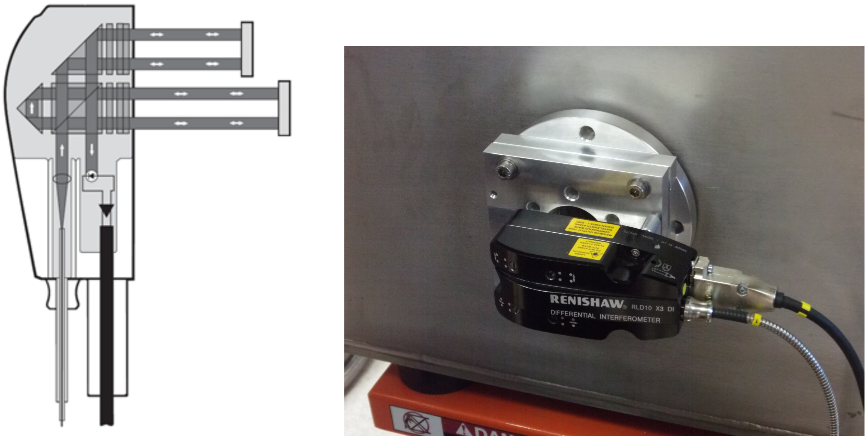

Figure 4.5: (Left) A schematic showing the interferometric components of the Renishaw Differential Interferometer. (Right) An image of the Renishaw Differential Interferometer and custom fabricated mounting plates attached to the Test Facility Cryostat.

and recording positional data with a least significant bit (LSB) corresponds to a resolution of 38.6 pm. The controllers were set up as a master-slave configuration, where the only function of the slave controller was to poll the differential interferometer for displacement readings. In this way, interrupts could be turned off in order to increase the sampling rate. The microcontroller read the 36-bit position encoder output from the DI with an external digital clock trigger since the microcontroller was not capable of real-time time stamping. Overflow conditions were included in the microcontroller code, using an external 16-bit counter, since missing a single sample would corrupt the time series. Data collection was started and stopped using the master microcontroller, to avoid slowing the collection rate of the slave controller by polling the serial port for commands. The maximum continuous reading frequency before the overflow condition was triggered was 17 kHz. For this application, 5 Hz sampling over a period of several hours was sufficient and produced manageable file sizes. A block diagram of the modules responsible for the data collection circuit is shown in Figure 4.6. A full circuit diagram of the microcontroller module and an explanation of the control software are shown in Appendix C.

The initial attempts to measure the temperature-dependent thermal expansion of CFRPs employed an existing cylindrical cryostat, which operated with a single Cryomech PT415

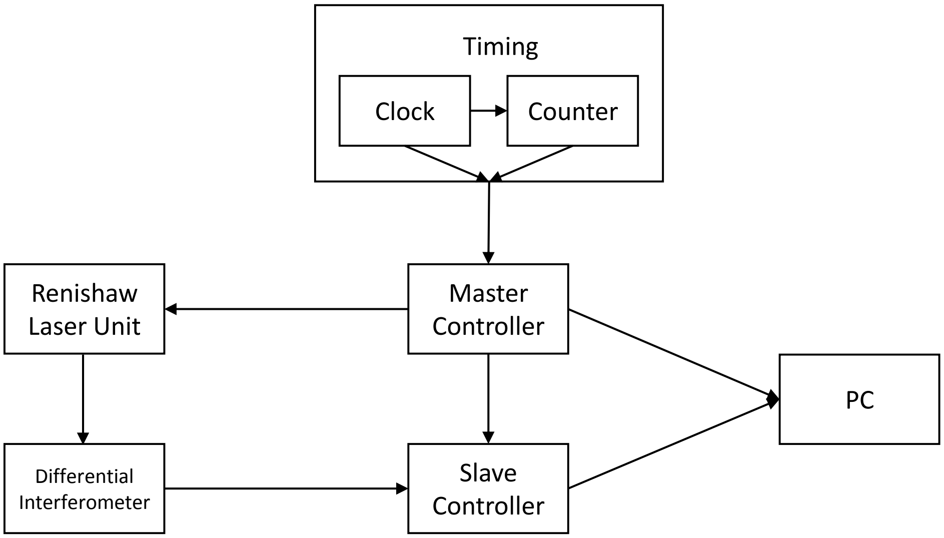

Figure 4.6: A block diagram of the dual microcontroller set up to read displacement data from the differential interferometer. See Appendix C for more information on the circuit and the control software.

Table 4.1: Renishaw differential interferometer detector head specifications.

Beam Diameter	3 mm
Beam Separation	7 mm x 14 mm
Alignment tolerance	$\pm 25''$
Beam alignment adjustment	$\pm 1^\circ$ pitch $\pm 1^\circ$ yaw
Maximum differential range	1 m
Sample rate	17 kHz
Resolution	38.6 pm

pulse tube cooler, was repurposed for the task (Figure 4.7) [40]. The thermal expansion measurement system was a configuration of struts arranged as a hexapod with aluminum end plates (Figure 4.8). In order to simplify the measurements and make best use of the available space, the hexapod was required to be aligned along the cylindrical axis of the cryostat, but the original 4 K cryostat was constructed with viewports only on the side walls of the vacuum chamber. A fold mirror was added to the hexapod structure in order to direct the DI measurement beam along the axis of the hexapod. Plane mirror targets were placed beside the fold mirror for the reference beam and on the bottom plate of the hexapod for the measurement beam.

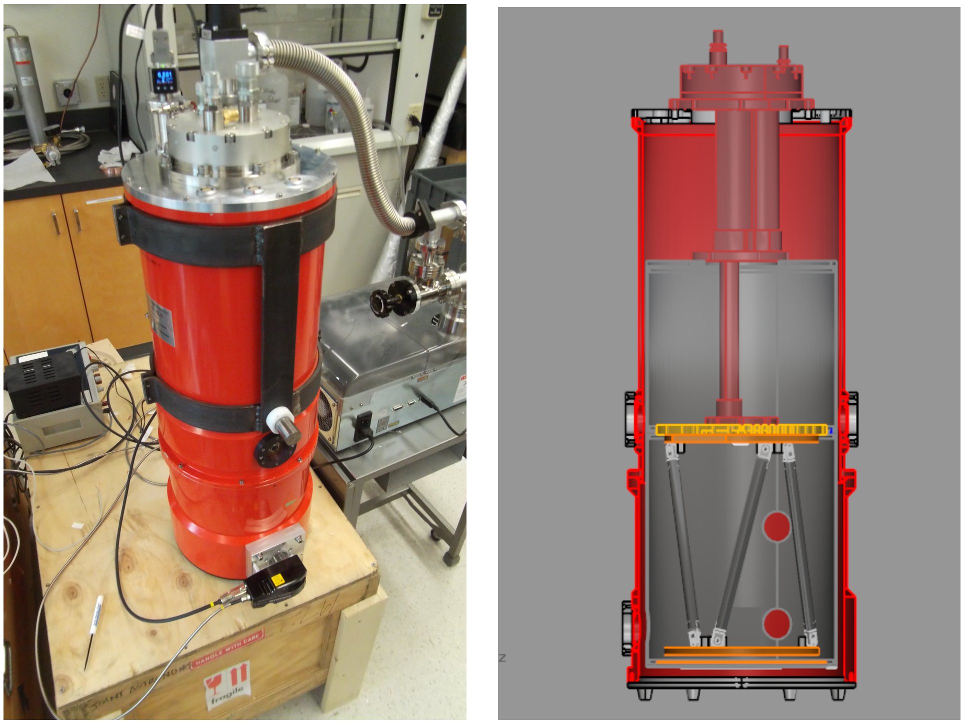

Figure 4.7: (Left) An image of the smaller, cylindrical 4 K cryostat and pulse tube cryocooler. (Right) A cutaway view of the cylindrical cryostat showing the 45 K and 4 K pulse tube heads as well as the 4 K cold plate and 45 K shields. The hexapod with CFRP struts is shown hanging from the 4 K plate.

In the original cryostat, there was no mechanical decoupling of the pulse tube from the 4 K plate in place. Therefore, alignment errors of the DI from vibrations induced by the operating pulse tube proved to be difficult to correct, despite the differential nature of the

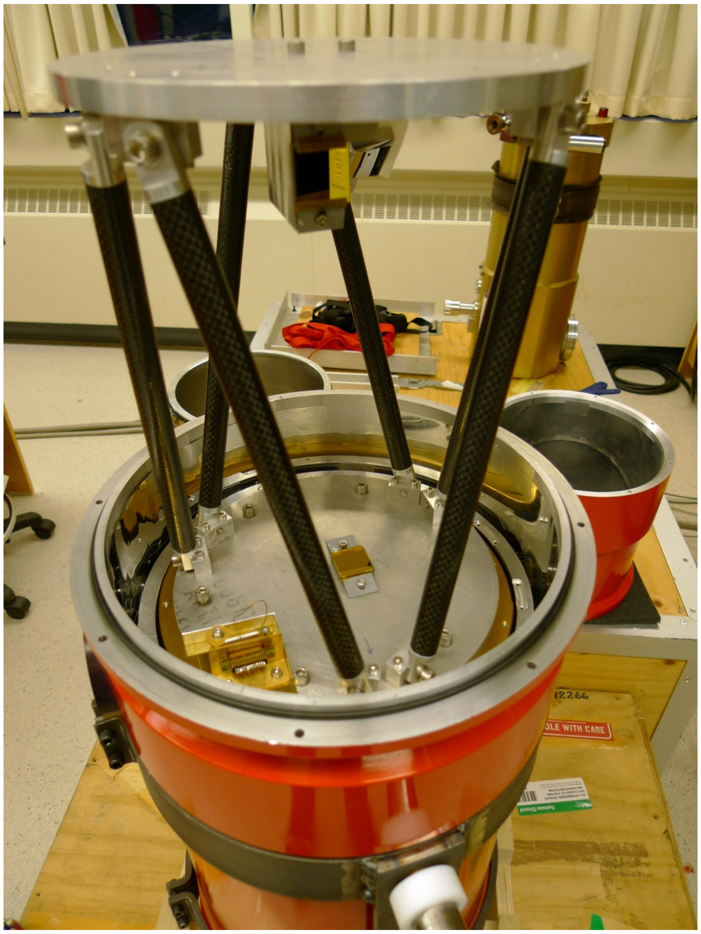

Figure 4.8: The original hexapod design. A 45° fold mirror is on the underside of the upper aluminum plate, reflecting a reference metrology beam and directing a measurement beam along the contraction axis.

measurement. The presence of an optical viewport to interface with the Renishaw DI also proved to be a drawback. The high absorptivity of the CFRP support rods, along with their low thermal conductivity at cryogenic temperatures, led to difficulties in cooling the system. The design was modified several times, in attempts to mitigate the vibrational effects. The fold mirror was removed in favour of a bottom-facing window and the hexapod was replaced with a straight-legged tripod system in order accommodate additional radiation shielding in the cylindrical cryostat, and to allow for different sample sizes and geometries to be used with the system (Figure 4.9).

Even with the upgrades to the thermal expansion measurement system, measurements were still plagued with misalignment errors due to the non-uniform cooling of the system

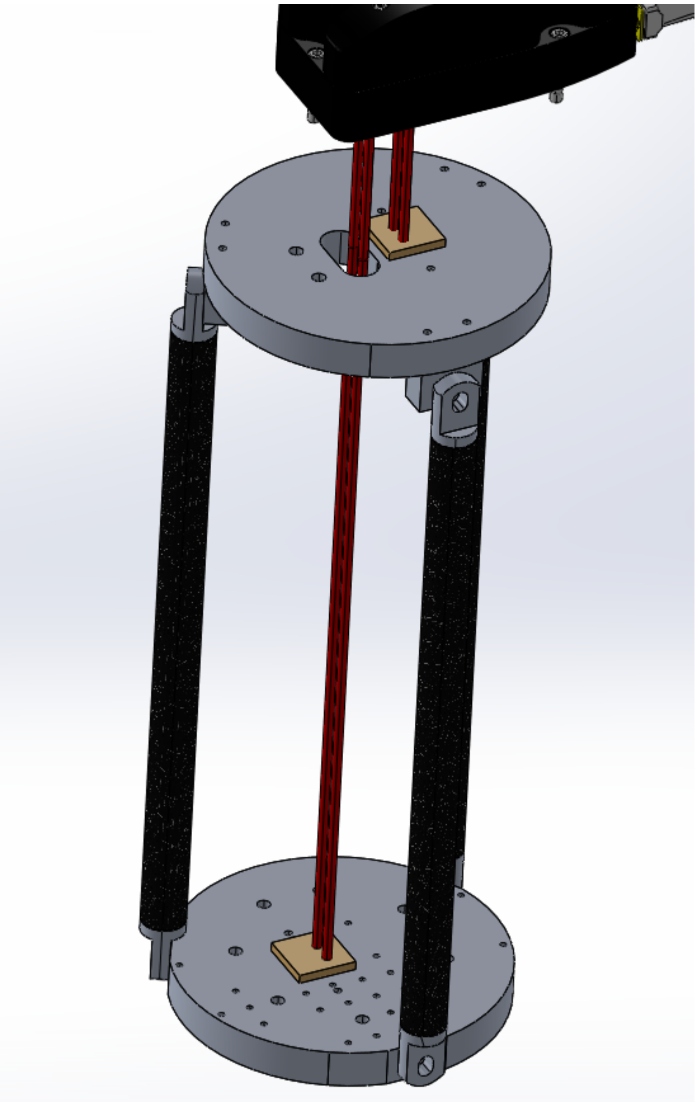

Figure 4.9: The straight-legged tripod system with an on-axis interferometer.

and insufficient mechanical tolerances. Additionally, vibration of the cold stage limited the measurement resolution to the order of 1 μm. Solutions to these issues were deferred until the completion of the Test Facility Cryostat (TFC) (Chapter 3). Flexible thermal straps between the pulse tube and the cryostat components were incorporated into the design of the TFC, under the anticipation that these would provide a sufficiently isolated measurement platform for accurate thermal expansion measurements.

In collaboration with Glyndwr University, Wales, CFRP plates were constructed for use with the tripod system (Figure 4.10). Plates were constructed rather than rods because it was easier to lay out *prepreg* on a flat mandrel than to wind it around a cylindrical mandrel. Six sets of three plates each were constructed for thermal expansion measurement. These were comprised of two sets each of quasi-isotropic, 0° and 90° fibre orientation with respect to the tripod axis. With the DI mounted on a 50 mm viewport located on the short side of the outer vacuum chamber (OVC), the CFRP plate tripod was positioned horizontally inside the 4 K volume, facing the viewport (Figure 4.11). The 0° and 90° fibre oriented samples provided a means to measure the contribution of the fibres and resin respectively to the overall thermal contraction of a quasi-isotropic sample.

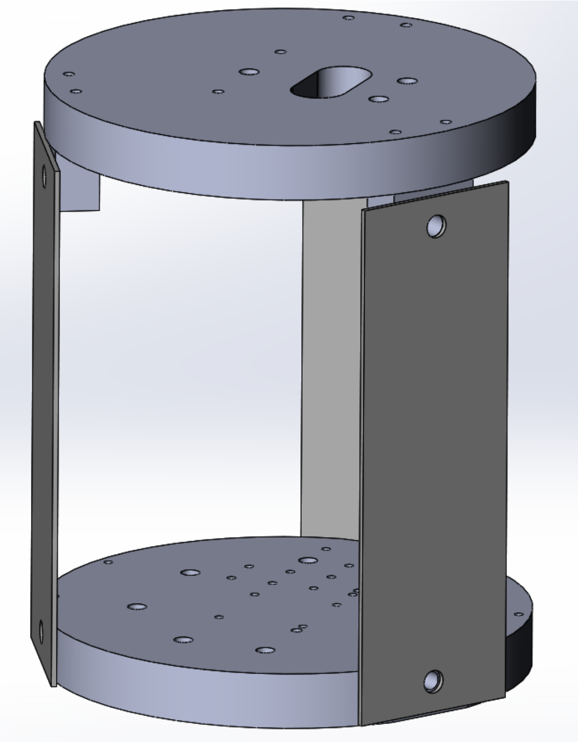

Figure 4.10: A rendering of the 3D CAD design for the plate tripod. Mirrors are placed on the top and bottom plate, and serve to reflect the measurement and reference beam from the DI. The model was designed in Solidworks [75].

Thermal expansion was measured with the DI down to an average plate temperature of 20 K. Results of the thermal expansion measurements are shown in Figure 4.12. The lower vibrational effects of the pulse tube in the test facility cryostat as compared to the older vessels ensured the mirrors stayed perpendicular to the DI beams during the entire cooling

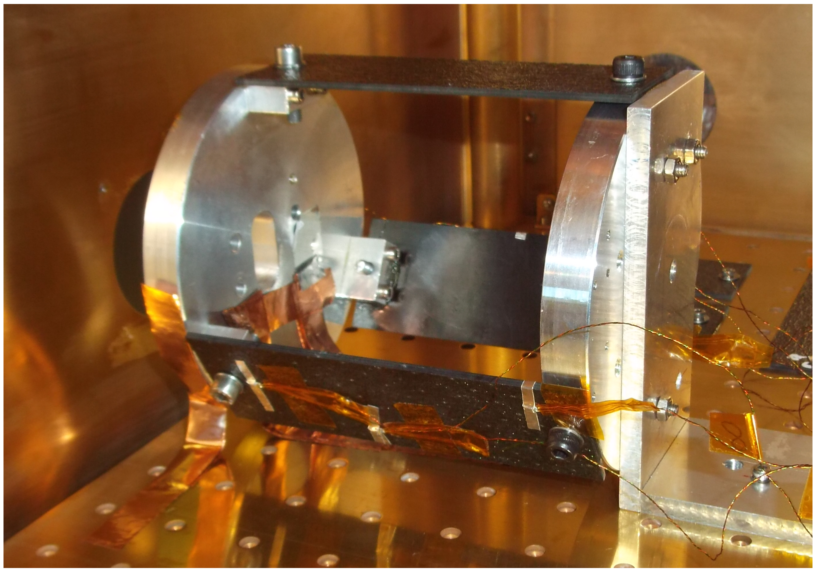

Figure 4.11: The straight-legged tripod system with CFRP plate samples installed. The system was positioned horizontally inside the TFC with the DI beams entering from a side viewport. Cernox™ RTDs are located at three positions on the CFRP plate, measuring the temperature gradient.

process. The slow cool down time of the TFC also allowed for a smaller thermal gradient across the CFRP plates during the cool down. Base temperatures of the CFRP plate tripod were still higher than the nominal 4 K, due to room temperature radiant loading from the laboratory.

The thermal expansion curves followed an expected trend, with the contraction along the fibres, 0°, being less than contraction of the resin orthogonal to the fibres, 90°. This was due to the higher thermal expansion of the polymeric resin compared to the carbon fibres. The expansion curve of the quasi-isotropic sample fell in between (Figure 4.12).

In order to determine the reliability of the tripod measurement technique, the tripod was calibrated using plates with the same dimension as the CFRP plates, but with a known thermal expansion, aluminum being the chosen material. The expansion of the aluminum tripod was measured as the TFC cooled. The results in Figure 4.13 show that the system accurately measured the contraction of aluminum, to within 2% error.

In the future, radiant loading will be reduced to achieve a lower base temperature of the samples. To achieve base temperatures of 4 K, I have designed a cryogenic, zero aperture

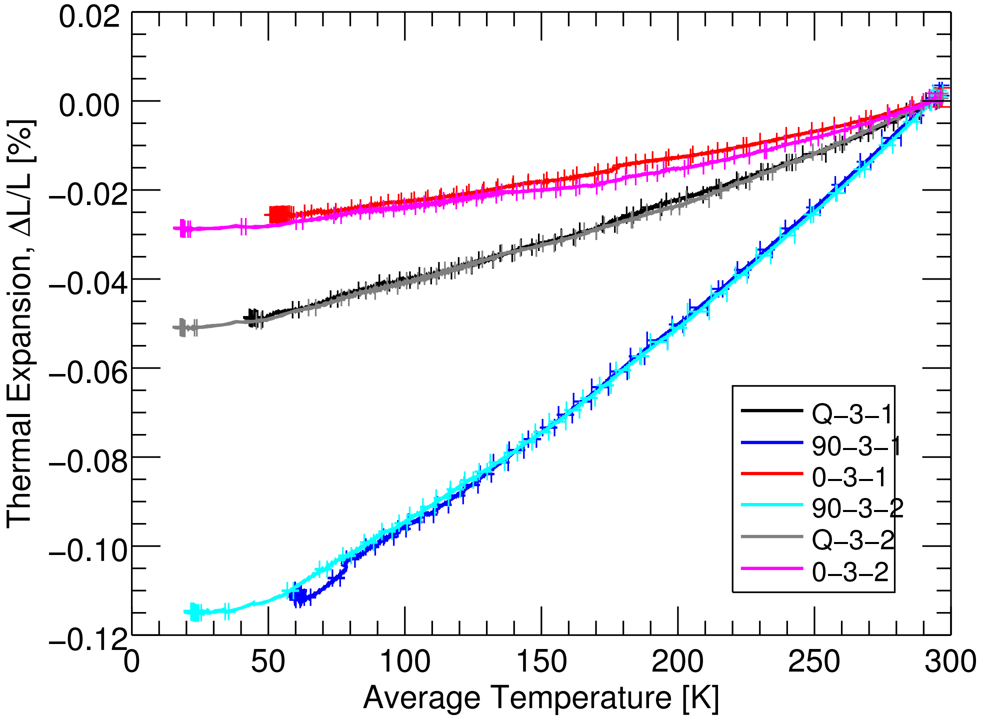

Figure 4.12: Thermal expansion results of the CFRP plates from room temperature to 20 K. As predicted, the 0° fibre samples experience less thermal contraction than the 90° samples. Error bars shown are shown ever 50 data points and represent 1σ uncertainties. The temperature uncertainty was the dominant source of error, due to the thermal gradient present along the CFRP plates while cooling.

iris which will be operated by a cryogenic, high-vacuum Phytron stepper motor [76]. The 4 K iris will remain closed for the duration of the cool down to 4 K after which the stepper motor will open the iris so thermal expansion may be measured on the warm up cycle (Figure 3.13).

4.3.2 Thermal Conductivity

In order to determine the thermal conductivity of a typical CFRP sample, thermal tests were performed to measure the heat conduction along a single CFRP strut. In a previous measurement, from a previous member of the AIG, one end of the strut was bolted to the 4 K stage and Cernox$^{\text{TM}}$ RTDs were attached to both ends. A resistor heater was attached to

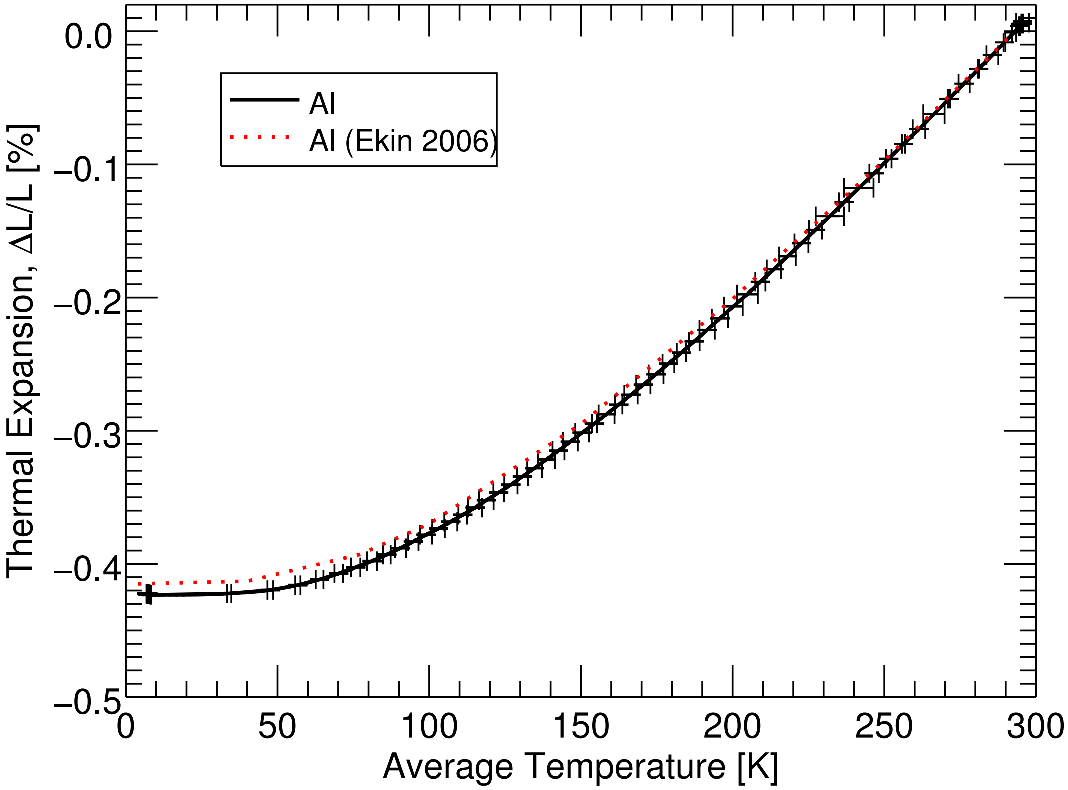

Figure 4.13: The tripod thermal expansion technique was calibrated using aluminum plates. This figure shows the measured thermal expansion of the aluminum in comparison to tabulated values found in [24]. The thermal expansion values show a systematic 2% offset from the tabulated values. Error bars are shown every 50 data points.

the free end of the strut. It was found that a constant heater output of 160 μW was required to maintain a temperature of 60 K at the warm end [37]. This gave an average thermal conductivity, λ, of around 15 mW m^{-1} K^{-1} from Equation 2.21. This experiment was conducted before 4 K radiation shields were in place and the technique did not account for heat load due to radiative transfer from the 45 K shields. Therefore, this thermal conductivity value for the average CFRP temperature was expected to be slightly lower than the actual conductivity.

In order to improve accuracy, the thermal conductivity of this type of CFRP rod was measured over the entire temperature range from 4 K to 300 K. In this experiment a short

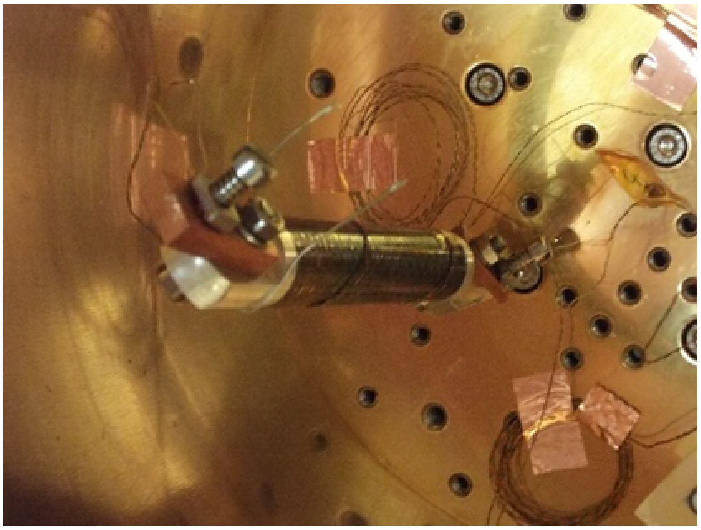

Figure 4.14: An image of the CFRP rod with one end bolted to the 4 K plate and the other end attached to a block of copper. The heat capacity of the copper, aluminum cap, stainless steel bolt, and thermometer clamp were all taken into account when calculating the flow of heat through the CFRP.

CFRP rod with aluminium end caps was bolted at one end to the 4 K stage. With thermometers on both ends of the rod, the temperature gradient across the rod was measured as the rod was cooled (Figure 4.14). The power flow through the rod was calculated for each successive measurement, using temperature information, as well as the specific heat of the aluminium end cap and copper thermometer block attached to the free end of the strut, with corrections for radiative transfer and heat flow through thermometry wiring. The total rate of heat flow was found by the equation,

$$\dot{q} = \frac{Q}{\Delta t} = (m_{Cu}c_{Cu} + m_{Al}c_{Al} + m_{SS}c_{SS})\Delta T/\Delta t \qquad \text{(W)} \qquad (4.3)$$

where m was mass, and c was specific heat at constant pressure for the copper, aluminum, and stainless steel, Δt was set to be 30 s, ΔT was the change in temperature of the copper block over the time interval, and Q was the heat leaving the system.

The rate of heat flow through the wires, $\dot{q}_{wire}$, was calculated using Equation 2.21, and the rate of heat flow as radiative transfer to the environment, $\dot{q}_{rad}$, was calculated using Equation 3.1, where the emissivity, ε, of CFRP was set to ~ 1 and the emissivity of the gold coated environment was ~ 0.03. Heat flow through the CFRP was found by,

$$\dot{q}_{cfrp} = \dot{q}_{tot} - (\dot{q}_{wire} + \dot{q}_{rad}) \,. \qquad \text{(W)} \quad (4.4)$$

The rate of heat flow through the CFRP was equated to Fourier's Law (Equation 2.21) to achieve a range of values for,

$$\dot{q}_{cfrp} L/A = \int_{T_1}^{T_2} \lambda(T) dT, \qquad (\text{W m}^{-1}) \quad (4.5)$$

where T_1 and T_2 ranged from 4 to 295 K.

Using the additive property of the ranges of definite integrals,

$$\int_a^b f(x)dx = \int_a^c f(x)dx + \int_c^b f(x)dx, \qquad (4.6)$$

a dataset was created of the form,

$$F(T) = \int_{4\,\text{K}}^{T} \lambda(T')dT'. \qquad (4.7)$$

This dataset was fit with a high order polynomial (6th order), as shown in Figure 4.15. Using the fundamental theorem of calculus,

$$F(x) = \int_a^x f(x)dx \rightarrow F'(x) = f(x), \qquad (4.8)$$

the thermal conductivity was found by taking the derivative of the 6th order polynomial fit with respect to temperature. The temperature dependent thermal conductivity of the CFRP rod is shown in Figure 4.16.

Finally, following standard practice laid out by NIST [77], the temperature dependent

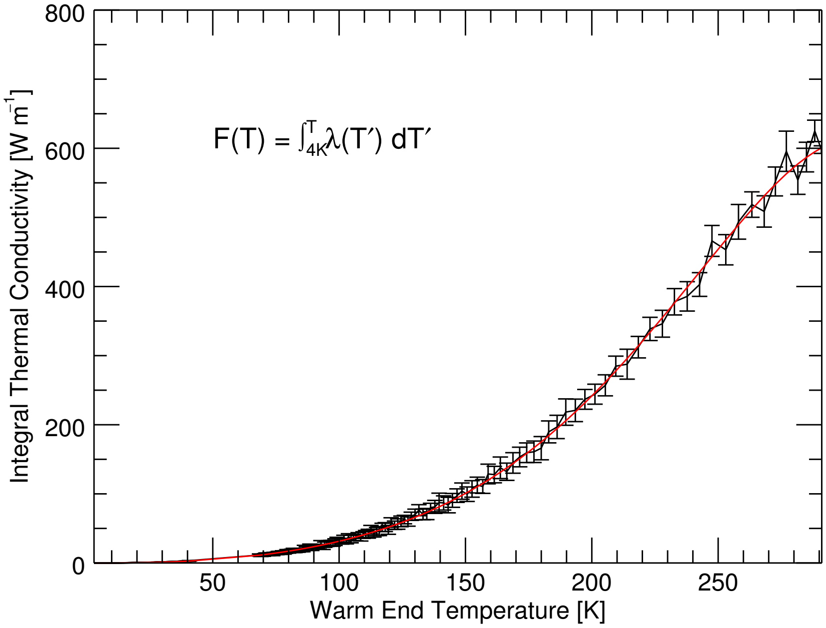

Figure 4.15: The integrated thermal conductivity, expressed as a function of warm end temperature, with the cold end temperature set to 4 K. The red curve is a 6th order polynomial fit.

thermal conductivity data was fit with an equation of the form,

$$\log(\lambda) = a + b\log(T) + c(\log(T))^2 + d(\log(T))^3 + e(\log(T))^4 + f(\log(T))^5 + g(\log(T))^6 + h(\log(T))^7 + i(\log(T))^8. \quad (4.9)$$

The fit values for coefficients are given in Table 4.2. This functional fitting form is used for all materials in NISTs cryogenic material properties database [77]. From Figure 4.16, this functional form provided an accurate fit to within 0.4% from 4 to 250 K. The thermal conductivity result for CFRP was then compared to a variety of other common cryostat materials, as shown in Figure 4.17.

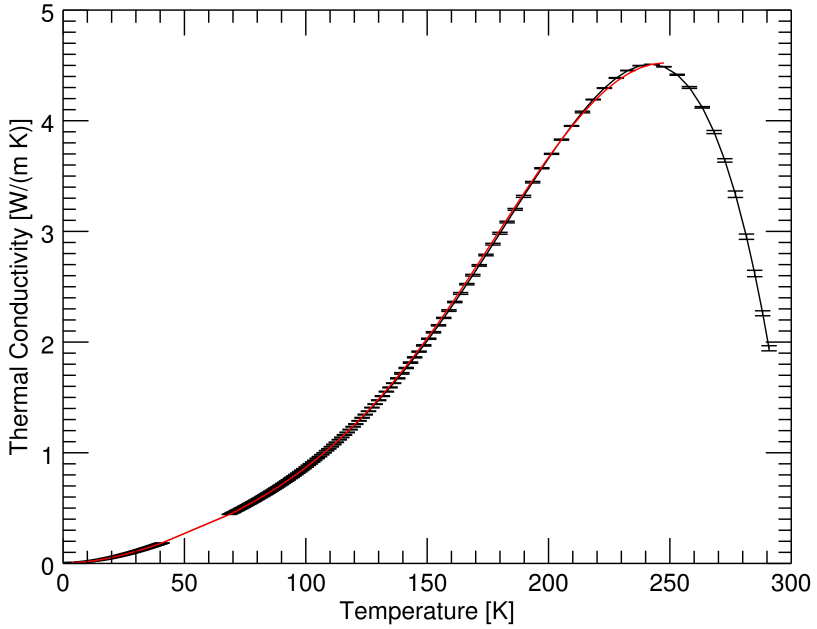

Figure 4.16: The thermal conductivity of the CFRP rod as a function of temperature. The lack of error bars between 40 K and 70 K is the result of a PC malfunction and a lack of data collected in that temperature range. A functional fit of the form shown in Equation 4.9 is shown from 4 to 250 K, overlaid in red.

4.4 Conclusion

The drive for the fabrication of composite materials, such as CFRP, was outlined in this chapter. In addition, the process of making CFRP was discussed, and the large variation of thermal and mechanical properties between samples was explained. Due to the importance of understanding material properties for cryogenic instrumentation, techniques for measuring the thermal expansion and thermal conductivity of CFRP samples were outlined and results were discussed.

Table 4.2: Fit coefficients.

Coefficient	Value	Uncertainty
a	-7.74	0.07
b	17.7	0.2
c	-23.4	0.3
d	17.1	0.2
e	-7.43	0.08
f	2.02	0.02
g	-0.337	0.003
h	0.0316	0.0003
i	-0.00126	0.00001

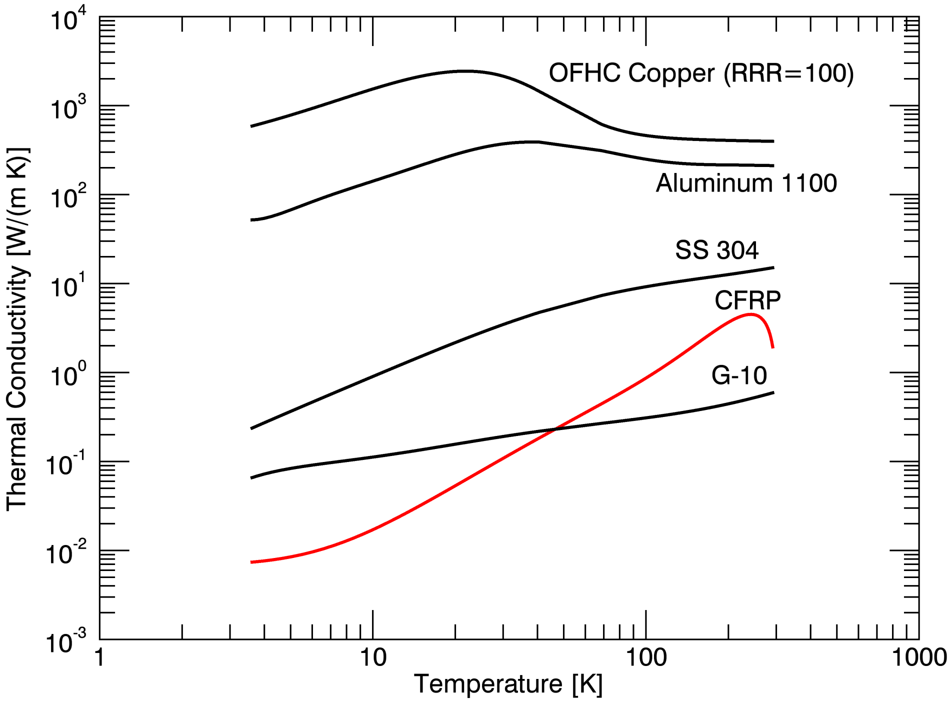

Figure 4.17: The thermal conductivity of CFRP rods purchased from McMaster-Carr (Part # 5287T32), shown in red, from room temperature to 4 K. The thermal conductivity of other common cryostat materials is shown as a comparison. Data for the thermal conductivity of these materials was taken from the NIST cryogenic material properties database [77].

Chapter 5

Progress Towards a Cryogenic FTS

The test facility cryostat (TFC), described in Chapter 3, was designed to provide a suitable 4 K environment for testing interferometer delay line metrology techniques as well as for characterizing the thermal, mechanical, and optical properties of materials at low temperatures. The initial plan was to procure the flight spare scanning mechanism of the Herschel/SPIRE instrument [15]. Unfortunately, the procurement process faced several logistical challenges and, since there was only one flight spare, it was decided that the risk was too great. Instead we chose to modify the scanning mechanism from a commercial laboratory Fourier transform spectrometer (FTS) for operation at cryogenic temperatures. This will allow us to evaluate the performance of an internally mounted, fibre fed laser as a FTS metrology system and the integrated performance of the interferometer at cryogenic temperatures. With the TFC, we will be able to install a 0.3 K refrigerator with bolometer detector, as well as a low temperature blackbody source, within the 4 K enclosure to allow for low background tests of the FTS performance.

5.1 Wishbone FTS Modifications

The FTS scanning mechanism to be modified was removed from a defunct ABB IR spectrometer, and is of the double pendulum design (Figure 5.1). The system is referred to as the wishbone interferometer (WBI). This type of interferometer was selected because of its compact structure and voice-coil driven, frictionless flex-pivot moving mechanism; both of which contribute to its suitability for use at cryogenic temperatures.

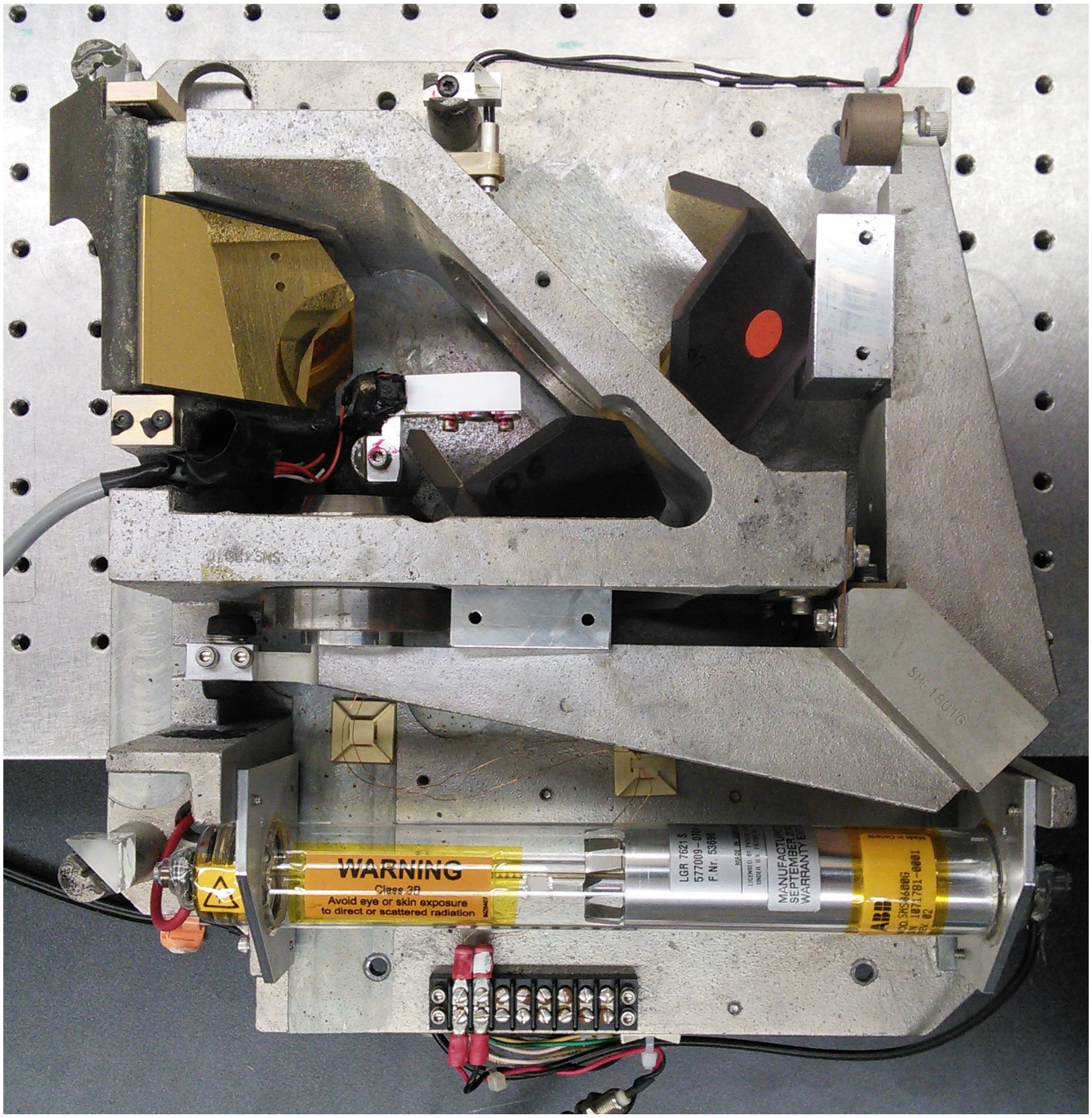

Figure 5.1: The ABB inteferometer with wishbone mechanism, original dual corner-cube retro-reflectors, and original IR beamsplitter. Also shown is the metrology system, consisting of a single-mode HeNe laser, beam stearing optics, and detector.

The WBI operates by deflecting the wishbone arm with a voice coil. Rotating the arm increases the optical path length of one interferometer beam, while simultaneously decreasing the path length of the other. Interference of the combined beams with a changing optical path length results in an observed interferogram. In the typical laboratory configuration, a HeNe laser beam running parallel to the infrared beam passes through the beam splitter off-axis, through apertures in the IR reflective beam splitter coating. A separate detector measures interference fringes from the monochromatic source to provide accurate optical path delay metrology. The optical path is shown in Figure 5.2. While this is an elegant design, the HeNe laser could not be used within a cryogenic system. We proposed to use an internal, fibre launched laser metrology beam to evaluate the performance of the WBI.

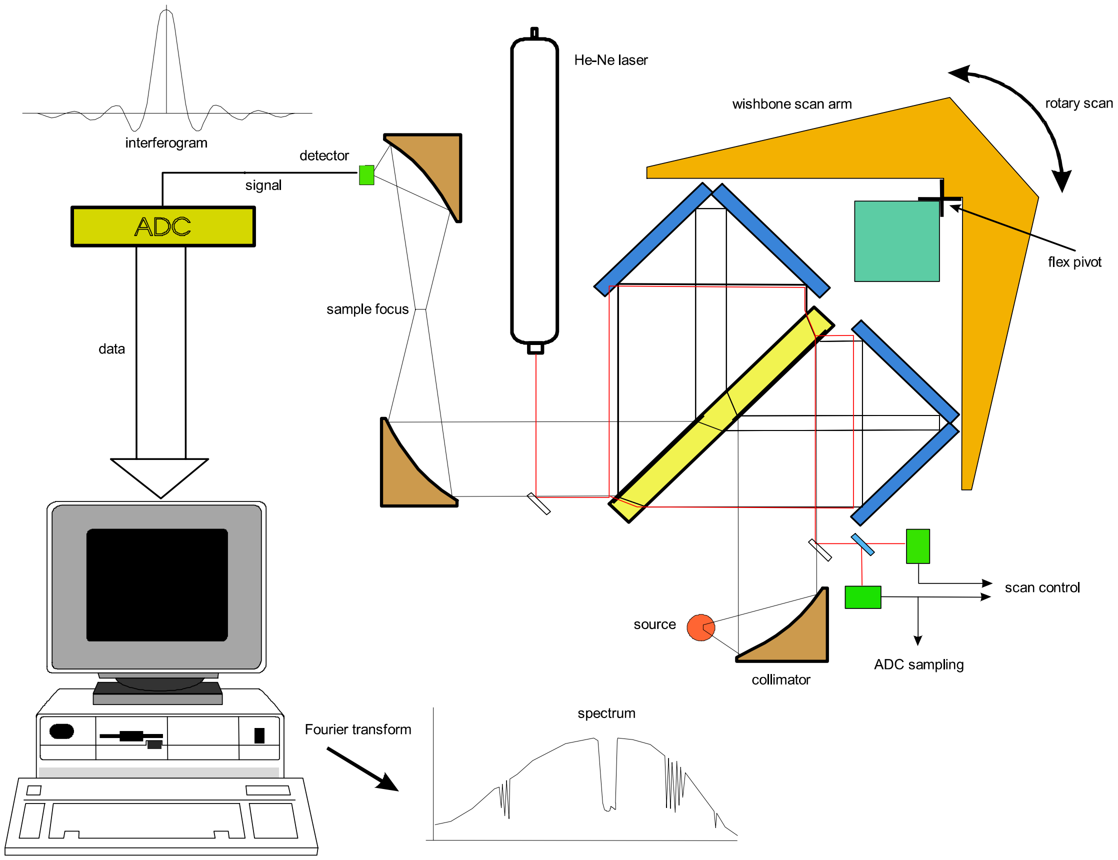

Figure 5.2: Schematic showing the ABB interferometer optics as well as the measurement and metrology beams.

Before modifying the ABB FTS, the likely modes of failure were identified, and their

Table 5.1: Risk assessment matrix

			Solution	
Risk	Severity	Proposed	Prototyped	Finalized
Voice Coil	Medium	X	X	X
Beamsplitter	High	X	X	
Mirrors	Medium	X	X	X
Flexure Bearings	Low	X	X	X
Metrology	High	X		
Source	Medium	X		
Detector	Low	X		

probability of failure and severity where characterized in a risk assessment matrix, shown in Table 5.1. The severity of the risk was determined qualitatively by assessing the likelihood of failure as well as the importance of the subsystem for the over functionality of the WBI.

The FTS mechanism framework was trimmed to minimize the thermal mass and simplify mounting within the cryostat, as shown in Figure 5.3. The ZnSe beamsplitter was replaced with a custom made, FIR beamsplitter that allowed the full 50 mm aperture to be used, instead of the smaller sheared beams in the original design. In the proposed performance testing of the WBI, off-axis parabolic mirrors will couple the parallel interferometer beam to a small low-temperature blackbody source and f/3 feedhorn-coupled bolometer, as shown in Figure 5.4.

The voice coil actuator, flex pivot, and optical components were also tested for operation at 4 K, as described in the following sections.

5.1.1 Hall Effect Sensor Calibration

In order to determine the temperature dependence of the magnetic field in the permanent magnet used in the voice coil for the WBI, a Hall Effect sensor was used to measure the field as the magnet was cooled. An Infineon Hall Effect Sensor was selected for use inside the cryostat, for its high sensitivity, linearity, and measurement range (0 mT to 100 mT). The integrated amplifiers in the chip, however, required an operating temperature of $>$130 K. A

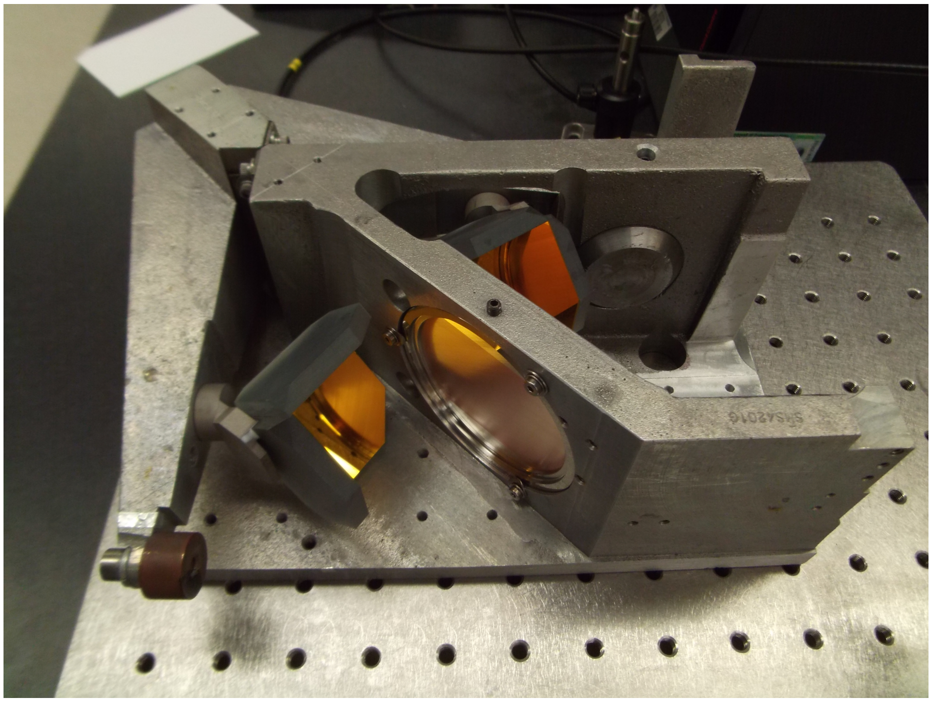

Figure 5.3: The ABB FTS mechanism trimmed down to minimize thermal mass, and retrofitted with optimal corner-cube mirrors and FIR beamsplitter.

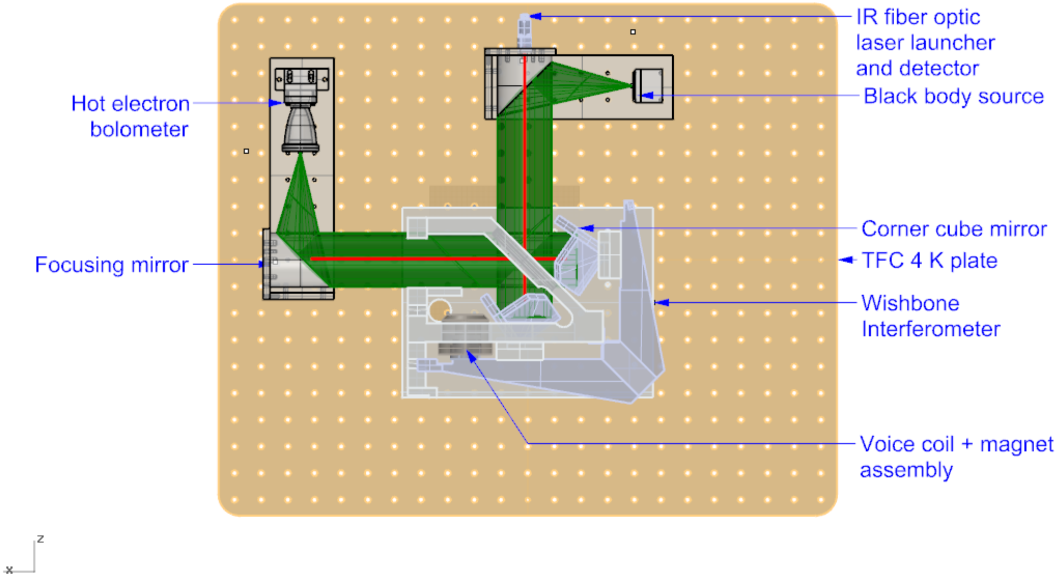

Figure 5.4: Schematic of the planned optical layout for the cryogenic Michelson FTS on the 4 K plate, including the wishbone mechanism, two off-axis parabolic reflectors, infrared metrology, low temperature blackbody source, 4 K detector and feedhorn.

simple platform, isolated with stainless steel bolts and heated by a servo-controlled 1 kΩ resistive heater, was constructed in order to maintain sensor at 130 ± 1 K (see Figure 5.5). The required operational temperature was determined by cooling the sensor and measuring its temperature response to the magnetic field generated by the solenoid extracted from the WBI voice coil driver. The resulting change in magnetic sensitivity with temperature is shown in Figure 5.6.

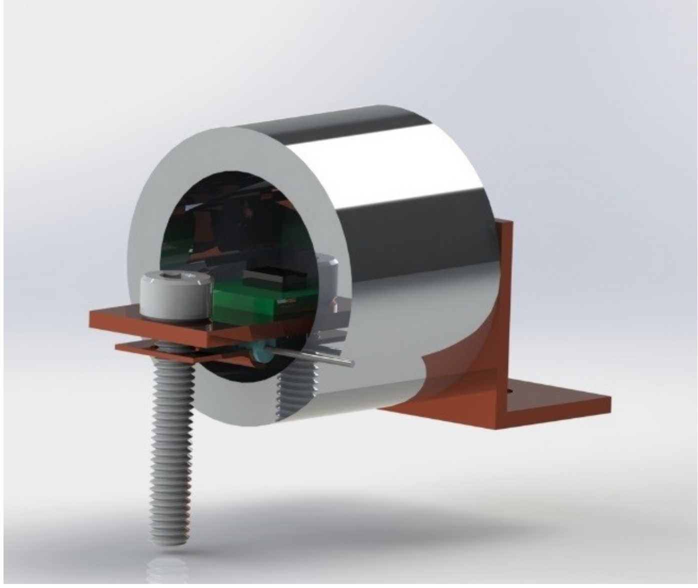

Figure 5.5: Setup for measuring the 4 K performance of Hall effect sensor within the solenoid

5.1.2 Magnet specifications

The permanent magnet used by WBI is a HICOREX rare-earth cobalt magnet. These magnets are suitable for extreme temperature operation, exhibiting only small reversible changes in magnetic properties when exposed to low temperatures. Rare-earth cobalt magnets such as Samarium-cobalt, however, are known to be prone to fracture when subjected to thermal shock. To minimize thermal gradients during the cooling process, the magnet was press fit into an aluminum mount, allowing the magnet to cool in a radially symmetric fashion.

The percentage change in the magnetic field strength was measured using the cali-

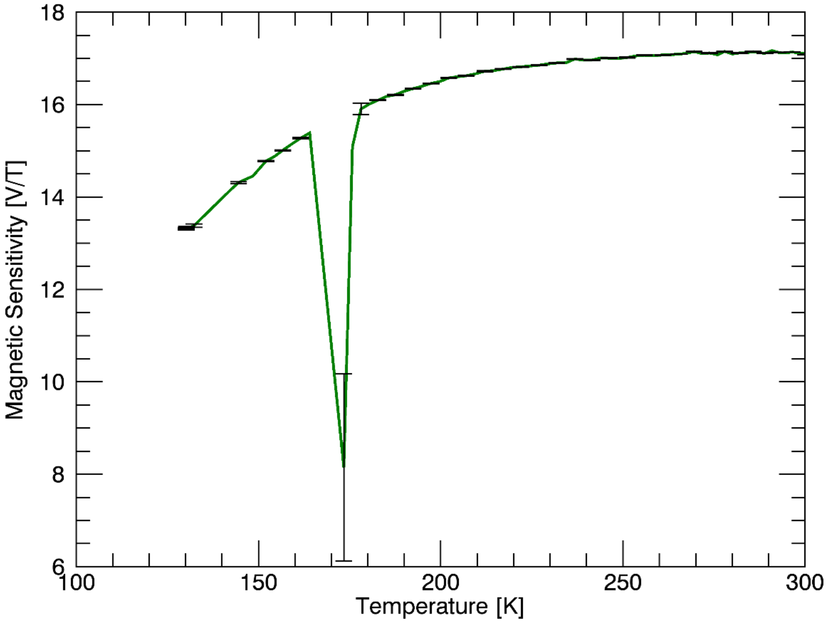

Figure 5.6: Temperature dependent calibration curve for the Infineon Hall Effect sensor with integrated amplifier electronics. Below 130 K, the magnetic sensitivity dropped sharply to zero. Measurements at a temperature range between 160 K and 180 K were disregarded because of the high uncertainty, repeatable anomaly present in that temperature range.

brated Hall Effect sensor, described in Section 5.1.1. The actual magnetic field strength was ∼180 mT, exceeding the measurement range of the sensor. Therefore, a relative percentage change in the magnetic field strength was measured by placing the sensor in a location where the magnetic field strength was weaker, ∼2 cm away from the permanent magnet. Figure 5.7 shows the percentage change in the magnetic field of the permanent magnet from room temperature to cryogenic temperatures. A relative increase in the magnetic field strength was recorded, due to smaller thermal fluctuations in the magnetic dipole moment at low temperatures. Multiple thermal cycles to 4 K reveal that the change in field strength was reversible, with a small amount of hysteresis (∼6 %). From these results, we confirmed the voice coil would function at 4 K.

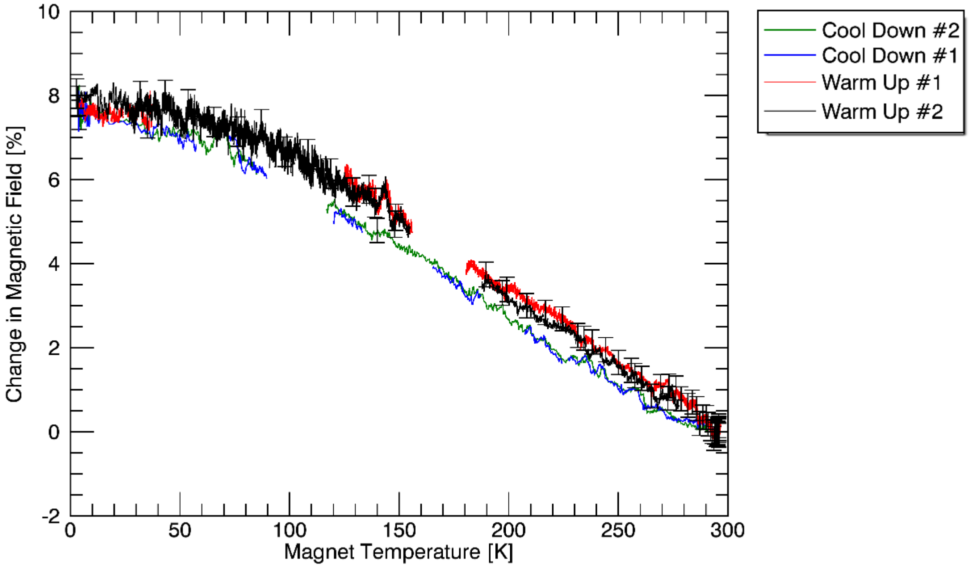

Figure 5.7: Percentage change in the magnetic field strength of the permanent magnet of the WBI voice coil. Measurements were taken over two complete thermal cycles of the magnet to 4K. Offset between the cool down and the warm up curves demonstrates a small amount of hysteresis upon thermal cycling. All magnetic field strength changes are reversible.

5.1.3 Voice Coil Solenoid

The temperature dependence of the magnetic field strength of the solenoid is only dependent on electrical current, as expressed in the equation,

$$B = \mu_0 IN/L \tag{5.1}$$

Therefore, the considerations for selecting a suitable solenoid are limited by the allowable power dissipation, determined by the required current and resistance of the OFHC copper wire at 4 K. Maximum power dissipation was determined to be ~2 mW for maximum displacement. With a Cernox™ thermometer on the solenoid at 4 K, this heat dissipation did not warm up the solenoid by more than 0.1 K. Therefore, the OFHC copper wire was determined to be suitable for 4 K operation. In future tests, the OFHC wire could be replaced with NbTi wire, which is superconducting at cryogenic temperatures, to eliminate Joule heating.

5.1.4 Beamsplitter design

The original WBI IR beamsplitter was made from ZnSe. Semi-reflective coatings were applied on the back side of the top half and front side of the bottom half with uncoated sections on the edges of the beam splitter for the measurement laser. The split design eliminated the need for a compensation plate, but required a smaller (1 $''$) beam diameter. Unfortunately, ZnSe does not transmit beyond ~20 μm. Prof. Peter Ade has provided a broad band beam splitter, similar to that used on Herschel/SPIRE interferometer, for operation in the FIR range. The new beamsplitter has a ”post-box” design with transparent regions that will allow the laser metrology beam to sample the optical path of the interferometer, as shown in Figure 5.8. The beamsplitter was fabricated by hot pressing polypropylene layers together, with a copper mesh grid in the main part of the beamsplitter to split the FIR beam.

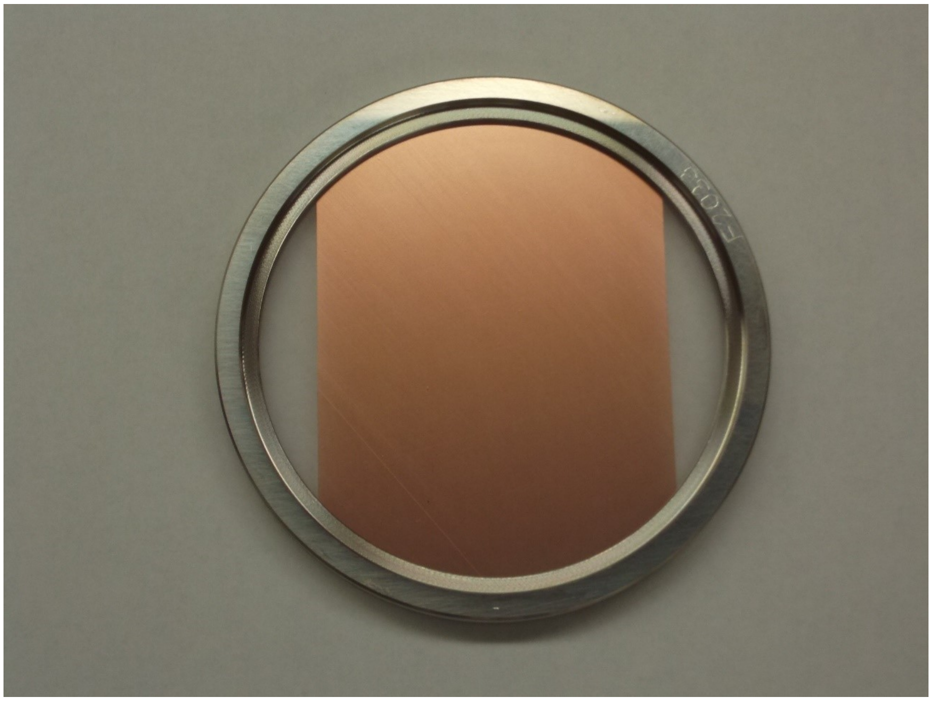

Figure 5.8: Post box beamsplitter.

Ideally, the ”post-box” design for the beamsplitter would allow laser metrology beams to sample the optical path difference of the interferometer without entering the FIR measurement beam. In this way, the metrology beam would not be seen by the FIR detector. However, the hot press process that bonded the individual layers that make up the beamsplitter was found to leave fine striations in the surface of the polypropylene that result in diffraction of the metrology beam into the science beam and did not produce reliable metrology fringes (Figure 5.9).

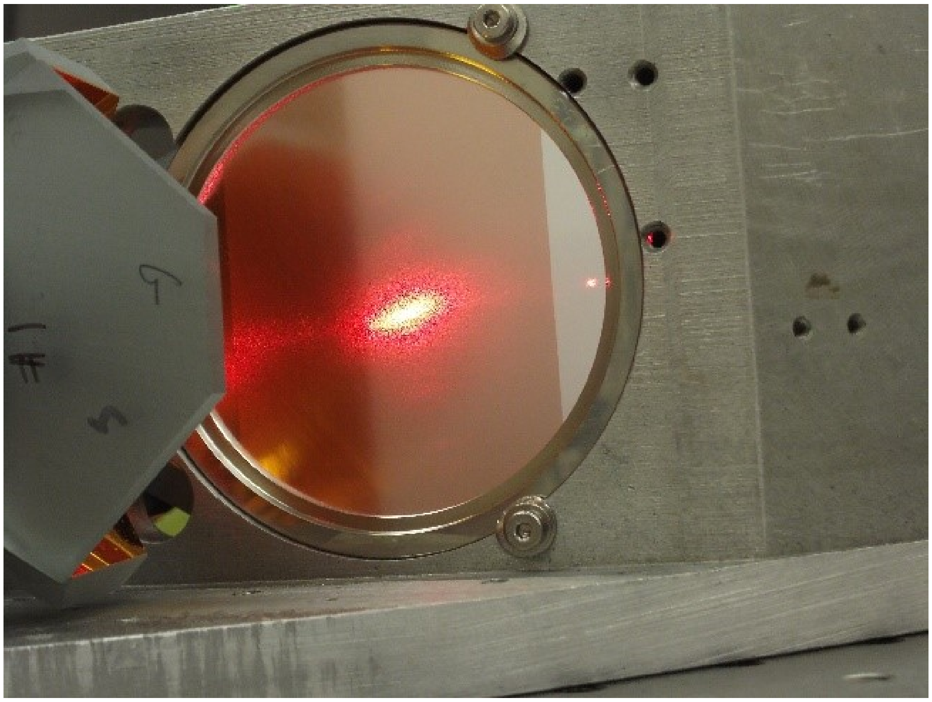

Figure 5.9: The diffraction of the metrology beam into the science beam. The red laser beam can be seen entering the WBI in the transparent region on the right. The diffuse spot in the center of the beamsplitter shows the scattering of the metrology beam after entering the WBI.

5.1.5 Corner Cube Retroflectors

The ABB FTS utilized two 2.5$''$ clear aperture, gold coated corner cube retroflectors. These corner cubes mounted on the FTS arm with epoxy joints to an aluminum frame. The type of epoxy was unknown, being a proprietary substance, but was not silicon based, meaning it was likely a low expansion type of epoxy. The corner cubes became detached from the frame after thermal cycling (Figure 5.10), likely due to the large differential thermal contraction between aluminum and the epoxy (Appendix A).

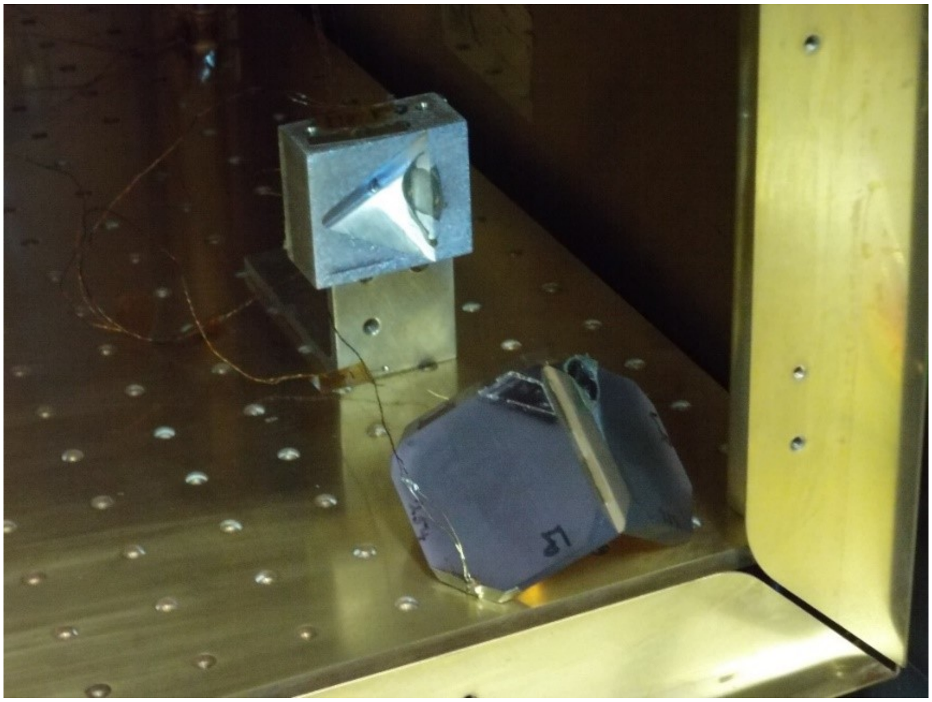

Figure 5.10: The original corner cube retroreflectors from the WBI after thermal cycling. The dislocation is due to the differential thermal expansion of the aluminum frame and the glass mirror.

As a solution to the thermal contraction issue, corner cube retroflectors were purchased with an Invar support frame (Figure 5.11). Through the process of thermal cycling and measuring the orthogonality of the mirrors with a PLX electronic autocollimator, we determined these corner cubes were suitable for both room temperature and cryogenic temperature operation.

5.1.6 Flexure Pivots

The interferometer moving mechanism consisted of a voice coil driven rotating arm attached to the interferometer frame by thin, metal flexure bearings. The original flexure bearing was fabricated from a 250 μm thick plate of spring steel. The mechanical properties of the steel at low temperatures was unknown because the alloy was not specific in the manufacturer specifications. Many steel alloys are known to become brittle and have reduced fracture toughness at low temperatures, due to their b.c.c crystal structure (Section 2.5).

Figure 5.11: Replacement corner cube retroreflectors with Invar frame. These corner cubes were tested at 4 K and maintained alignment both while cold and on return to room temperature.

Therefore, the flexure bearings were replaced with Inconel 718 [78]. Inconel retains its ductility over the cryogenic temperature range, and has a space heritage, being used in flexure bearings for the cryogenic HIFI instrument on the Herschel Space Observatory [79]. In addition, thinner bearings were considered in order to minimize the force requirements of the voice coil, minimizing the heat dissipation. However, since the flexure bearings were the only connection between the wishbone arm and the FTS frame, they provided the only thermal path through which to cool the arm. The installation of thinner arms significantly decreased the heat flow between the two components.

After the corner-cubes, beamsplitter, and voice coil actuator were removed from the FTS, the thermal map of the skeletal frame of the WBI along with wishbone arm was measured in the Test Facility Cryostat. The thermal conduction was measured for Inconel 718 flexures of two different thicknesses, as well as the original spring steel flexures:

- Stainless steel: thickness = 0.25 mm

- Inconel 718: thickness = 0.13 mm
- Inconel 718: thickness = 0.42 mm

Nine temperature sensors were placed at various locations on the FTS frame and arm to determine the temperature variation across the system Five sensors were placed along the WBI arm, to measure any temperature variation across the arm. The other four sensors were placed around the WBI frame.

Figure 5.12 shows typical cooldown curves when a wishbone arm was connected to its frame using the stainless steel flexures. The Test Facility Cryostat was precooled with liquid nitrogen for 4 hours and the 4 K plate reached its base temperature after 17 hours. The wishbone interferometer frame reached 10 K at approximately the same time, but took another 6 hours to reach base temperature. The wishbone arm connected by the flexure bearings required an additional 10.5 hours. The temperature across the wishbone arm was uniform to within $\sim$1 K, so the 5 sensors on the arm were all shown as the red curve. Table 5.2 shows the time to cool for the other two tests with the Inconel 718 flexures. Te reduce the cooldown time of the WBI arm, an OFHC copper braid was mounted between the frame and arm of the WBI, at the fulcrum to minimize additional torque, as shown in Figure 5.13. The cooldown time was reduced from 50 hours to 32 hours, with no noticeable difference in the current drive requirements. The cooling curves of the WBI arm for each flexure bearing, and, furthermore, with a 10 AWG, 10 cm long, OFHC copper braid across the pivot joint for the thinnest Inconel flexures, are shown in Figure 5.14. The inclusion of the OFHC copper braid sufficiently reduced the cooldown time of the WBI arm with the use of 0.13 mm Inconel flexure bearings, making the use of these thin flexures feasible.

5.1.7 Metrology

The metrology system is used to record interferogram samples in equal intervals of optical path difference of the wishbone interferometer. A 1.55 μm fibre launched, laser based, infrared metrology system was developed for use at cryogenic temperatures. The

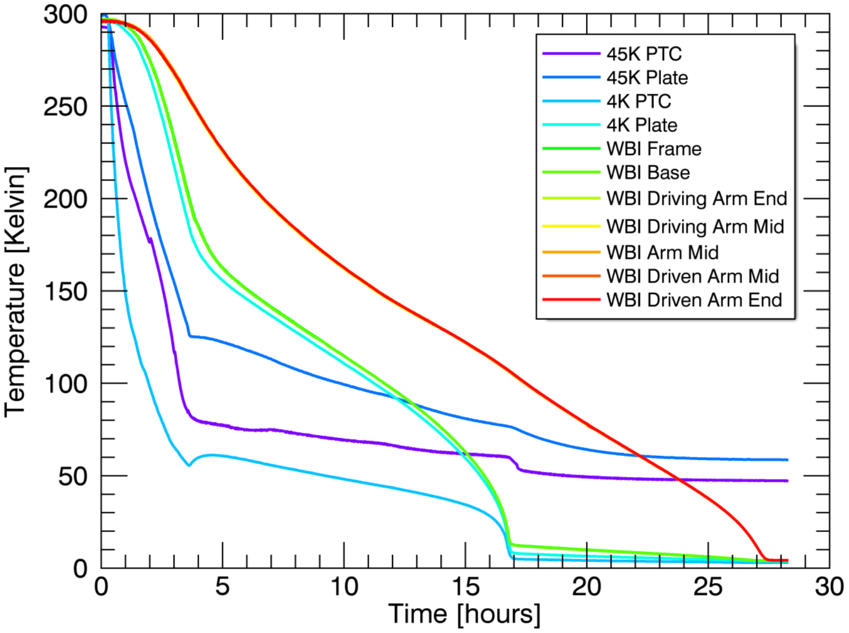

Figure 5.12: Cooldown curves for components of the TFC and WBI during thermal mapping of the FTS. The thermometers on the WBI arm remained within 1 K for the entire cooldown, and are therefore not distinguishable in the figure. Uncertainty in the thermometer readings were approximately 2% of the recorded value.

Table 5.2: Cooling times of the 4 K plate and wishbone interferometer components with different flexure pivots. The reason for the different times to achieve the base temperature of 4 K is because of the different liquid nitrogen precool times.

	Cooling Time (hrs)		
Flexure Type	4 K Plate	WBI frame	WBI arm
Stainless Steel	20.5	24	24.6
Inconel 718 (0.13 mm)	18	45	50.5
Inconel 718 (0.42 mm)	17	23	27.5

Figure 5.13: Flexible copper braid attached to pivot of the wishbone arm to aid cooling the arm.

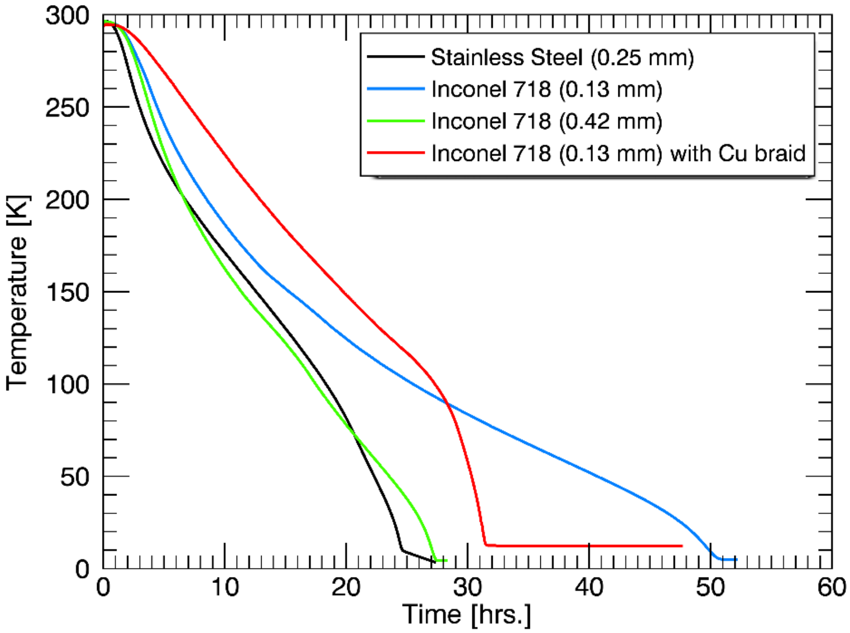

Figure 5.14: Temperature of the WBI arm during cooling. Nominal cooling time for the 4 K volume is 23 hours. Uncertainty in the thermometer readings were approximately 2% of the recorded value.

laser itself will not operate at cryogenic temperatures, and, therefore, will be mounted in the room temperature, upper plate of the TFC. The metrology beam will be fed into the cryogenic volume by a fibre with a low coefficient of thermal expansion, and a low thermal conductivity.

Figure 5.15 shows the IR laser launched using an optical fiber into the interferometer module. A plane mirror was mounted on the piezo-electric translation mechanism oscillating at a frequency of 10 Hz.

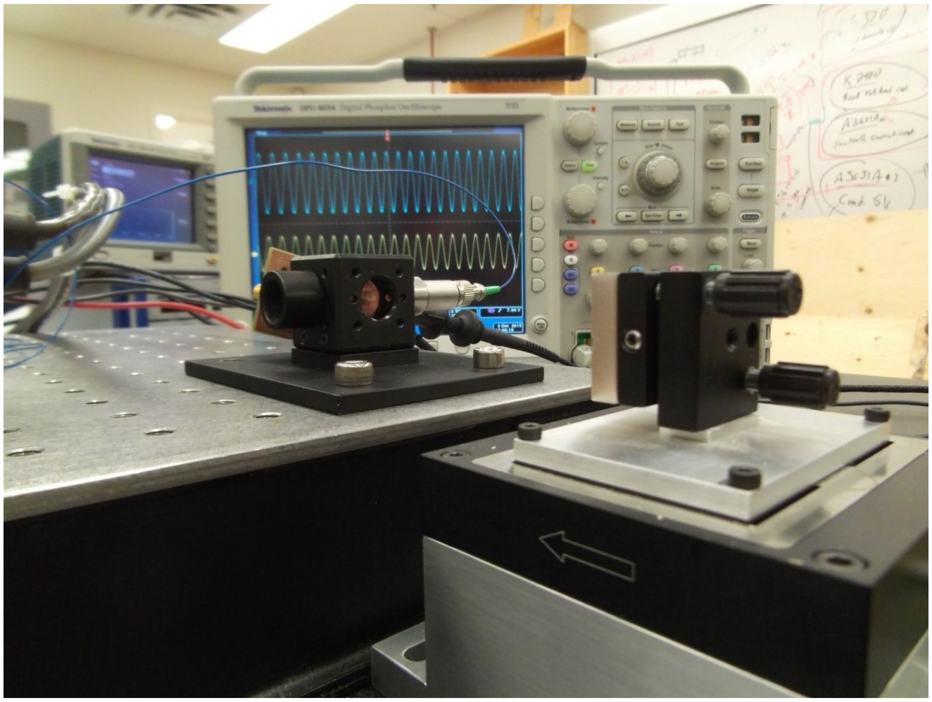

Figure 5.15: IR metrology system shown on an optical bench for testing. Fringes on the oscilloscope are the result of modulating the path difference by translating a reflecting mirror.

IR metrology could not be completed with the post-box beamsplitter due to scattering of the metrology beam. However, we constructed a Mylar™ beamsplitter which reflected an appreciable fraction of a metrology beam from a single mode HeNe laser, in order to test the metrology (Figure 5.16). We were able to observe weak interference fringes using this beamsplitter and the HeNe laser source, shown in Figure 5.17.

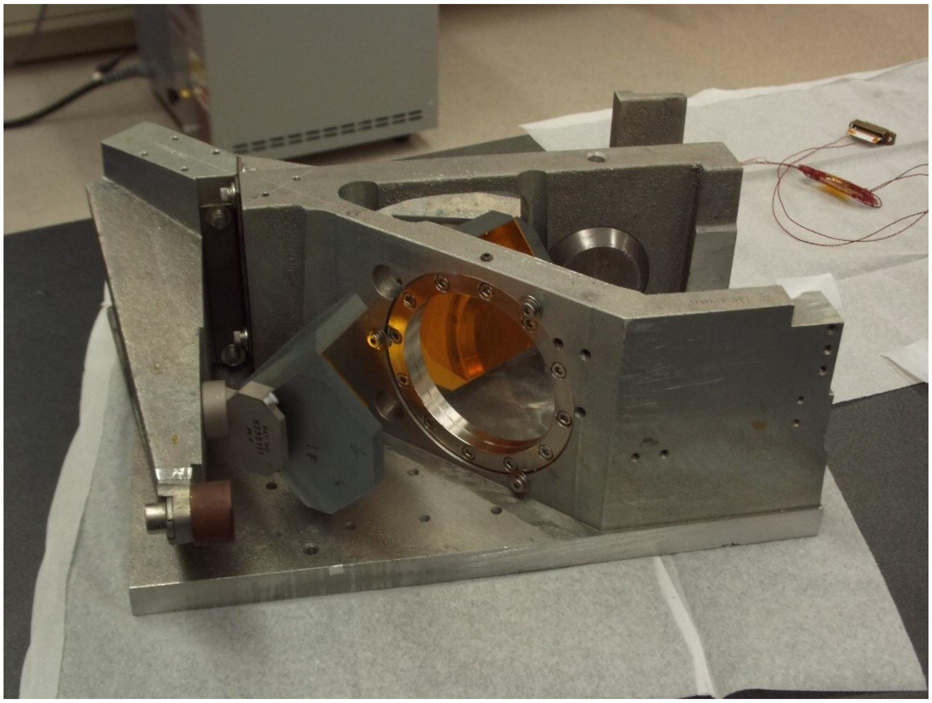

Figure 5.16: Image of the wishbone interferometer with a Mylar beamsplitter.

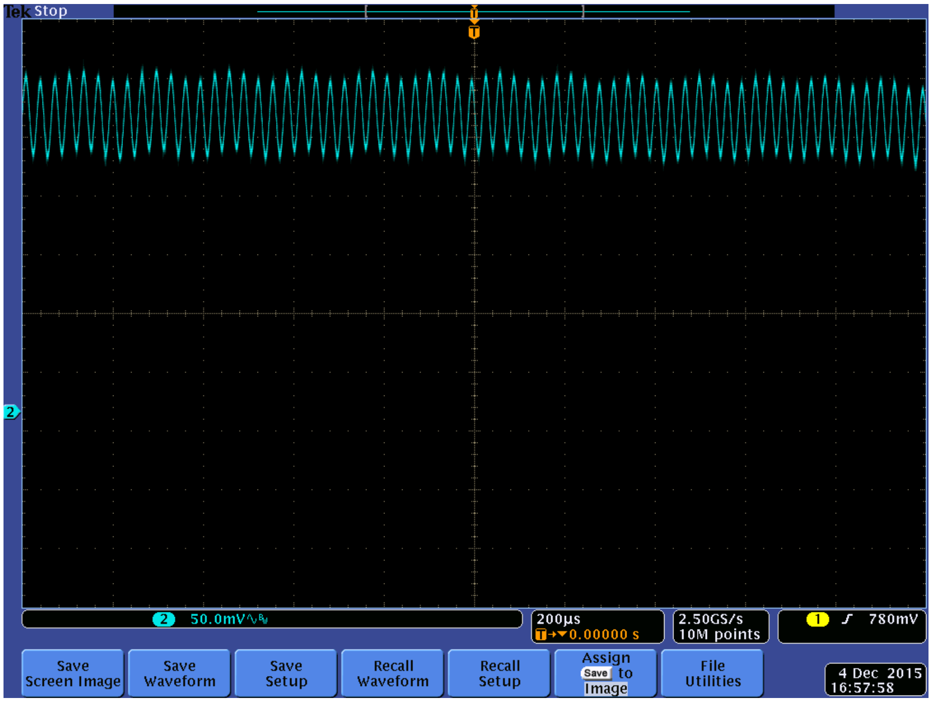

Figure 5.17: Interference fringes observed with a HeNe laser through the Mylar beamsplitter in the wishbone FTS. The scanning frequency of the FTS was 2 Hz.

5.1.8 Cryogenic Black Body Source

In the final design of the cryogenic FTS, the instrument will operate in a light-tight enclosure at ∼4 K. This operational requirement necessitates the use of an internal calibration source. A cryogenic blackbody source similar to that used on the Herschel/SPIRE instrument (SCAL) will be constructed [15]. The goal is to be able to distinguish spectral features at low to intermediate resolution. By placing an unresolved source containing subcomponents of different temperatures at a pupil of the instrument, a complex continuum spectrum can be generated. Figure 5.18 shows a simulation of the spectrum produced from a proposed design of a three component blackbody.

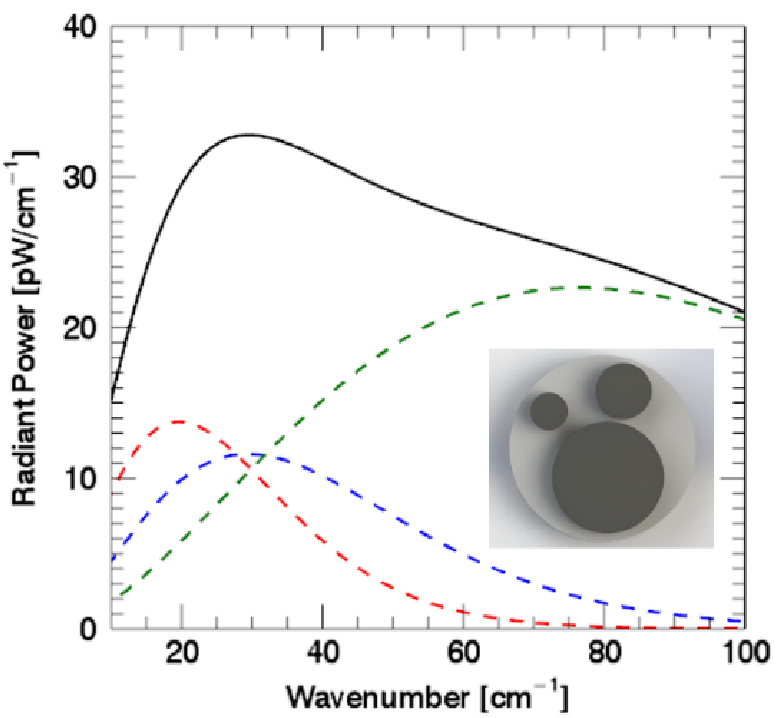

Figure 5.18: A simulation of the spectrum produced by a cryogenic blackbody source with 3 isolated sources. Diameters of the subcomponents are 1 mm, 2 mm, and 6 mm and temperatures are 10 K, 15 K and 40 K respectively.

5.1.9 Millikelvin Bolometers

The test facility cryostat was built with the option to install an adsorption fridge within the 4 K volume for a sub-Kelvin environment. The refrigeration unit selected is a He-10 unit from Chase Research Cryogenics LTD [35]. The system operates with three adsorption pumps, two using ^{3}He and one using ^{4}He. The system can sustain a temperature of 300 mK with a heat load of 3 μW, making it suitable for operation of semiconducting bolometers. Superconducting or hot electron bolometers which operate at 4 K may also be chosen. The selection of a suitable detector for the demonstrator FTS has not been finalized yet. However, with a sub-Kelvin refrigerator, a wide selection of detectors of various sensitivities are available.

5.2 Conclusion

The development of a cryogenic FTS based on a pivoting wishbone arm is still in progress, as shown by unmarked sections in Table 5.1. The voice coil driver, flexure bearings, and corner cube mirrors have been tested and modified as required in order to ensure their functionality at cryogenic temperatures. The design of the beamsplitter and metrology system have been selected and finalized. However, the implementation of these systems is dependent on the fabrication of a beamsplitter with sufficiently small scattering of the metrology beam. A design for the blackbody source has been proposed and a suitable cryogenic detector will be selected. The next steps towards the construction of the cryogenic FTS will be to reproduce the post-box beamsplitter, construct the blackbody source, install the selected cryogenic detector, and install a fibre fed laser in the TFC for metrology. Also, upon completion of the system, a second voice coil driver may be added to provide suitable dampening of WBI arm oscillations in order to make the system capable of performing step and integrate measurements. This work will be completed as part of my future PhD thesis. The expected performance of the cryogenic FTS once completed is given in Table 5.3

Table 5.3: Expected specifications of the cryogenic FTS.

Parameter	Expected Performance
Spectral Range	5-500 cm^{-1} with resonant mesh beamsplitter
Spectral Resolution	<1 cm^{-1}
Beam Diameter	50 mm
Optical Scan Length	0.5 cm before and after ZPD
Scan Time	$\sim$1 s
Source	Internal cryogenic blackbody
Focussing optics f/#	f/3, f/2
Mirror Diameter	50 mm

Bibliography

[1] Michael G. Hauser and Eli Dwek. The cosmic infrared background: Measurements and implications. *Annual Review of Astronomy and Astrophysics*, 39(1):249–307, 2001.

[2] Peter H Siegel et al. Terahertz technology. *IEEE Transactions on microwave theory and techniques*, 50(3):910–928, 2002.

[3] Infrared Processing and Analysis Center (ipac). Infrared Windows. `http://www.ipac.caltech.edu/outreach/Edu/Windows/irwindows.html`, 2015. [Online; accessed 23 December 2015].

[4] Grace Trimboli. Development of a near-field terahertz microscope for breast cancer diagnostics. Master's thesis, University of Lethbridge, 2015.

[5] Thomas G Phillips and Jocelyn Keene. Submillimeter astronomy [heterodyne spectroscopy]. *Proceedings of the IEEE*, 80(11):1662–1678, 1992.

[6] David Leisawitz, William Danchi, Michael DiPirro, Lee D Feinberg, Dan Gezari, Michael Hagopian, John C Mather, S Harvey Moseley Jr, Robert F Silverberg, William D Langer, et al. Far-ir/submillimeter space interferometry: scientific motivation and technology requirements. In *Aerospace Conference, 2001, IEEE Proceedings.*, volume 4, pages 4–1995. IEEE, 2001.

[7] Jeffrey Bennett, Megan Donahue, Nicholas Schneider, and Mark Voit. *The cosmic perspective; 6th ed.* Addison-Welsey, Boston, MA, 2010.

[8] J. H. Jeans. The stability of a spherical nebula. *Philosophical Transactions of the Royal Society of London. Series A, Containing Papers of a Mathematical or Physical Character*, 199:1–53, 1902.

[9] Douglas Scott, Pauline Barmby, Pierre Bastien, Jan Cami, Edward Chapin, James Di Francesco, Michel Fich, Mark Halpern, Martin Houde, Gilles Joncas, et al. The submillimetre universe. *arXiv preprint arXiv:1008.4159*, 2010.

[10] M. J. F. Rosenberg, P. P. van der Werf, S. Aalto, L. Armus, V. Charmandaris, T. Daz-Santos, A. S. Evans, J. Fischer, Y. Gao, E. Gonzlez-Alfonso, T. R. Greve, A. I. Harris, C. Henkel, F. P. Israel, K. G. Isaak, C. Kramer, R. Meijerink, D. A. Naylor, D. B. Sanders, H. A. Smith, M. Spaans, L. Spinoglio, G. J. Stacey, I. Veenendaal, S. Veilleux, F. Walter, A. Wei, M. C. Wiedner, M. H. D. van der Wiel, and E. M. Xilouris. The Herschel Comprehensive (U)LIRG Emission Survey (HERCULES):

CO Ladders, Fine Structure Lines, and Neutral Gas Cooling. *The Astrophysical Journal*, 801(2):72, 2015.

[11] E. Hecht. *Optics*. Pearson education. Addison-Wesley, 2002.

[12] MF Kessler, JA Steinz, ME Anderegg, J Clavel, G Drechsel, P Estaria, J Faelker, JR Riedinger, A Robson, BG Taylor, et al. The infrared space observatory (iso) mission. *Astronomy and Astrophysics*, 315:L27–L31, 1996.

[13] M. W. Werner, T. L. Roellig, F. J. Low, G. H. Rieke, M. Rieke, W. F. Hoffmann, E. Young, J. R. Houck, B. Brandl, G. G. Fazio, and others. The spitzer space telescope mission. *The Astrophysical Journal Supplement Series*, 154(1):1, 2004.

[14] Hiroshi Murakami, Hajime Baba, Peter Barthel, David L. Clements, Martin Cohen, Yasuo Doi, Keigo Enya, Elysandra Figueredo, Naofumi Fujishiro, Hideaki Fujiwara, and others. The infrared astronomical mission AKARI. *Publications of the Astronomical Society of Japan*, 59(sp2):S369–S376, 2007.

[15] GL Pilbratt, JR Riedinger, T Passvogel, G Crone, D Doyle, U Gageur, AM Heras, C Jewell, L Metcalfe, S Ott, et al. Herschel space observatory-an esa facility for far-infrared and submillimetre astronomy. *Astronomy & Astrophysics*, 518:L1, 2010.

[16] P Murdin. James clerk maxwell telescope. *Encyclopedia of Astronomy and Astrophysics*, 1:4223, 2000.

[17] E. T. Young, E. E. Becklin, P. M. Marcum, T. L. Roellig, J. M. De Buizer, T. L. Herter, R. Gsten, E. W. Dunham, P. Temi, B.-G. Andersson, and others. Early science with SOFIA, the stratospheric observatory for infrared astronomy. *The Astrophysical Journal Letters*, 749(2):L17, 2012.

[18] Bruce Swinyard and Takao Nakagawa. The space infrared telescope for cosmology and astrophysics: Spica a joint mission between jaxa and esa. *Experimental Astronomy*, 23(1):193–219, 2009.

[19] Takao Nakagawa, Hideo Matsuhara, and Yasuhiro Kawakatsu. The next-generation infrared space telescope spica. In *SPIE Astronomical Telescopes+ Instrumentation*, pages 84420O–84420O. International Society for Optics and Photonics, 2012.

[20] G Neugebauer, HJ Habing, R Van Duinen, HH Aumann, B Baud, CA Beichman, DA Beintema, N Boggess, PE Clegg, T De Jong, et al. The infrared astronomical satellite (iras) mission. *The Astrophysical Journal*, 278:L1–L6, 1984.

[21] CM Bradford, PF Goldsmith, A Bolatto, L Armus, J Bauer, P Appleton, A Cooray, C Casey, D Dale, B Uzgil, et al. A cryogenic space telescope for far-infrared astrophysics: A vision for nasa in the 2020 decade. *arXiv preprint arXiv:1505.05551*, 2015.

[22] SPICA: Space Infrared Telescope for Cosmology and Astrophysics. `http://isdc.unige.ch/spica/`, 2015. [Online; accessed 23 December 2015].

[23] Jonathan P Gardner, John C Mather, Mark Clampin, Rene Doyon, Matthew A Greenhouse, Heidi B Hammel, John B Hutchings, Peter Jakobsen, Simon J Lilly, Knox S Long, et al. The james webb space telescope. *Space Science Reviews*, 123(4):485–606, 2006.

[24] J. Ekin. *Experimental Techniques for Low-Temperature Measurements: Cryostat Design, Material Properties and Superconductor Critical-Current Testing*. OUP Oxford, 2006.

[25] Daniel V Schroeder. *An introduction to thermal physics*, volume 60. Addison Wesley New York, 2000.

[26] Harold Max Rosenberg. *Low temperature solid state physics*. Clarendon Press Oxford, 1963.

[27] Laird Kramer and Hugh D. Young. *Sears & Zemansky's University Physics*. Addison-Wesley Longman, Incorporated, New York, 13th edition, 2012.

[28] Charles Kittel. *Introduction to Solid State Physics*. John Wiley & Sons, Inc., New York, 8th edition, 2005.

[29] G. Ventura and M. Perfetti. *Thermal Properties of Solids at Room and Cryogenic Temperatures*. International Cryogenics Monograph Series. Springer Netherlands, 2014.

[30] Neil W. Ashcroft and N. David Mermin. *Solid State Physics*. Brooks/Cole, Cengage Learning, Belmont, CA, 1976.

[31] Guglielmo Ventura and Lara Risegari. *The Art of Cryogenics: Low-Temperature Experimental Techniques*. Elsevier Ltd., Oxford, UK, 1st edition, 2008.

[32] R.P. Reed, A.F. Clark, and American Society for Metals. *Materials at low temperatures*. American Society for Metals, 1983.

[33] By cdang (own work) [gfdl (`http://www.gnu.org/copyleft/fdl.html`) or cc by-sa 3.0 (`http://creativecommons.org/licenses/by-sa/3.0`)], via wikimedia commons, 2015. [Online; accessed 19 December 2015].

[34] Teun C van den Dool, Bob Kruizinga, Ben C Braam, Roger FMM Hamelinck, Nicolas Loix, Dennis Van Loon, and Johan Dams. Spica/safari fourier transform spectrometer mechanism evolutionary design. In *SPIE Astronomical Telescopes+ Instrumentation*, pages 84423R–84423R. International Society for Optics and Photonics, 2012.

[35] Chase Research Cryogenics. `http://www.chasecryogenics.com/index.htm`, 2015. [Online; accessed 05 November 2015].

[36] A. Rogalski. History of infrared detectors. *Opto-Electronics Review*, 20(3):279–308, July 2012.

[37] Darren Hayton. Cryogenic test facility interface control document. Technical report, University of Lethbridge, 2010.

[38] R.G. Budynas, J.K. Nisbett, and J.E. Shigley. *Shigley's mechanical engineering design*. McGraw-Hill series in mechanical engineering. McGraw-Hill, 2008.

[39] *Properties and Selection of Materials*, volume 1 of *Metals Handbook*. ASM International, Materials Park, OH, 8th edition, 1961.

[40] Cryomech. PT415 Pulse Tube Cryocooler. `http://www.cryomech.com/products/cryorefrigerators/pulse-tube/pt415/`, 2015. [Online; accessed 04 November 2015].

[41] A. W. Lawson and Robert Fano. Note on the efficiency of radiation shields. *Review of Scientific Instruments*, 18(10):727–729, 1947.

[42] R Berman and CF Mate. Thermal contact at low temperatures. *Nature*, 182:1661, 1958.

[43] Apiezon. Apiezon N Grease. `http://www.apiezon.com/products/vacuum-greases/n-grease`, 2015. [Online; accessed 05 November 2015].

[44] Gold Plating Services. `http://www.goldplating.com/`, 2015. [Online; accessed 04 November 2015].

[45] P.A. Kohl. Electrodeposition of gold. *Modern Electroplating*, pages 115–130, 2010.

[46] Electrolytics Inc., Faraday's Law. `http://www.electrolytics.org/faradaysLaw.html`, 2015. [Online; accessed 23 December 2015].

[47] M. M. Finckenor and D. Dooling. *Multilayer insulation material guidelines*. National Aeronautics and Space Administration, Marshall Space Flight Center, 1999.

[48] CMR Direct. 12-pair copper loom. `http://www.cmr-direct.com/en/woven-loom/cmr-cwl-12cu`, 2015. [Online; accessed 05 November 2015].

[49] Lake Shore Cryotronics. Cryogenic Temperature Sensors. `http://www.lakeshore.com/products/Cryogenic-Temperature-Sensors/Pages/default.aspx`, 2015. [Online; accessed 02 December 2015].

[50] Lake Shore Cryotronics. Cryogenic Wiring. `http://www.lakeshore.com/products/Cryogenic-Accessories/Wire/pages/Overview.aspx`, 2015. [Online; accessed 13 December 2015].

[51] Lake Shore Cryotronics. Model 340 Cryogenic Temperature Controller. `http://www.lakeshore.com/products/cryogenic-temperature-controllers/model-340/Pages/Overview.aspx`, 2015. [Online; accessed 05 November 2015].

[52] Renishaw. RLD10 Differential Interferometer. `http://www.renishaw.com/en/rld10-differential-interferometer--6492`, 2015. [Online; accessed 05 November 2015].

[53] PLX. ACT-25 Electronic Autocollimator and Alignment Telescope. `http://www.plxinc.com/products/all-in-one-electronic-autocollimator-and-alignment-telescope`, 2015. [Online; accessed 05 November 2015].

[54] DuPont. Kevlar® Fiber. `http://www.dupont.com/products-and-services/fabrics-fibers-nonwovens/fibers/brands/kevlar.html`, 2015. [Online; accessed 02 December 2015].

[55] McMaster-Carr. High-Strength Lightweight Carbon Fiber Tubes. `http://www.mcmaster.com/#standard-carbon-fiber-hollow-tubing/=109maqu`, 2015. [Online; accessed 16 December 2015].

[56] P.K. Mallick. *Fiber-reinforced composites: materials, manufacturing, and design*. Dekker Mechanical Engineering Series. CRC Press, 2008.

[57] RP Reed and M Golda. Cryogenic composite supports: a review of strap and strut properties. *Cryogenics*, 37(5):233–250, 1997.

[58] G. Hartwig and S. Knaak. Fibre-epoxy composites at low temperatures. *Cryogenics*, 24(11):639–647, November 1984.

[59] Morinobu Endo. Structure of mesophase pitch-based carbon fibres. *Journal of Materials Science*, 23(2):598–605, February 1988.

[60] F.C. Campbell. *Structural Composite Materials*. ASM International, 2010.

[61] A. Kelly and W. R. Tyson. Tensile properties of fibre-reinforced metals: Copper/-tungsten and copper/molybdenum. *Journal of the Mechanics and Physics of Solids*, 13(6):329–350, December 1965.

[62] M. El Asloun, J. B. Donnet, G. Guilpain, M. Nardin, and J. Schultz. On the estimation of the tensile strength of carbon fibres at short lengths. *Journal of Materials Science*, 24(10):3504–3510, 1989.

[63] Th Lacroix, B. Tilmans, Roland Keunings, M. Desaeger, and Ignace Verpoest. Modelling of critical fibre length and interfacial debonding in the fragmentation testing of polymer composites. *Composites science and technology*, 43(4):379–387, 1992.

[64] Shao-Yun Fu and Bernd Lauke. Effects of fiber length and fiber orientation distributions on the tensile strength of short-fiber-reinforced polymers. *Composites Science and Technology*, 56(10):1179–1190, 1996.

[65] H Bansemir and O Haider. Fibre composite structures for space applicationsrecent and future developments. *Cryogenics*, 38(1):51–59, January 1998.

[66] PC McDonald, E Jaramillo, and B Baudouy. Thermal design of the cfrp support struts for the spatial framework of the herschel space observatory. *Cryogenics*, 46(4):298–304, 2006.

[67] Takashi Onaka, Takao Nakagawa, Toshio Matsumoto, Hiroshi Murakami, Hideo Matsuhara, Hirokazu Kataza, Hidehiro Kaneda, Keigo Enya, Yukari Y. Yui, and Motohide Tamura. Telescope system of the Space Infrared Telescope for Cosmology and Astrophysics (SPICA) mission. In *5th International Conference on Space Optics*, volume 554, pages 297–302, 2004.

[68] Abdel A. Abusafieh, Dan R. Federico, Steven J. Connell, Eri J. Cohen, and Paul B. Willis. Dimensional stability of CFRP composites for space-based reflectors. In *International Symposium on Optical Science and Technology*, pages 9–16. International Society for Optics and Photonics, 2001.

[69] J. Guthrie, T.B. Tolle, and D.H. Rose. Composites for orbiting platforms. In *AMPTIAC Quarterly*, volume 8, pages 51–58. AMMTIAC, 2004.

[70] European Union Seventh Framework Programme. Far Infrared Space Interferometer Critical Assessment. `http://www.fp7-fisica.eu/`, 2015. [Online; accessed 15 December 2015].

[71] J. Fraden. *Handbook of Modern Sensors: Physics, Designs, and Applications*. Springer New York, 2010.

[72] JD James, JA Spittle, SGR Brown, and RW Evans. A review of measurement techniques for the thermal expansion coefficient of metals and alloys at elevated temperatures. *Measurement Science and Technology*, 12(3):R1, 2001.

[73] Francois P Pajot, Bruno Maffei, Dominic J Benford, Dale J Fixsen, Sébastien Lefranc, S Harvey Moseley, Cyrille Rioux, Rick A Shafer, Gaurav J Shah, and Johannes G Staguhn. Design and performances of a cryogenic fabry-perot for submillimeter astronomy. In *Optical Science and Technology, SPIE's 48th Annual Meeting*, pages 13–20. International Society for Optics and Photonics, 2003.

[74] PJRC. Teensy++ 2.0. `https://www.pjrc.com/teensy/index.html`, 2015. [Online; accessed 02 December 2015].

[75] SolidWorks. `http://www.solidworks.com/`, 2015. [Online; accessed 23 December 2015].

[76] Phytron. Stepper Motors VSS UHVC (Cryo). `http://www.phytron-elektronik.de/antrieb/index.php?Set_ID=160&PID=38`, 2015. [Online; accessed 02 December 2015].

[77] NIST. Cryogenic Material Properties Database. `http://cryogenics.nist.gov/MPropsMAY/materialproperties.htm`, 2015. [Online; accessed 02 December 2015].

[78] American Special Metals, Inconel Alloy 718. `http://www.americanspecialmetals.com/inconelalloy718.html`, 2015. [Online; accessed 23 December 2015].

[79] R. Huisman, J. W. G. Aalders, M. J. Eggens, J. Evers, H. M. Jacobs, B. J. van Leeuwen, A. C. T. Nieuwenhuizen, G. R. Ploeger, K. J. Wildeman, B. Jayawardhana, and J. M. A. Scherpen. Cryogenic mechatronic design of the HIFI Focal Plane Chopper. *Mechatronics*, 21(8):1259–1271, December 2011.

Appendix A

Material Properties

To provide a useful reference, I have gathered together an appendix of properties for those materials which have been used or considered throughout the thesis. Except where explicitly stated, all values are taken from [24].

Table A.1: Specific heat capacity, c_P [J g^{-1} K^{-1}], of common cryogenic materials used in this thesis.

Material	4 K	10 K	20 K	30 K	50 K	77 K	100 K	150 K	200 K	300 K
Aluminum	0.00026	0.00140	0.0089	0.032	0.142	0.336	0.481	0.684	0.797	0.902
Copper	0.00009	0.00088	0.0070	0.027	0.097	0.192	0.252	0.323	0.356	0.386
Al 6061-T6	0.00029	0.00157	0.0089	0.033	0.149	0.348	0.492	0.713	0.835	0.954
Stainless steel	0.0017	0.0047	0.016	0.01	0.10	0.20	0.25	0.35	0.40	0.48
Inconel	–	–	–	–	–	0.275	0.291	0.334	0.369	0.427
G-10CR	0.0020	0.0154	0.047	0.081	0.149	0.239	0.317	0.489	0.664	0.999
Polyimide (Kapton$^{\text{TM}}$)	0.00079	0.0117	0.0579	0.116	0.224	0.338	0.414	0.537	0.627	0.755
Apiezon N$^{\text{TM}}$	0.00203	0.0243	0.0925	0.172	0.332	0.522	0.657	0.913	1.201	-

Table A.2: Thermal expansion of materials which are commonly used in cryogenics. Below room temperature, thermal expansion is expressed as a percentage change in dimensions. Above room temperature, it is expressed as the coefficient of thermal expansion, α

Material	4 K [%]	40 K [%]	77 K [%]	100 K [%]	150 K [%]	200 K [%]	250 K [%]	α at 293 K [$10^{-6}\,\mathrm{K}^{-1}$]
Aluminum	0.415	0.413	0.393	0.370	0.295	0.201	0.097	23.1
Copper	0.324	0.322	0.302	0.282	0.221	0.148	0.070	11.6
Al 6061-T6	0.414	0.412	0.389	0.365	0.295	0.203	0.097	22.5
Gold	0.324	0.313	0.281	0.256	0.195	0.129	0.061	14.1
Inconel 718	0.238	0.236	0.224	0.211	0.167	0.114	0.055	13.0
Invar	–	0.04	0.038	0.036	0.025	0.016	0.009	3.0
Stainless steel 304	0.296	0.296	0.281	0.261	0.206	0.139	0.066	15.1
Stainless steel 316	0.297	0.296	0.279	0.259	0.201	0.136	0.065	15.2
Epoxy	1.16	1.11	1.028	0.959	0.778	0.550	0.277	66
Polyimide (Kapton™)	0.44	0.44	0.43	0.41	0.36	0.29	0.16	46
G-10CR (parallel to fibres)	0.241	0.234	0.213	0.197	0.157	0.108	0.052	12.5
G-10CR (normal)	0.706	0.690	0.642	0.603	0.491	0.346	0.171	41

Table A.3: Electrical Resistivity of common cryogenic materials. For pure metals, resistivity at cryogenic temperatures is largely dependent on sample purity. Therefore, the ideal electrical resistivity is shown, by subtracting the residual resistivity. Residual resistivity, $\rho_{res} \approx \rho_{4\,\mathrm{K}}$, can be found by dividing room temperature resistivity by the RRR. Resitivity is measured in $\mu\Omega$cm

Material	10 K	20 K	50 K	77 K	100 K	150 K	200 K	250 K	295 K
Aluminum (RRR = 3500)	-	0.0007	0.047	0.22	0.44	1.01	1.59	2.28	2.68
Copper (RRR = 3400)	-	0.001	0.049	0.19	0.34	0.70	1.05	1.38	1.69
Gold (RRR = 300)	0.0006	0.012	0.20	0.42	0.62	1.03	1.44	1.92	2.20
Al 6061-T6	1.38	1.39	1.48	1.67	1.88	2.46	3.09	3.68	4.19
Inconel 718	108	108	108	109	–	–	114	134	156
Beryllium Copper	6.92	6.92	7.04	7.25	7.46	7.96	8.48	8.98	9.43
Phosphor Bronze	8.58	8.58	8.69	8.89	9.07	9.48	9.89	10.3	10.7
Stainless Steel 304	49.5	49.4	50.0	51.5	53.3	58.4	63.8	68.4	72.3
Stainless Steel 316	53.9	53.9	54.9	56.8	58.8	63.8	68.9	73.3	77.1
Invar	50.3	50.5	52.1	54.5	57.0	63.3	70.0	76.5	82.3

Table A.4: Thermal conductivity of common cryogenic materials. Units are W m^{-1} K^{-1}.

Material	4 K	10 K	20 K	40 K	77 K	100 K	150 K	200 K	295 K
Al-6061-T6	5.3	14	28	52	84	98	120	136	155
Beryllium-Copper	1.9	5.0	11	21	36	43	57	72	95
Copper OFHC (RRR = 100)	630	1540	2430	1470	544	461	418	407	397
Inconel 718	0.46	1.5	3.0	4.7	6.4	7.1	8.1	8.7	9.7
Invar	0.24	0.73	1.7	2.6	4.2	6.2	7.6	10	12
Stainless steel 304, 316	0.27	0.90	2.2	4.7	7.9	9.2	11	13	15
G-10CR (Normal)	0.072	0.11	0.16	0.22	0.28	0.31	0.37	0.45	0.60
G-10CR (Warp)	0.073	0.14	0.20	0.27	0.39	0.45	0.57	0.67	0.86
Polyimide (Kapton™)	0.011	0.024	0.048	0.083	0.13	0.14	0.16	0.18	0.19
Polyethylene terepthalate (Mylar™)	0.038	0.048	0.083	0.096	0.12	–	–	–	–

Table A.5: Mechanical properties of common cryogenic materials.

Material	Density [g cm^{-3}]	Young's Modulus [GPa]	Shear Modulus [GPa]	Poisson's Ratio	Yield Strength [MPa]
Stainless Steel 304	7.86	200	77.3	0.290	240
Stainless Steel 316	7.97	195	75.2	0.294	240
Al 1100-0	2.75	69	–	–	¡35
Al 6061-T87 (Precipitation Hardened)	2.70	70.1	26.4	0.338	275
Copper OFHC	8.95	117	–	–	70
Beryllium Copper Cu-2%Be (UNS C17200)	8.23	119	–	–	1030
Inconel 718	8.20	200	–	–	1060
G-10 fiberglass	1.65	28	–	–	–
Kapton™	1.43	3.4	–	–	210
Mylar™	1.38	3.8	–	–	70

Appendix B

Test Facility Cryostat Wiring

Figure B.1: Block diagram of wiring for the Test Facility Cryostat.

Appendix C

Renishaw Differential Interferometer Interface

As outlined in Chapter 4, the differential interferometer (DI) as delivered only allowed the collection of displacement data for 20 s. Since our use of the DI required data collection for a series of hours, we designed our own control circuit and software for the interferometer. Here we outline the design of the interface and data logger electronics for the Renishaw differential interferometer (DI) readout. The electronics features two Teensy++2.0 microcontrollers [74]. A single controller is dedicated to reading the 36 bit output from the RDI module, the second controller is configured for remote operation of momentary switches to reset the RDI module and for generating a clock pulse to trigger reading RDI output. This controller is referred to as the ”master,” since it communicates with the PC serial port and sends commands to the other controller, referred to as the ”slave.” The slave controller transmits over the serial port, but does not receive, allowing for faster collection and transmission of data over the port.

The clock chip is a variable DS32KHz crystal clock, which is controlled via 16 pins from the master controller. A 16 bit counter module is also included in the electronics which increments with every clock pulse. Since the DI provides a relative measurement, and data readings are not individually time stamped, if the data receiver misses a clock pulse, the rest of the data set is compromised. The counter triggers an overflow error if the count on any read cycle does not increase incrementally.

A signal strength monitor iss also incorporated into the output of the master controller. This max 1 V DC signal can be measured by a BNC connection to a voltmeter or passed through an ADC to be measured by the PC control software(Figure C.1). The signal strength indicates whether the DI was in alignment. In practice, a 1 V is never achieved because of Fresnel reflection losses when passing the laser through the fused silica viewport window in the TFC.

The circuit was designed and fabricated by Greg Tompkins and Vince Weiler, members of the AIG.

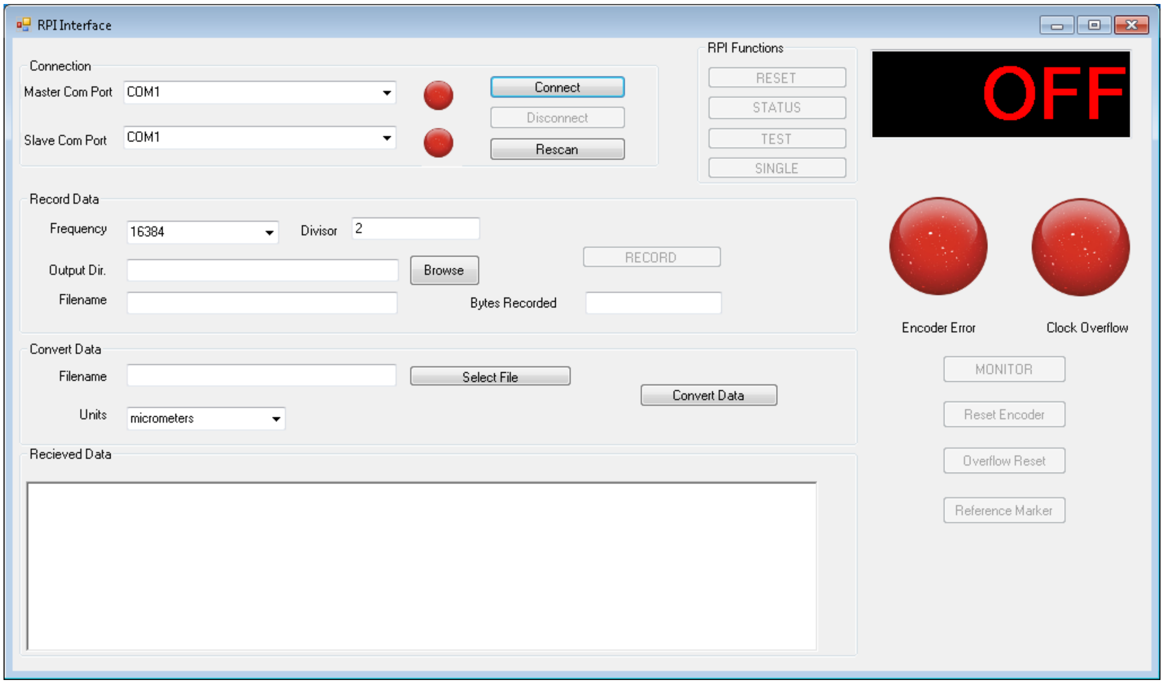

Master Com Port COM1

Slave Com Port COM1

Frequency 16384

Divisor 2

Units micrometers

Figure C.1: The graphical user interface (GUI) used to set the recording frequency, reset the Renishaw DI and laser unit, and record displacement data from the DI. Software was written in Visual Basic by Vince Weiler.

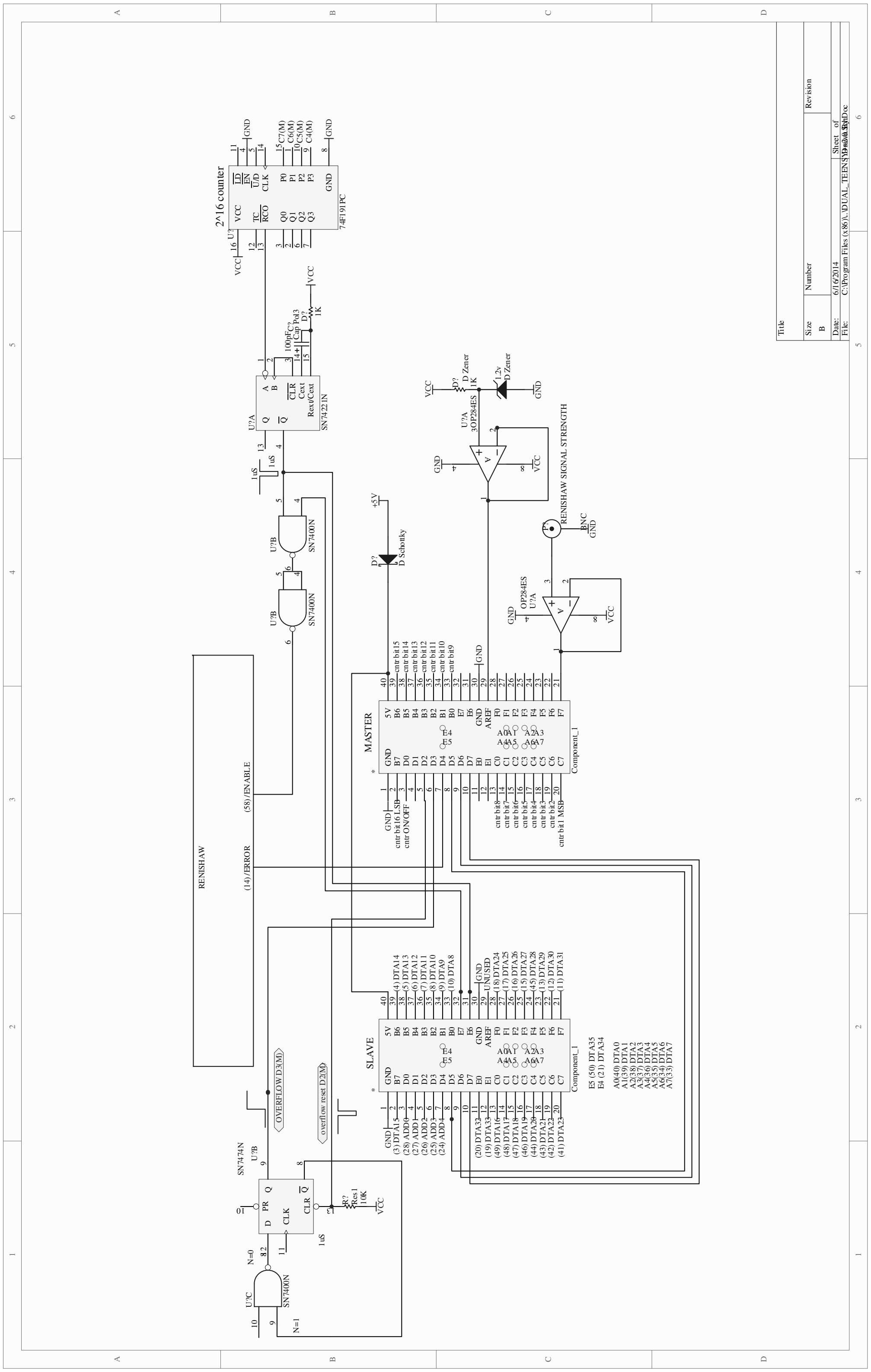

Figure C.2: The circuit diagram for the dual Teensy module to interface between the Renishaw RPI20 module and a PC.

Appendix D

Initial Design of TFC

Design of a cryogenic test facility for evaluating the performance of interferometric components of the SPICA/SAFARI instrument

Ian T. Veenendaal*, David A. Naylor, Brad G. Gom
Institute for Space Imaging Science, Department of Physics and Astronomy, University of Lethbridge, 4401 University Drive W., Lethbridge, Alberta, Canada T1K 3M4

ABSTRACT

The Japanese SPace Infrared telescope for Cosmology and Astrophysics (SPICA), a 3 m class telescope cooled to ~ 6 K, will provide extremely low thermal background far-infrared observations. An imaging Fourier transform spectrometer (SAFARI) is being developed to exploit the low background provided by SPICA. Evaluating the performance of the interferometer translation stage and key optical components requires a cryogenic test facility. In this paper we discuss the design challenges of a pulse tube cooled cryogenic test facility that is under development for this purpose. We present the design of the cryostat and preliminary results from component characterization and external optical metrology.

Keywords: SPICA, SAFARI, test cryostat, Fourier transform spectrometer, characterization

1. INTRODUCTION

The Space Infrared telescope for Cosmology and Astrophysics (SPICA[1]) is an international space project lead by the Japanese Space Agency (JAXA) and is designed to build on the success of Herschel. The telescope is similar in design and function to the Herschel observatory[2] but will feature some major improvements. Herschel was itself an infrared space observatory that demonstrated a major advancement in sensitivity and spatial resolution compared to previous FIR space observatories. The Herschel telescope was passively cooled; reaching an operational temperature of ~ 85 K.[2] This temperature still represented a larger radiant flux than most objects in the universe. SPICA is designed with the intent to look further into the universe to gain a better understanding of the formation and evolution of galaxies, stars and planets, and will therefore require a dramatic increase in sensitivity, which will be achieved by employing an active cooling system to cool the primary mirror to 6 K. The thermal emission of the SPICA telescope optics will be about six orders of magnitude less than Herschel, allowing SPICA to peer further into the universe without being blinded by thermal emission from the telescope.[3]

1.1 SAFARI overview

The SpicA FAR infrared Instrument (SAFARI[3]) is a far-infrared imaging spectrometer proposed for SPICA that will utilize the extremely low thermal background to provide astronomers with highly sensitive, highly spatially resolved spectral data of the universe in the 34-200 μm range. SAFARI will boast a much higher spatial resolving power compared to the SPIRE instrument on Herschel, and a larger projected field of view (2'×2' compared to 50"x50")[3]. In line with the operating requirements of the telescope, the optical components of SAFARI will be designed to function near 4 K. This presents many engineering challenges in the design of the instrument. The instrument will consist of a Mach-Zehnder imaging Fourier transform spectrometer (FTS) which will need to be cooled to 4 K while maintaining optical alignment. Additionally, the electronics controlling the translation mechanism for the optical delay line must dissipate very little power in order to meet the stringent thermal requirements of the spacecraft. To this end, the translation mechanism design will be heavily influenced by the translation mechanism design for the DARWIN mission, a system of magnetic bearings which dissipates little heat and provides high precision mirror movement and metrology.[4]

2. CRYOSTAT DESIGN

In order to test the translation stage and key components of the FTS optics under normal operating conditions a cryogenic test facility is required. There are design challenges in the construction of this facility related to the large

---

* ian.veenendaal@uleth.ca

volume and large cooling capacity requirements as well as the need for a large number of wires for thermometry and metrology. Optical ports will also be required to allow interferometric measurements through the cryostat walls.

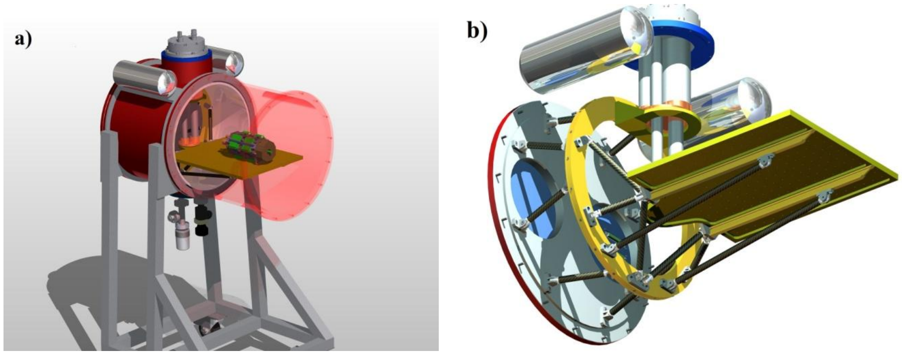

Figure 1. Schematic view of the proposed Cryogenic Test Facility: a) View of the 4 K plate and ODL with shields and outer vacuum chamber shown as transparent. b) Bottom view of the 4 K plate and support struts with shields and outer vacuum chamber removed.

For efficient and effective cooling of the FTS scanning mechanism and optical components, a large volume cryostat which utilizes the cooling power of a 2-stage high powered 4 K pulse tube cryo-refrigerator is being designed. The cooling system is a Cryomech PT415 pulse tube with a remote motor and a water-cooled CP1010 compressor unit[5]. At 4.2 K, the pulse tube has a 1.5 W cooling capacity on the second stage and a simultaneous 40 W cooling capacity on the first stage at 45 K. The second stage has a minimum temperature of 2.8 K with no thermal load. The 4K FTS mechanism in development for SAFARI has volume requirements of 420×220×125 mm[6]. In the interest of conducting future cryogenic tests of a complete FTS, similar to that of SAFARI, the cryostat must feature a working volume of at least this size. In addition, the ODL mechanism to be tested contains an off-loading electromagnet compensating for the gravitational force during earth-based tests of the instrument. Commercial off-the-shelf cryostats are not available for this application due to size limitations and positioning requirements for the ODL mechanism electromagnet, therefore the cryostat must be custom built. This cryostat will incorporate a non-inverted, rectangular 4 K stage which will be supported inside a cylindrical outer vacuum vessel oriented with the radial axis horizontal (Figure 1). The ODL and FTS mechanisms will be positioned on the 4 K plate and fitted with appropriate thermometers and wiring for the voice coils and actuators required for the scanning mechanism. In addition, an optical viewport will be positioned to allow the mounting of an external differential laser interferometer to test the capabilities of the moving stage. The model that has been selected for this project is a Renishaw differential interferometer (DI) detector head fed by a Renishaw laser unit (RLU) through a fiber[7]. The detector head will be mounted on the surface of the outer vacuum chamber, positioned to view a stationary mirror on the 4 K plate and also a retroreflecting mirror on the ODL in order to measure the relative displacement between them (Figure 2). In order for the pulse tube to cool down such a large volume, careful considerations must be made regarding the mechanical and thermal design and material choices.

To minimize convective heat transfer, a high vacuum environment is required. A turbomolecular pump will be used to achieve a pressure of ~ 10^{-5} Torr before commencing the cool down cycle. In order to minimize radiative heat transfer, radiation shields are required at the 4 K and 40 K stages. The 40 K shield is attached via a supporting ring which bolts to the 1st stage. The ring itself provides a solid framework for the shield and is supported by Carbon-Fiber-Reinforced Polymer (CFRP) struts which connect the 40 K shield to the OVC end plate (Figure 1). The rectangular 4 K shield is bolted directly to the 4 K stage, which is in turn connected to the 4 K pulse tube stage and supported by CFRP struts to the 40 K shield support ring. Additionally, optical inputs will be minimized and filtered in order to block thermal radiation from the laboratory. The 50 mm diameter viewports in the cryostat shields will be fitted with a plate with four 3 mm diameter holes to minimize the thermal loading apart from the four necessary 3 mm diameter laser interferometer beams (Figure 2).

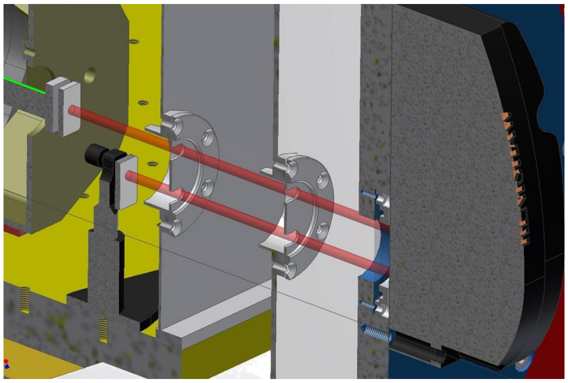

Figure 2. Cross-sectional view of the Renishaw differential interferometer attached to the cryostat wall and the optical viewports through the radiation shields. On the 4K stage, there is a stationary mirror and a movable mirror attached to the ODL.

Minimizing conductive heat flow represents a significant design challenge. The goal is to create layers of highly conductive, isothermal environments, with minimal conductive heat flow between them. The aforementioned CFRP struts are strategically used to support shielding containing the isothermal layers to minimize parasitic heat between layers. CFRP is fabricated to have a low thermal conductivity and a high tensile strength, making it the ideal material for this application. However, CFRP is a composite material consisting of two parts: an epoxy matrix and carbon fiber reinforcement. The thermal properties of the material depend on the relative density and placement of these two distinct elements. Consequently, the thermal conductivity and contraction of CFRP varies widely between manufacturers and even between produced batches. In order to predict the performance of the CFRP material in the cryostat, CFRP struts were fabricated and the thermal properties were characterized at cryogenic temperatures using the Renishaw DI system and careful thermometry, as described in the following section.

3. COMPONENT CHARACTERIZATION

3.1 Thermal Conductivity

The CFRP mechanical support struts are designed to have a high tensile strength and a very low thermal conductivity. Low conductivity is especially important for the supports between 4 K plate and the ring on the first pulse tube stage to prevent exceeding the cooling capacity of the pulse tube. Thermal tests were done to measure the heat conduction along a single strut for a thermal gradient of 4 K to 60 K. A single end of a strut was bolted to the 4 K pulse tube stage and Cernox resistance temperature detectors[8] (RTDs) were attached on either end. A resistor heater was attached to the free end. It was found that a constant heater output of 160 µW was required to maintain 60 K at the warm end. This gave an average thermal conductivity, $\bar{\lambda}$, of 0.015 W/(m·K) by the equation:

$$\dot{q}_{cond} = \frac{A}{L}\bar{\lambda}\Delta T \tag{1}$$

where $\dot{q}_{cond}$ is the conduction heat flow, L is the length, A its cross-sectional area, and ΔT the temperature difference between the ends of the strut. With the current system design using 8 struts of similar length to the test strut, a total 4 K heat load of 1.3 mW is predicted, representing a negligible fraction of the 1.5 W total cooling budget.

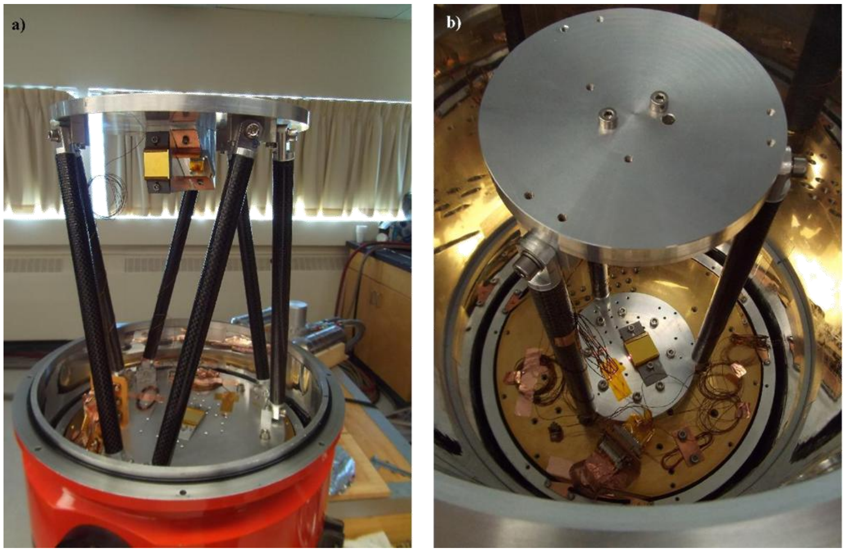

Figure 3. The CFRP contraction measurement structures: a) The original hexapod design of the CFRP contraction test structure; b) The refined, smaller diameter tripod design.

3.2 Thermal Contraction

In order to measure the contraction of CFRP struts over the range 300 K to 4 K, a test CFRP assembly was set up using a small volume cryostat and the Renishaw DI. In the original design, two aluminum plates were held parallel using six CFRP rods in a hexapod fashion (Figure 3a). Each strut was assembled using a CFRP tube and aluminum mounting points were held in place at either end using TorrSeal 2-part epoxy[9]. Each strut was then thermally cycled between 300 K and 4 K several times and mechanically tested to withstand at least a 90 kg tensile load. Bolted to the aluminum plates was a 45° fold mirror and a vertical reference mirror designed to reflect a horizontally incident laser beam down the vertical axis of the hexapod while retroreflecting a stationary reference beam, providing a differential measurement of the change in separation of the aluminum plates.

In addition, the hexapod was fitted with a number of Cernox RTDs (CX-1010-SD[8]) cryogenic thermometers (previously calibrated for the 4-300 K temperature range using the same cryostat system) along the length of a CFRP strut as well as the aluminum plates and both stages of the PT415 pulse tube. This smaller volume cryostat had only a single layer of shielding in place, which was thermally sunk to the 40 K stage of the pulse tube. Initial cooling tests revealed that more shielding was required for the structure to cool to 4 K. Additionally, poor thermal conduction along the CFRP struts caused the top plate of the hexapod to stay well above the desired temperature. It was determined that a flexible copper strap sunk to the 4 K pulse tube stage would cool the system down more efficiently while introducing minimal undesirable mechanical stresses. Without the strap, the free end of the hexapod stayed well above the desired temperature, reaching only 160 K over a time period of ~30 hours. The copper strap was a thin strip of Oxygen-Free High Conductivity (OFHC) copper, designed to allow the top aluminum plate to cool down to 4 K in less than 3 hours.

Unfortunately, the space required for the second layer of shielding was such that the existing hexapod was too large to fit inside the remaining volume. The structure was subsequently redesigned with a smaller diameter, but in order to use the same components and optical system, the design was constrained to use the previous system of parallel plates separated by three vertical struts (Figure 3b). This system suffered from reduced lateral rigidity compared to the hexapod design but resulted in much simpler thermal contraction measurements as the struts were oriented along the direction of contraction. It was determined, however, that vibrations caused by the pulse tube had similar effects on both the hexapod and the tripod designs. This was possible because vibrations were mainly along the rigid, vertical axis of the system. Vibrations of the pulse tube during cool down created substantial noise in the differential measurement on the order of ±0.1 µm. The new strut system was also created with the intent of providing a direct axial measurement of displacement (ie. without the 45° fold mirror) using a new window located in the bottom end of the cryostat. Importantly, this would reduce sensitivity in the measurement to lateral vibrations perpendicular to the struts.

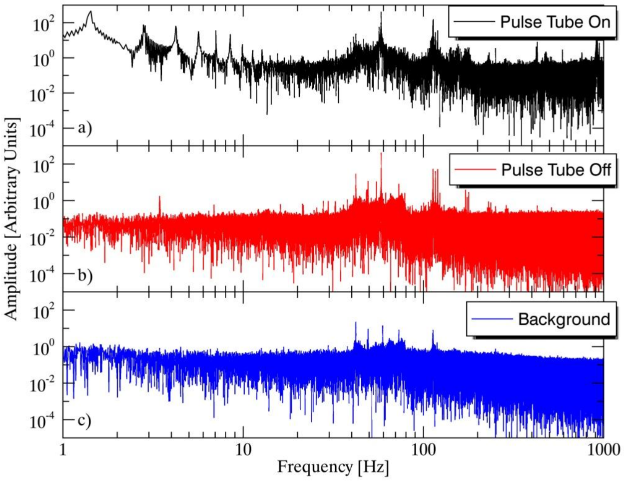

Figure 4. Power spectrum of displacement noise using the Renishaw DI: a) Pulse Tube On; b) Pulse Tube Off , Vacuum Pump On; c) Background Noise.

3.2.1 Pulse Tube Vibrations

As with any pulse tube cooled system, vibration caused by pressure changes in the pulse tube must be controlled when performing sensitive measurements. Normally, efforts are made to use vibration dampening components in order to achieve adequate precision. In this case, however, most vibrations were along the axis of the tripod. The differential interferometer is largely insensitive to these common-mode displacements. The only vibration effects that were evident were traced to imprecision in the alignment of the 45° mirror block. The operating frequency of the pulse tube is 1.3 Hz, resulting in vibrations at that frequency and its harmonics. Additionally, large compressors and vacuum pumps running in the laboratory contributed to vibrations of ~60 Hz and their harmonics. Figure 4 compares the frequency elements of the noise in the Renishaw DI measurement caused from the pulse tube with background measurements.

3.2.2 Optical Viewports

Currently, the cryostat viewport is fitted with a 50 mm diameter, 5 mm thick, uncoated fused silica (SiO_4) window. With the Renishaw DI system mounted on the window plate with a sealing gasket, the system is relatively light-tight to the laboratory environment, only allowing the Renishaw measurement beams into the vacuum chamber. It was found that reflections of the faces of the window do not interfere significantly with the readout of the interferometer but do cause a slight decrease in signal strength at the detector. If this becomes a limiting factor for the sensitivity of future ODL displacement readings, the window will be anti-reflection coated, optimized for transmission of the 632.8 nm HeNe line. Optical windows in the shields consist of 40 mm diameter circular apertures. As discussed in Section 2, optical windows in the shields of the cryogenic test facility will be much smaller. In the current system, large optical windows do not significantly affect the cooling capacity of the pulse tube.

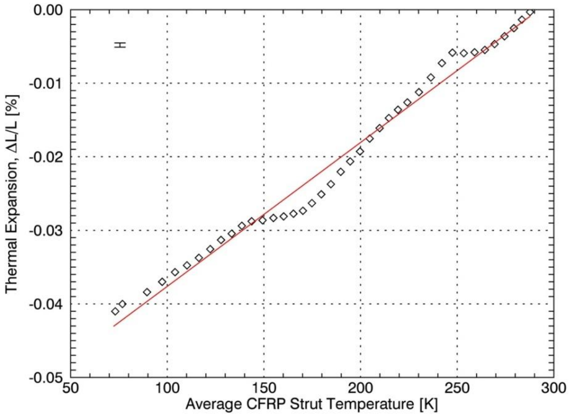

Figure 5. The percentage thermal expansion compared to the average CFRP strut temperature during a single cool down cycle. The slope of a linear regression fit to the data points gives the average CTE over the temperature range. A typical error bar is pictured in the top left corner.

3.2.3 Interferometer Interfacing

To avoid the use of large heaters to measure temperature dependent thermal contraction, the Renishaw DI system was set up to allow for contraction measurements during the cool down process. This required software that would record the interferometer output continuously for time scales on the order of 5 hours. For such large time scales, the software provided with the interferometer proved to be ineffective as it had a 20 second maximum recording time. To provide sufficiently long time series measurements, a USB-based microcontroller (Teensy++2.0[10]) was employed to interface with a Renishaw RPI-20 card. The card accepts analogue 1 Vpp sine/cosine signals and converts them to a 36-bit word, recording positional data with a 38.6 picometer resolution[11]. The Teensy read the Renishaw's 36-bit position encoder output. The system uses an external digital clock trigger since the microcontroller is not capable of real-time time stamping. Overflow conditions were included in the microcontroller code since missing a single sample would corrupt the time series. Data collection was started and stopped using manual switches, since polling the serial port for commands drastically slowed the collection rate. The maximum continuous reading frequency before the overflow condition was triggered was found to be ~17 kHz. For this application, 5 Hz sampling over a period of several hours was sufficient and produced manageable file sizes.

3.2.4 Coefficient of Thermal Expansion

With the flexible OFHC copper strap in place, both ends of the tripod structure reached a minimum temperature of 5 K in under 3 hours. However, a large thermal gradient still existed across the CFRP, with the middle of the struts remaining at 60 K. This may have been due to a large thermal resistance between the Cernox sensor and the strut, resulting in self-heating errors in the sensor. The resulting thermal gradients were fit with a 2nd order polynomial and a mean temperature was used to determine the coefficient of thermal expansion (CTE). The CTE, α, is given by the simple equation:

$$\frac{\Delta L}{L} = \alpha(T)\Delta T \, . \tag{2}$$

The temperature dependence of the contraction was found by measuring the contraction during a cool down cycle while recording the average strut temperature. The contraction of the aluminum end caps, mounting blocks and plates were determined using thermometers on the respective components and the known temperature dependent CTE curve for aluminum. These curves were subtracted from the final thermal expansion curve shown in Figure 5. The variation of CTE with temperature was relatively small, allowing the contraction data to be fit with a linear regression curve. The slope of the fit reflected the average CTE of the CFRP struts over the 60 - 300 K temperature range. Using this analysis, the average CTE of these CFRP struts was determined to be $(1.95 \pm 0.01) \times 10^{-6}$ K^{-1} for this temperature range.

At certain temperature intervals, non-uniform warping of the tripod structure caused a shift in the angular position of the mirrors. This caused the Renishaw DI unit to lose the measurement beams, necessitating a manual realignment process. At these unavoidable positions, the total thermal expansion was lost, but relative contraction during further cooling continued to be measured unhindered. The curves following realignment were stitched on to the previous contraction curve using a linear fit of the previous data points as a guideline.

4. FUTURE DEVELOPMENTS

After refitting the existing cryostat with an axial window, a face-on contraction measurement will be attempted, which is more suitable for future tests of a 4 K FTS translation stage. Additionally, efforts will be made to improve the measurement accuracy by using AR coated windows, optical filters, and vibration isolation. While we wait for the acquisition of the large test cryostat we will develop a compact cryogenic FTS that will fit within our current small cryostat, which will allow performance testing of optical and mechanical FTS components in a 4 K environment.

5. CONCLUSION

Progress continues to be made on the design for a large volume cryogenic test facility. Preliminary measurements of the expected performance of the cryostat subcomponents are under way and decisions on materials used in the design are being finalized. A report on the performance of a cryogenic FTS will be produced once construction of the large scale test facility is completed.

ACKNOWLEDGMENTS

The authors acknowledge support from the Canada Foundation for Innovation, the Canadian Space Agency, EU FP7-FISICA and NSERC.

REFERENCES

[1] Swinyard, B., and Nakagawa, T., "The space infrared telescope for cosmology and astrophysics: SPICA A joint mission between JAXA and ESA," Experimental Astronomy 23(1), 193-219 (2009).
[2] Pilbratt, G. L., Riedinger, J. R., Passvogel, T. *et al.*, "Herschel Space Observatory*," A&A 518, L1 (2010).
[3] Roelfsema, P., Giard, M., Najarro, F. *et al.*, "The SAFARI imaging spectrometer for the SPICA space observatory." Proc. SPIE 8442, 84420R-84420R-15 (2012).
[4] van den Dool, T. C., Kamphues, F., Gielesen, W. L. M. *et al.*, "The development of a breadboard cryogenic optical delay line for DARWIN." Proc. SPIE 6692, 66920A-66920A-12 (2007).
[5] http://www.cryomech.com/products/cryorefrigerators/pulse-tube/pt415/.
[6] van den Dool, T. C., Kruizinga, B., Braam, B. C. *et al.*, "SPICA/SAFARI Fourier transform spectrometer mechanism evolutionary design." Proc. SPIE 8442, 84423R-84423R-7 (2012).
[7] http://renishaw.ca/en/rle-fibre-optic-laser-encoder--20999.
[8] http://www.lakeshore.com/products/cryogenic-temperature-sensors/cernox/models/pages/overview.aspx.
[9] http://www.lesker.com/newweb/fluids/sealants_epoxy.cfm?pgid=torrseal.
[10] http://www.pjrc.com/store/teensypp.html.
[11] http://www.renishaw.ca/en/rpi20-parallel-interface--6488.